NASA TM X-372

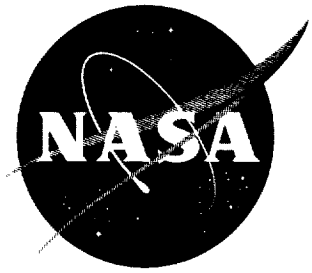

TECHNICAL MEMORANDUM

X-372

INVESTIGATION AT MACH NUMBERS OF 0.20 TO 3.50 OF BLENDED WING-BODY COMBINATIONS OF SONIC DESIGN WITH DIAMOND, DELTA, AND ARROW PLAN FORMS

By George H. Holdaway and Jack A. Mellenthin

Ames Research Center,
Moffett Field, Calif.

NATIONAL AERONAUTICS AND SPACE ADMINISTRATION

WASHINGTON

August 1960
Declassified September 1, 1961

NATIONAL AERONAUTICS AND SPACE ADMINISTRATION

TECHNICAL MEMORANDUM X-372

INVESTIGATION AT MACH NUMBERS OF 0.20 TO 3.50 OF BLENDED WING-BODY COMBINATIONS OF SONIC DESIGN WITH DIAMOND, DELTA, AND ARROW PLAN FORMS

By George H. Holdaway and Jack A. Mellenthin

SUMMARY

The models had aspect-ratio-2 diamond, delta, and arrow wings with the leading edges swept 45.00°, 59.04°, and 70.82°, respectively. The wing sections were computed by varying the section shape along with the body radii (blending process) to match the prescribed area distribution and wing plan form. The wing sections had an average value of maximum thickness ratio of about 4 percent of the local chords in a streamwise direction. The models were tested with transition fixed at Reynolds numbers of about 4,000,000 to 9,000,000, based on the mean aerodynamic chord of the wings. The effect of varying Reynolds number was checked at both subsonic and supersonic speeds.

The diamond model was superior to the other plan forms at transonic speeds ($(L/D)_{max}$ = 11.00 to 9.52) because of its higher lift-curve slope and near optimum wave drag due to the blending process. For the wing thickness tested with the diamond model, the marked body and wing contouring required for transonic conditions resulted in a large wave-drag penalty at the higher supersonic Mach numbers where the leading and trailing edges of the wing were supersonic. Because of the low sweep of the trailing edge of the delta model, this configuration was less adaptable to the blending process. Removing a body bump prescribed by the Mach number 1.00 design resulted in a good supersonic design. This delta model with 10 percent less volume was superior to the other plan forms at Mach numbers of 1.55 to 2.35 ($(L/D)_{max}$ = 8.65 to 7.24), but it and the arrow model were equally good at Mach numbers of 2.50 to 3.50 ($(L/D)_{max}$ ≈ 6.85 to 6.39). At transonic speeds the arrow model was inferior because of the reduced lift-curve slope associated with its increased sweep and also because of the wing base drag. The wing base-drag coefficients of the arrow model based on the wing plan-form area decreased from a peak value of 0.0029 at Mach number 1.55 to 0.0003 at Mach number 3.50.

Linear supersonic theory was satisfactory for predicting the aerodynamic trends at Mach numbers from 1.55 to 3.50 of lift-curve slope, wave drag, drag due to lift, aerodynamic-center location, and maximum lift-drag ratios for each of the models.

INTRODUCTION

This report is a continuation of the investigation of a blended diamond wing and body combination reported in reference 1. The design method has been applied to models with delta and arrow plan forms. The diamond wing, which is the best structural shape of the zero-taper-ratio plan forms, is generally considered to be aerodynamically the poorest, particularly at Mach number 1.00. This concept was discussed in reference 1, which also illustrated how some of the transonic limitations of the diamond plan form could be overcome. The purpose of the present investigation was to illustrate with experiment and theory the effects of wing plan-form variation on the aerodynamic performance characteristics of blended wing-body combinations.

The diamond model was designed with a body, wing sections, and area distribution which resulted in near optimum zero-lift wave drag at Mach number 1.00 and in decreasing wave-drag coefficients for Mach numbers up to 1.20. An interesting feature of the diamond-wing design was that the computed inboard wing sections were inverted. Similar analysis of arrow and delta plan forms with the same over-all model area distribution as the diamond model indicated that equally low wave drag could be obtained at $M = 1.00$, but there would be some increase in wave-drag coefficient with increasing Mach number. Although different area curves could have been selected for the sonic design of the arrow and delta models, the analysis included in appendix A indicated that using the same area curve as selected for the diamond model would give essentially the same transonic wave-drag results. Using the same area distribution for all the models would permit an evaluation of possible plan-form effects at $M = 1.00$. Each plan form had an aspect ratio of 2, and the complete models were designed so that most geometric items, such as volume, span, and length, were equal. The wing sections were computed from the selected area distribution by assuming linear spanwise thickness variation of elements perpendicular to the center line. The design procedure is described in appendix B of reference 1. The leading edges of the diamond, delta, and arrow wings were swept 45.00°, 59.04°, and 70.82°, respectively.

Experiments were conducted at Mach numbers from 0.20 through 3.50 at Reynolds numbers based on the mean aerodynamic chord of roughly 4,000,000 to 9,000,000. Also tested at Mach numbers from 0.60 to 2.35 was a body with the same area distribution as the design area distribution for the wing-body combinations. The wave drag of the body alone served as a reference or a reasonable goal for the wing-body combinations. As a check

on the experimental results, theoretical predictions were made of the friction drag, zero-lift wave drag, drag due to lift, lift-curve slope, maximum lift-drag ratio, and aerodynamic-center position of the models with wings.

A limited investigation of the effect of sweep on transition of the boundary layer from laminar to turbulent flow was conducted with the sublimation technique to insure that transition was fixed on each model. A delta model was tested at Mach number 3.00 and a Reynolds number per foot of 2,000,000, with four different sizes of grit used as a distributed roughness to fix the boundary-layer transition. The tests of the different sizes of grit were made to evaluate the magnitude of the drag penalty of the grit itself above the drag change caused by fixing transition. These results are discussed in appendix B.

NOTATION

A	aspect ratio
A_{bb}	body base area
A_{wb}	wing base area projected on a plane perpendicular to the conventional x axis
A_N	area distribution of the approximate Newtonian spindle shape (see fig. 20)
A_n	coefficients determining the magnitude of the harmonics of a Fourier sine series
$\frac{b}{2}$	semispan
C_D	drag coefficient (All aerodynamic coefficients are based on the total wing area.)
$\frac{C_{D_i}}{C_L^2}$	slope of the curve of drag coefficient due to lift versus lift coefficient squared, taken at the lift-coefficient data point nearest to that for $\left(\frac{L}{D}\right)_{max}$
C_{D_o}	zero-lift drag coefficient
C_{D_b}	wing or body base drag coefficient
C_L	lift coefficient

C_{L_α}	lift-curve slope, per deg
C_m	pitching-moment coefficient about body station 34.50 inches, measured from the body nose, except that when noted the body station was selected to produce 10-percent static margin at M = 0.60
c_R	wing root chord measured along model center line
$\bar{c}$	mean aerodynamic chord of the wings
k	average height of transition grit based on at least 100 samples
$\left(\frac{L}{D}\right)_{max}$	maximum lift-drag ratio
l	model length
M	Mach number
N	total number of harmonics used to compute ΔC_{D_o} or to define an area distribution
n	specific term or harmonic used to define an area distribution
R	Reynolds number
r	body radius
r_o	body maximum radius
r_b	body base radius
S	cross-sectional area
S_W	total wing area
$\frac{t}{2}$	wing semithickness
x	coordinate and body station, measured from model nose
y	coordinate measured in a spanwise direction
$\frac{x_1}{c_R}$	aerodynamic-center location, where x_1 is the station measured from leading edge of wing center-line chord
V	volume

$\frac{V}{V_{A_2}}$ volume relative to a Sears-Haack body with minimum wave drag for given volume and length

α angle of attack

β $\sqrt{M^2 - 1}$

ΔC_{D_o} zero-lift wave-drag coefficient

θ roll angle of a cutting plane tangent to a Mach cone as measured between the z axis and the intersection of the cutting plane with the yz plane

Λ_{LE} angle of wing leading-edge sweep

φ transformation of the length x to radians, $\cos^{-1}\left(\frac{2x}{l} - 1\right)$

MODELS AND TESTS

The geometric details of the M = 1.00 equivalent body and the three wing-body combinations are presented in figures 1 and 2 and in tables I through IV. The delta model was also tested without a rearward body bump as shown in figure 1(c) and in table I, which lists the radii of the body components of each model. The design area distribution derived in reference 1 is presented in figure 3, along with the modified area distribution for the delta model without the body bump.

The wing coordinates are listed in tables II through IV for the three plan forms. The wing thickness distributions are illustrated in figure 2 and were computed as described in reference 1. The wing thickness in each case is formed by straight-line elements perpendicular to the model center line which form triangular spanwise sections as shown in figure 2. Note that the rear portion of the arrow wing was designed with a blunt trailing edge, as suggested in reference 2, to avoid wing sections with large rearward slopes. For wing sections perpendicular to the body center line, similar to the one shown in figure 2(c), the trailing-edge thicknesses of the arrow wing were half the ridge thicknesses, except near the body juncture, as shown in table IV. The wing sections had an average value of maximum thickness of about 4 percent of the local chords in a streamwise direction with greater thickness ratios inboard.

The models were tested at the Ames Research Center in the 12-foot subsonic pressurized wind tunnel, the 14-foot transonic wind tunnel and in the 9- by 7-foot and the 8- by 7-foot supersonic test sections of the

Unitary Plan wind tunnel. Photographs of the models are presented in figures 4(a) through 4(d). The ranges of the test variables in each facility are shown in the following table:

Tunnel throat	Models (1)	M	R/ft	α, deg	Transition
12-foot	◇ △ A	0.20	3,000,000	-4 to 26	Free
12-foot	◇ △ A	0.20	6,000,000	-4 to 26	↓
12-foot	◇ △ A	0.50	3,000,000	-4 to 18	↓
14-foot	◇ △ ▲ A B	0.60 to 0.80	3,500,000 to 4,000,000	-2 to 11	Fixed, 0.040-inch grit
14-foot	◇ △ ▲ A B	0.80 to 1.20	4,000,000	-2 to 8	↓
9- by 7-foot	◇ ▲ A B	1.55	4,000,000	-3 to 6	↓
9- by 7-foot	◇ ▲ A B	1.55 to 2.35	3,000,000	-2 to 12	↓
8- by 7-foot	◇	2.50 to 3.00	4,000,000	-2 to 12	↓
8- by 7-foot	◇	3.00 to 3.50	3,000,000	-2 to 12	↓
8- by 7-foot	▲ A	3.00	3,000,000	-3 to 13	↓
8- by 7-foot	▲ A	2.50 to 3.50	2,000,000	-3 to 15	↓
8- by 7-foot	▲	3.00	2,000,000	-1 to 15	Free and fixed with 4 sizes of grit
8- by 7-foot	◇ ▲ A	3.50	2,000,000	0	One wing panel free and the other panels fixed with different sizes of grit

(1) B M = 1.00 equivalent body
◇ Diamond model
△ Delta model
▲ Delta model without bump
A Arrow model

Three-component aerodynamic forces and moments were measured and corrected by standard procedures. For the model sizes and shapes, the force corrections for blockage and buoyancy were generally believed to be negligible. Wall interference corrections were required for the angle-of-attack and drag data obtained in the subsonic wind tunnel, and these corrections were based on the theory of reference 3. At all Mach numbers, the drag coefficients were adjusted by setting the body base pressure equal to free-stream static pressure. All aerodynamic coefficients were based on the complete plan-form area of the wings of 800 square inches. The pitching-moment coefficients were computed about a longitudinal center 34.50 inches rearward from the nose of each model. This position was selected for approximately neutral longitudinal stability at moderately supersonic speeds.

Transition was fixed near the nose of the bodies and near the leading edge of the wings with distributed roughness composed of grit with an average height of about 0.040 inch. The grit was located 1.13 inches rearward of the wing leading edges (upper and lower surfaces) and of the body nose in a streamwise direction so that a laminar-flow area of only 5 percent of the wing area was allowed. A grit location farther rearward could have been used at the higher supersonic Mach numbers; however, natural transition would have occurred ahead of the grit location at transonic speeds. The selection of the grit size was based on tests of the diamond wing reported in reference 1. The diamond wing with the least sweep was considered to be the most difficult to fix transition on, so the same grit is certainly larger than necessary for the other plan forms. Subsequent to the tests with the diamond model, the 8- by 7-foot test section was limited to lower Reynolds numbers; so additional tests, reported in appendix B, were made to check the performance of the grit in fixing transition on each wing and to determine the drag penalty attributable to the grit.

RESULTS

The basic test data are presented in figures 5 through 10. Notice that the data from the subsonic wind tunnel are plotted to a coarser scale than the rest of the data because of the greater angle-of-attack range. For this reason, and in order to illustrate the slight effects of doubling the Reynolds number, the data obtained on the three basic models having different plan forms at $M = 0.20$ are listed in table V. The delta model was tested at transonic speeds both with and without the rearward bump on the body; however, only the basic data for the delta model as designed for $M = 1.00$ (with the body bump) are presented at transonic speeds (fig. 6). At supersonic speeds the delta model was tested only without the bump as indicated by the results in figures 7 and 8. A comparison at transonic speeds between the delta models with and without the bump will be briefly discussed relative to cross plots of the data and will be considered in more detail in appendix A. At supersonic speeds the effect of Reynolds number is illustrated only for the delta model without bump and the arrow model (figs. 7(d) and 7(e) at $M = 1.55$ and figs. 8(d) and 8(e) at $M = 3.00$), because the Reynolds number effects on the diamond model data have been reported in reference 1. The $M = 1.00$ equivalent body was tested over a small angle-of-attack range to clearly define the zero-lift drag coefficients which are presented in figure 9.

Figure 10 shows how the wing-base-pressure coefficients for the arrow model varied with spanwise position and Mach number. Body-base pressures were measured for each model and were used to correct the drag data. The body-pressure coefficients shown in figure 10 for the arrow model are representative of the values obtained for each model.

Cross plots of the various aerodynamic parameters with Mach number will be presented when discussed in the following sections of the report. Figure 11 is presented in order to summarize the differences in test Reynolds numbers with Mach number. Note that for Mach numbers above 2.50 the diamond model was generally tested at higher Reynolds numbers than the other models; however, the effects of this Reynolds number difference were not very large, as may be seen in figures 8(d) and 8(e).

DISCUSSION

In general, the discussion will make comparisons between the experimental results for the three models of different plan form and between supersonic linear theory and experiment for each plan form. The delta model without the rearward body bump is used for the comparisons between plan forms, because the body bump required for the sonic design was too blunt to be treated by linear theory at supersonic speeds. This problem is discussed more fully in appendix A, which contains an evaluation of the transonic zero-lift wave drag relative to the design concepts. Except for the subsonic data from $M = 0.20$ to $M = 0.50$, the results discussed are for transition fixed and have not been corrected for the drag penalty which can be attributed to the grit. Appendix B presents an analysis of theoretical and experimental results of the effect of the grit used to fix transition, at $M = 3.00$. The analysis indicated a grit penalty in C_{D_0} of 0.0003 separate from and above the effect of fixing transition. The wave drag due to the grit appeared to be negligible.

The following discussion has two main divisions: the first part is an analysis of the zero-lift wave and base drags, and the second is an analysis of the other basic aerodynamic trends with Mach number. The arrow-model data contain the wing base drag.

Zero-Lift Wave and Base Drags

The zero-lift wave-drag coefficients for the three wing plan forms and the $M = 1.00$ equivalent body at Mach numbers from 0.60 to 3.50 are presented in figure 12. The theoretical wave-drag coefficients were computed with the procedures of reference 4, and 49 harmonics were used to define the derivative of the model area distributions. The variation of the body area distribution with Mach number, used in the theoretical computations, was based on method 1 described in reference 1.

The experimental zero-lift wave-drag coefficients (fig. 12(b)) were determined from the basic data by removing the friction-drag coefficients. The friction-drag coefficients were assumed to be equal to the zero-lift drag coefficient at $M = 0.60$ and were adjusted at each Mach number to

account for the variation with Mach number of the friction-drag coefficient for fully turbulent flow over a smooth surface. This procedure was discussed and justified in reference 1. For the test models, the small regions of laminar flow and of turbulent flow over a rough surface had small and compensating effects relative to the variation in friction-drag coefficient with Mach number. The friction-drag coefficients used to determine the wave-drag coefficients were also corrected for variations in Reynolds number. The latter correction was not made for the results presented in reference 1, because the variations in Reynolds number were not as great in that case. The experimental results of figure 12(b) showed that the diamond model had the lowest wave-drag coefficient at transonic speeds with values which matched the $M = 1.00$ equivalent body data; the diamond model had higher wave drag than the other models at Mach numbers above 1.7.

The comparison between theory and experiment can be more clearly demonstrated by considering each model separately (see fig. 13). For the simple body, the 49-harmonic solution is larger than the experimental results at supersonic speeds, although the variation with Mach number is similar. The diamond model data (fig. 13(b)) have been discussed previously in reference 1 and are repeated here with the slight Reynolds number correction used for all the data presented in this report. The reduction in wave-drag coefficient shown for the computation identified as method 2 (discussed in ref. 1) would be less for the smoother body of the arrow model and almost negligible for the delta model without bump. In general, the experimental wave-drag coefficients for the three plan forms investigated are lower than the theoretical wave-drag coefficients near sonic wing-edge conditions. The one exception is for the delta model, which had perfect agreement between theory and experiment at sonic leading-edge conditions. Note in this case that the theory did not indicate a wave-drag peak at sonic leading-edge conditions, and thus this better agreement between theory and experiment for the delta model is reasonable. As was discussed in reference 1, the higher wave-drag coefficients for the diamond model at the higher Mach numbers are a result of the marked body and wing contouring required for transonic conditions.

The experimental wave-drag coefficients shown for the arrow model in figure 13(d) include the wing base-drag coefficient. The agreement between theory and experiment shown at the intermediate supersonic Mach numbers would be poorer if the variation with Mach number of wing base drag were introduced. The theory used to compute the wave-drag coefficients does not include viscous effects. The zero-lift base-drag coefficients for the wing and body bases of the arrow model, as determined by experiment and empirical predictions based on reference 5, are presented in figure 14. The body base-drag coefficients include an effect of the sting, so the comparison made with the analysis of reference 5 is only qualitative. The body base-drag coefficients are representative of the values for the other models. The wing base-drag coefficients of the arrow model, based on the wing plan-form area, decreased from a peak value of 0.0029 at Mach number

1.55 to 0.0003 at Mach number 3.50. The two-dimensional analysis of reference 5 did not represent the three-dimensional results at transonic speeds, but could be used to obtain slightly conservative predictions for Mach numbers above 1.60. The individual pressure measurements at different locations on the wing base varied as shown by the basic pressure coefficients in figure 10. The greatest differences in wing-base pressure coefficients occurred where these coefficients were the greatest, that is, from Mach numbers 1.55 to 2.35.

Aerodynamic Trends With Mach Number

Summary plots of experimental values of maximum lift-drag ratio, lift-curve slope, drag due to lift, and aerodynamic-center location are presented in figure 15 for the three models of different plan form. It should be noted that the delta model without the rearward body bump, used for the comparison between plan forms at supersonic speeds, had about 10-percent less volume than the other models. The model with the greatest maximum lift-drag ratio or the greatest lift-curve slope generally was the one with the lowest zero-lift wave-drag coefficients. At transonic speeds the diamond model was superior ($(L/D)_{max}$ = 11.00 to 9.52); at the intermediate supersonic Mach numbers the delta model without bump was superior ($(L/D)_{max}$ = 8.65 to 7.24); at Mach numbers from 2.50 to 3.50 the difference between models was not very great and the delta model without bump and the arrow model were equally good ($(L/D)_{max}$ ≈ 6.85 to 6.39). With an increase in Reynolds number, the maximum lift-drag ratios would be increased, as may be determined from the example plots presented in figures 7(d) and 7(e). For instance, in figure 7(d), which shows the least effect, the increase in Reynolds number per foot from 3,000,000 to 4,000,000, for the delta model without bump, resulted in an increase in $(L/D)_{max}$ from 8.65 to 8.86 (M = 1.55). The effect of zero-lift drag on the maximum lift-drag ratio is as important as the drag due to lift and should be kept in mind when one compares the data presented in figures 15(a) and 15(c). For Mach numbers from 2.50 to 3.50, the arrow model, relative to the delta model without bump, clearly has the lower values of drag due to lift. However, at M = 3.50 an increase in zero-lift drag coefficient, from 0.0075 for the delta model without bump to 0.0082 for the arrow model, was enough to cancel a possible benefit in maximum lift-drag ratio due to a decrease in C_{D_i}/C_L^2 from 0.813 to 0.726. Less than half of the above increase in zero-lift drag coefficient of 0.0007 (that is, 0.0003) could be attributed to the arrow wing-base drag, but the remaining difference is small relative to possible cumulative experimental errors. These data indicate that the effects of the plan-form variation considered are small at Mach numbers above 2.50, and that the model with the lowest zero-lift drag coefficients would probably have the highest values of maximum lift-drag ratio. The zero-lift wave drag of each of the test models could be improved if specifically designed for the higher supersonic Mach numbers; however, the greatest potential improvement exists for the model with the

diamond wing which structurally could be made thinner than the other plan forms. With transition free, the wing with the least sweep would also have potentially the greatest amount of laminar flow, as shown in appendix B, and thus lower friction drag.

The variation in aerodynamic-center location with Mach number, as shown in figure 15(d), occurred primarily at transonic speeds, was not unduly large for any of the models, and was greatest for the diamond model.

The utility of supersonic linear theory in predicting the trends in the aerodynamic parameters is demonstrated in figures 16 and 17 for the delta model without bump and the arrow model, respectively. Theoretical comparisons with experimental results were presented and discussed in reference 1 for the diamond model and will not be repeated here. The theoretical results presented in figures 16 and 17 were computed in the same manner as in reference 1, and, except for the friction and wave drags required in computing the maximum lift-drag ratios, the theoretical results were computed from equations available in reference 6 or 7. The theory used assumed no wing leading-edge suction and no arrow-wing base drag. Theoretical estimates of wing leading-edge thrust are considered in later figures. The agreement shown in figures 16 and 17 between theory and experiment and between test facilities was considered to be satisfactory, because the differences shown are generally of the same order of magnitude as the slight nonlinearities in the basic data. For instance, the large difference in the trend of the lift-curve slopes for the arrow model (fig. 17(b)) between the highest transonic data and the $M = 1.55$ data obtained in the 9- by 7-foot test section occurred near zero lift where the slopes were measured. At angles of attack of 2° or 3° the lift-curve slopes for the arrow model are about the same at transonic speeds as at $M = 1.55$. As was the case in reference 1, the experimental lift-curve slopes obtained in the 9- by 7-foot test section were consistently higher than those of the theory.

Some wing leading-edge thrust is indicated in figures 16(c) and 17(c), because the experimental values of C_{D_i}/C_L^2 are lower than the theoretical values based on no-leading-edge thrust. However, only a small amount of the theoretically possible leading-edge thrust was obtained for the arrow model. Figure 18 presents the theoretical values of the drag-due-to-lift parameter, C_{D_i}/D_L^2, with and without leading-edge thrust, as a function of β, for flat-plate wings of the three plan forms investigated. From supersonic theory alone and assuming almost full leading-edge thrust, one might conclude that the arrow model would be superior at all Mach numbers and C_{D_i}/C_L^2 would approach the minimum vortex drag due to lift or a value of $1/\pi A$ at $\beta = 0$ (or $M = 1.00$), as plotted in figure 18. The linearized theory used for computing the leading-edge thrust was developed in reference 6, which states that no entirely satisfactory theory for this effect has been developed. Thus, if one assumes little leading-edge thrust, the arrow model would only be superior at the highest Mach numbers and there

only slightly superior. The experimental results (fig. 19) indicated that there was little leading-edge thrust. Although the arrow model had some leading-edge thrust at the lower values of β, it had a drag-due-to-lift parameter as high as or higher than that for the other models at values of β lower than 2.0.

CONCLUDING REMARKS

The following statements apply to blended wing-body combinations as tested with transition fixed by distributed roughness.

The diamond model was superior to the other plan forms at transonic speeds ($(L/D)_{max}$ = 11.00 to 9.52) because of its higher lift-curve slope and near optimum wave drag due to the blending process. For the wing thickness tested with the diamond model, the marked body and wing contouring required for transonic conditions resulted in a large wave-drag penalty at the higher supersonic Mach numbers where the leading and trailing edges of the wing were supersonic. Possible advantages in supersonic zero-lift drag are significant for the diamond model, because its structural rigidity will permit a thinner wing section and its low relative sweep is favorable to laminar boundary-layer flow.

The delta model was less adaptable to the blending process because of the low sweep of the trailing edge. Removing a body bump, prescribed by the Mach number 1.00 design, resulted in a good supersonic design. The 10-percent less body volume made it superior to the other plan forms at Mach numbers of 1.55 to 2.35 ($(L/D)_{max}$ = 8.65 to 7.24). This delta model and the arrow model were equally good at Mach numbers of 2.50 to 3.50 ($(L/D)_{max} \approx$ 6.85 to 6.39).

At transonic speeds the arrow model was inferior because of the reduced lift-curve slope associated with its increased sweep and also because of the wing base drag. The wing base-drag coefficients of the arrow model, based on the wing plan-form area, decreased from a peak value of 0.0029 at Mach number 1.55 to 0.0003 at Mach number 3.50.

Linear supersonic theory was satisfactory for predicting the aerodynamic trends at Mach numbers from 1.55 to 3.50 of lift-curve slope, wave drag, drag due to lift, aerodynamic-center location, and maximum lift-drag ratios.

There was no apparent sweep effect on the wave drag of the sharp-leading-edged wings at Mach number 1.00.

Ames Research Center
National Aeronautics and Space Administration
Moffett Field, Calif., March 23, 1960

APPENDIX A

EVALUATION OF TRANSONIC DATA RELATIVE TO SONIC DESIGN

The design area curve (fig. 3) was selected primarily for the diamond plan form as discussed in reference 1 (to seek a low wave drag at $M = 1.00$ which was consistent with a decreasing supersonic wave-drag coefficient). This design curve is a modification ($N = 25$ fit of the derivative) of the peak-shaped area curve presented in the upper left-hand corner of figure 20. Of the area curves considered in the preliminary analysis (fig. 20) this peak type of area curve was also best for the delta plan form at transonic speeds ($\beta \cos \theta = 0$ to 0.6633) and almost best for the arrow plan form as shown in table VI. In any case, it was decided to use the same area curve for each plan form so that a direct comparison could be made of the effect of sweep on zero-lift wave drag at Mach number 1.00.

Data points of transonic zero-lift wave-drag coefficients are plotted in figure 21 to show clearly how well the diamond and arrow models matched the equivalent body at Mach number near one. Therefore, there is no apparent sweep effect on the wave drag of sharp-leading-edged wings at Mach number one.

The higher wave drag of the delta model at Mach number 1.00 was not predicted by theory, because all models had identical cross-sectional area distributions. This model illustrates that an area distribution made up of a wing and a body which individually have large slopes in area distribution can result in wave drag greater than that for the equivalent body. For the delta-type wing the problem is primarily confined to transonic speeds and is a result of the low sweep of the wing trailing edge. The sonic design contour for the body of this delta model resulted in a large body bump which caused an increased thickening of the boundary layer, as indicated by the surface flow lines in figure 22. The fluorescent-oil film method used for the surface flow study is described in reference 9. The increased boundary-layer thickness would result in an effective increase in the bump size over that prescribed by the design and thus in higher wave drag. Removing the entire bump, as indicated by the body radii of table I, resulted in an increase in the drag coefficients near Mach number 1.00, as shown in figure 23, and a reduction in wave-drag coefficient for Mach number 1.20.

The theoretical zero-lift wave-drag coefficients of the various winged models at transonic speeds are compared with experimental results in figure 24. The predictions for the diamond and arrow models are very good for 25 harmonics as well as for 49. The previously discussed problems with the delta model affected the theoretical results as well. The delta model, with the body bump of sonic design, obviously violated the slenderness limitations for the theory, as indicated by the poor wave-drag

coefficient predictions. Without the bump, the low sweep of the trailing edge of the delta wing is responsible for the high wave drag and poor predictions at Mach number 1.00. Also note that the use of the higher number of harmonics for both of the delta models generally results in poorer agreement with experiment. The predictions for the delta model without the bump were satisfactory for Mach numbers above 1.20, as shown previously in figure 13(c).

The inferior aerodynamic characteristics of the arrow model at transonic speeds were analyzed to insure that the reductions in maximum lift-drag ratio were primarily due to the increased sweep (reduction in lift-curve slope) and not due to the wing base drag or to separated flow. The effect of the wing base drag on the maximum lift-drag ratios at transonic speeds was not large relative to the differences between models, as shown in figure 25. The possibility that the arrow wing had separated flow was investigated with the fluorescent-oil technique of reference 9. At low lift coefficients representative of the maximum lift-drag ratios there were no visible regions of separated flow, and the surface flow was uniform in a streamwise direction. At angles of attack greater than 4° there was a faint indication of a leading-edge vortex and a small separated-flow region near the trailing edge of the arrow wing. The small separated-flow region increased with angle of attack to that shown in figure 26 for 11° ($M = 0.70$). The separated region may be identified by the accumulation of oil which appears as a short curved line near the wing trailing edge.

APPENDIX B

DRAG DUE TO THE GRIT USED TO FIX TRANSITION

Lift and drag coefficients for the delta model without bump, with transition free and fixed at Mach number 3.00 and a Reynolds number per foot of 2,000,000, are presented in figure 27. Runs with transition fixed on the wing and body were made with four sizes of grit with average heights, in inches, of 0.016, 0.040, 0.062, and 0.089. The grit was located, as for the basic investigation, 1.13 inches rearward of the wing leading edges (upper and lower surfaces) and of the body nose in a streamwise direction. The drag due to lift for the transition-free run (figure 27) was greater than the theoretical value of $C_{D_o} + C_L \tan \alpha$ and corresponding values of drag due to lift with transition fixed. This result was probably due to a forward movement of natural transition (primarily noted on the lower surface from sublimation pictures taken at $(L/D)_{max}$) with an increase in angle of attack. At lift coefficients above 0.30 the reason for the drag coefficients of the model with the 0.040-inch grit being lower than those for the transition-free model is not known; however, for the one run with the 0.040-inch grit, the model mounting holes were filled a little more smoothly (painted and sanded condition as used for the results presented in the body of the report). For the other runs presented in figure 27 the holes were filled with wax.

The 0.016-inch grit did not quite fix transition at $M = 3.00$ and definitely did not fix transition at $M = 3.50$, as shown in figure 28 (R/ft = 2,000,000). Otherwise the larger grit (0.040 in. or greater) fixed transition at the grit for all test Mach numbers and Reynolds numbers. Figure 28 also shows that there was a decrease in the length of the laminar boundary-layer flow with increase in wing leading-edge sweep. For each wing the white lines are spaced three inches apart in a streamwise direction. The most forward line shown in most of the photographs is where the grit was located 1.13 inches from the wing leading edge in a streamwise direction.

The zero-lift data of figure 27 are plotted in figure 29 to show the effect of grit size on the zero-lift drag coefficients of the delta model without bump, as determined by experiment and theory ($M = 3.00$, R/ft = 2,000,000). The theoretical friction-drag coefficients were computed by procedures discussed in reference 1. The average length of the laminar-flow region, used for the transition-free theoretical point, was estimated from photographs of sublimation material to be 6 inches, or somewhat less than the higher Mach number pattern shown in figure 28. The theoretical effect of fixing transition was computed at zero grit size as the change from partially laminar flow over a smooth surface to completely turbulent flow (rearward of the 1.13-in. station). The lack of agreement between the theoretical and experimental drag coefficients shown

in figure 29 for zero grit size may be attributed to errors in the theoretical wave drag; however, the experimental model may not have been theoretically smooth. The important feature of figure 29 is that the experimental increase in zero-lift drag with increasing grit size was predicted by a theory (M = 0) which did not include the possibility of wave drag attributable to the grit. Thus, the wave drag of the grit was apparently negligible. The theoretical slope of figure 29 (which involves the average grit size squared) was extrapolated through the experimental data points to zero grit size, which would give an indication of the experimental zero-lift drag coefficient with transition fixed but without grit. With this point as a reference, the drag coefficient penalty of the 0.040-inch grit was 0.0003. Thus, the drag coefficients presented in this report are high by an amount of at least 0.0003 (the theoretical penalty of the 0.040-inch grit was 0.0010) because of the grit used to fix transition.

REFERENCES

1. Holdaway, George H., Mellenthin, Jack A., and Hatfield, Elaine.W.: Investigation at Mach Numbers of 0.20 to 3.50 of a Blended Diamond Wing and Body Combination of Sonic Design but With Low Wave-Drag Increase With Increasing Mach Number. NASA TM X-105, 1959.

2. Chapman, Dean R.: Reduction of Profile Drag at Supersonic Velocities by the Use of Airfoil Sections Having a Blunt Trailing Edge. NACA TN 3503, 1955.

3. Glauert, H.: The Elements of Aerofoil and Airscrew Theory. Cambridge Univ. Press, 1937.

4. Holdaway, George H., and Mersman, William A.: Application of Tchebichef Form of Harmonic Analysis to the Calculation of Zero-Lift Wave Drag of Wing-Body-Tail Combinations. NACA RM A55J28, 1956.

5. Love, Eugene S.: Base Pressure at Supersonic Speeds on Two-Dimensional Airfoils and on Bodies of Revolution With and Without Fins Having Turbulent Boundary Layers. NACA TN 3819, 1957.

6. Puckett, A. E., and Stewart, H. J.: Aerodynamic Performance of Delta Wings at Supersonic Speeds. Jour. Aero. Sci., vol. 14, no. 10, Oct. 1947, pp. 567-578.

7. Donovan, A. F., and Lawrence, H. R.: Aerodynamic Components of Aircraft at High Speeds. Princeton Univ. Press, 1957. (High Speed Aerodynamics and Jet Propulsion, vol. VII, pp. 100, 197-226)

8. Sears, William R.: On Projectiles of Minimum Wave Drag. Quart. Appl. Math., vol. IV, no. 4, Jan. 1947, pp. 361-366.

9. Loving, Donald L., and Katzoff, S.: The Fluorescent-Oil Film Method and Other Techniques for Boundary-Layer Flow Visualization. NASA MEMO 3-17-59L, 1959.

TABLE I.- COORDINATES FOR BODIES, INCHES

M = 1.00 equivalent body		Diamond model		Delta model with bump		Delta model without bump		Arrow model	
x	r	x	r	x	r	x	r	x	r
0	0	(1)		(1)		Same as delta model with rearward body bump		Wing alone	
.375	.075								
.750	.143								
1.500	.263								
2.250	.356								
3.000	.449							3.150	0.311
3.750	.542							4.000	von Kármán .371
4.500	.623							4.200	ogive (2) .424
5.250	.693							5.600	.474
6.000	.761								
6.750	.830							6.400	.522
7.500	.903							7.200	.569
8.250	.976								
9.000	1.048							8.800	.614
9.750	1.116								
10.500	1.179							10.400	.739
11.250	1.238			10.683	1.190				
12.000	1.296			11.000	1.210			12.000	.826
12.750	1.353			12.000 Blended body	1.216				
13.125	1.388			13.000	1.169				
13.875	1.443			14.000	1.099			13.600	.890
14.625	1.509								
15.375	1.570			15.000	1.057			15.200	.960
16.125	1.630			16.000	1.035				
16.875	1.688			16.800	1.026			16.800	1.026
17.500	1.733			von Kármán					
18.000	1.762			18.400 ogive (2)	1.039			18.400	1.039
19.000	1.823			19.200	1.119			19.200	1.119
19.875	1.896	19.360	1.360						
20.625	1.948	20.000 Blended body	1.474	20.000	1.149			20.000	1.149
21.375	2.000	21.000	1.825	20.800	1.178			20.800	1.178
22.125	2.054	22.000	1.712	21.600	1.206			21.600	1.206
23.625	2.156	24.000	1.471	23.200	1.260			23.200	1.260
24.375	2.221	24.800	1.392	24.800	1.311			24.800	1.311
25.125	2.275	25.000	1.347						
25.625	2.374	25.400 von Kármán	1.360	25.400	1.360			25.400	1.360
27.375	2.480	28.000 ogive (2)	1.405	28.000	1.405			28.000	1.405
28.125	2.404	29.600	1.447	29.600	1.447			29.600	1.447
29.625	2.555	31.200	1.487	31.200	1.487			31.200	1.487
30.375	2.603	32.800	1.522	32.800	1.522			32.800	1.522
31.125	2.655	33.600	1.539	33.600	1.539			33.600	1.539
32.625	2.765	34.400	1.554	34.400	1.554			34.400	1.554
33.375	2.820	35.200	1.569	35.200	1.569			35.250	1.570
34.125	2.873	36.000	1.582	36.000	1.582			36.000 Blended body	1.620
35.625	2.957	36.800	1.594	36.800	1.594			37.000	1.660
36.375	2.984	37.600	1.605	37.600	1.605			37.000	1.690
37.500	3.000	38.400	1.614	38.400	1.614				
38.625	2.984	39.200	1.621	39.200	1.621			39.000	1.705
39.375	2.957	40.000	1.625	40.000	1.625	40.000	1.625	40.000	1.715
40.125	2.919	Cylinder		Cylinder		Cylinder		40.500	1.725
41.625	2.820							41.000	1.735
42.375	2.765			42.033	1.625			41.532	1.751
43.125	2.709			43.000 Blended body	1.993			42.000	1.776
44.625	2.603			44.000	2.206			43.000	1.821
45.375	2.555			45.000	2.348			45.000	1.909
46.125	2.509			46.000	2.420				
46.875	2.464			47.000	2.454			47.000	1.975
47.625	2.420			47.898	2.406				
48.000	2.400			(1)					
48.375	2.374								
49.125	2.328							49.000	2.011
49.875	2.279								
50.625	2.221								
51.375	2.166	51.000	1.625					51.000	2.000
52.125	2.110	52.000 Blended body	1.657						
52.875	2.054	53.000	1.730					53.000	1.942
53.625	2.000	54.000	1.827						
54.375	1.944	55.000	1.878			54.100	1.625		
55.125	1.890	55.840	1.900			54.500 Fillet	1.637	55.000	1.872
55.875	1.840	(1)				55.000	1.651	56.000	1.825
56.625	1.795					56.000	1.681	57.000	1.767
57.300	1.747					57.000	1.711	57.500	1.750
57.600	1.728					57.500	1.728	57.600	1.728
57.900	1.709					(1)		(1)	
58.200	1.692								
58.500	1.677								
58.800	1.662								
59.100	1.649								
59.400	1.637								
59.700	1.629								
60.000	1.625								

[1]Same as M = 1.00 equivalent body

[2]Part of a von Kármán ogive (l = 40 in. and r_b = 1.625 in.)

TABLE II.- COORDINATES FOR DIAMOND WING, INCHES

	Semithickness, ±t/2											
y / x	0	±2.000	±4.000	±6.667	±8.000	±12.000	±13.333	±14.000	±16.000	±18.000	±19.000	±20.000
17.500	0											
18.000	.470											
18.500	.685											
19.000	.825											
19.500	.926	0										
20.000	1.010	.202										
20.500	1.047	.349										
21.000	1.070	.459										
21.500	1.089	.545	0									
22.000	1.098	.610	.122									
23.000	1.086	.691	.296									
24.000	1.050	.727	.404	24.167=0								
25.000	.996	.730	.465									
25.500					0							
26.000	.925	.707	.490	.199	.054							
27.000	.858	.677	.496		.135							
28.000	.799	.647	.495	.292	.190							
29.000	.755	.624	.492		.230							
29.500						0						
30.000	.724	.608	.492	.338	.261	.029	30.833=0					
31.000	.702	.598	.494		.286	.078						
31.500								0				
32.000	.685	.591	.496	.370	.307	.118	.055	.024				
33.000	.677	.590	.502		.328	.153		.066				
33.500									0			
34.000	.670	.589	.508	.399	.345	.183	.129	.102	.020			
35.000	.661	.585	.510		.359	.208		.132	.057			
35.500										0		
36.000	.640	.571	.502	.409	.363	.225	.179	.156	.086	.017		
36.500											0	
37.000	.612	.549	.486		.361	.235		.173	.110	.047	.016	
37.500	.594	.535	.475	.396	.356	.238	.198	.178	.119	.059	.030	0
38.000	.610	.547	.485		.360	.235		.172	.109	.047	.016	
38.500											0	
39.000	.631	.563	.495	.404	.358	.222	.176	.153	.085	.017		
39.500										0		
40.000	.643	.569	.496		.349	.202		.129	.055			
41.000	.649	.570	.492	.386	.334	.177	.124	.098	.020			
41.500									0			
42.000	.650	.566	.482		.315	.147		.063				
43.000	.649	.560	.470	.351	.291	.112	.052	.022				
43.500								0				
44.000	.655	.558	.461		.267	.073	44.167=0					
45.000	.667	.560	.454	.311	.240	.027						
45.500						0						
46.000	.683	.564	.445		.208							
47.000	.710	.575	.440	.259	.169							
48.000	.744	.587	.431		.117							
49.000	.787	.602	.417	.170	.046							
49.500				50.833=0	0							
50.000	.845	.620	.394									
51.000	.924	.640	.356									
51.500	.970	.647	.323									
52.000	1.020	.649	.278									
52.500	1.048	.629	.210									
53.000	1.061	.590	.118									
53.500	1.065	.533	0									
54.000	1.060	.454										
54.500	1.045	.348										
55.000	1.011	.202										
55.500	.942	0										
56.000	.842											
56.500	.712											
57.000	.500											
57.500	0											

TABLE III.- COORDINATES FOR DELTA WING, INCHES

	Semithickness, ±t/2						
x \ y	0	±2.000	±4.333	±6.667	±10.000	±13.333	±16.667
8.700	0						
9.000	.540						
9.500	.728						
10.000	.835						
10.600	.920						
11.000	.955						
11.500	.987						
12.000	1.000	12.033=0					
12.500	1.000	.123					
13.000	1.000	.225					
13.500	.992	.303					
14.000	.980	.363					
14.500	.966	.411					
15.000	.948	.447					
15.500	.930	.474	15.922=0				
16.000	.910	.495	.010				
16.500	.888	.508	.066				
17.000	.867	.519	.113				
17.500	.844	.525	.151				
18.000	.822	.526	.184				
18.500	.800	.528	.211				
19.000	.780	.528	.233				
19.500	.765	.529	.254	19.811=0			
20.000	.753	.531	.272	.012			
21.000	.735	.536	.303	.071			
22.000	.723	.542	.330	.119			
23.000	.723	.554	.358	.161			
24.000	.721	.564	.381	.197			
25.000	.719	.572	.400	.229	25.367=0		
26.000	.715	.577	.416	.256	.026		
27.000	.710	.581	.430	.279	.063		
28.000	.706	.584	.442	.300	.096		
29.000	.704	.588	.454	.319	.126		
30.000	.704	.594	.465	.337	.153	30.922=0	
31.000	.707	.601	.478	.355	.179	.002	
32.000	.716	.613	.494	.374	.204	.033	
33.000	.730	.630	.513	.396	.229	.062	
34.000	.739	.642	.528	.414	.252	.090	
35.000	.742	.648	.538	.429	.272	.115	
36.000	.739	.649	.544	.438	.288	.138	
37.000	.721	.636	.537	.438	.296	.155	.013
37.500	.706	.625	.529	.434	.297	.162	.025
38.000	.688	.610	.518	.427	.297	.166	.036
39.000	.643	.573	.490	.407	.289	.172	.054
40.000	.593	.530	.456	.383	.277	.172	.067
41.000	.535	.480	.415	.351	.259	.167	.075
41.500	.506	.455	.395	.335	.249	.163	.077
42.033	.474	.427	.371	.316	.237	.158	.079
42.500	.439	.392	.337	.282	.203	.124	.046
43.000	.400	.353	.299	.244	.166	.088	.010
43.500	.365	.318	.264	.209	.131	.053	43.144=0
44.000	.332	.284	.230	.175	.097	.018	
44.500	.295	.248	.194	.139	.061	44.256=0	
45.000	.261	.214	.159	.104	.026		
45.500	.225	.178	.123	.069	45.367=0		
46.000	.191	.144	.089	.034			
46.500	.155	.108	.053	46.478=0			
47.000	.120	.073	.018				
47.500	.083	.037	47.256=0				
48.000	.050	.002					
48.500	.008	48.033=0					
48.700	0						

TABLE IV.- COORDINATES FOR ARROW WING, INCHES

x \ y	Semithickness, ±t/2										
	0	±2.000	±4.333	±6.667	±10.000	±13.333	±16.667	Ridge		Trailing edge	
								±t/2	±y	±t/2	±y
0.000	0.000										
.500	.086										
1.000	.171										
1.500	.207										
2.000	.237										
2.500	.270										
3.000	.304										
3.500	.337										
4.000	.360										
4.500	.380										
5.000	.395										
5.500	.402										
5.750		0.000									
6.000	.408	.017									
6.500	.414	.048									
7.000	.426	.076									
7.500	.443	.103									
8.000	.467	.131									
9.000	.505	.182									
10.000	.534	.227									
11.000	.552	.263									
12.000	.567	.295									
12.457			0.000								
13.000	.587	.327	.025								
14.000	.610	.359	.067								
15.000	.640	.395	.108								
16.000	.669	.429	.148								
17.000	.688	.455	.184								
17.500	.696	.467	.201								
18.000	.704	.479	.217								
18.500	.712	.491	.233								
19.000	.718	.501	.247								
19.167				0.000							
19.500	.725	.511	.262	.012							
20.000	.731	.521	.276	.030							
21.000	.746	.542	.303	.065							
22.000	.764	.564	.331	.098							
23.000	.789	.592	.362	.131							
24.000	.814	.619	.391	.164							
25.000	.833	.641	.418	.194							
26.000	.851	.663	.443	.224							
27.000	.864	.680	.465	.251							
28.000	.877	.697	.487	.277							
28.750					0.000						
29.000	.890	.714	.508	.302	.008						
30.000	.906	.732	.530	.327	.030						
31.000	.925	.753	.553	.353	.067						
32.000	.948	.778	.579	.380	.096						
33.000	.977	.807	.608	.410	.126						
33.333	.986	.816	.617	.419	.136			0.986	0.000		
34.000	.955	.832	.635	.437	.155			.955	.552		
34.500	.932	.845	.648	.450	.169			.932	.966		
35.000	.908	.853	.657	.462	.182			.905	1.379		
35.230	.898	.855	.661	.466	.188			.891	1.570		
35.750		[1].853									
36.000	.852	.839	.665	.476	.205			.838	2.207		
36.500	.815	.805	.666	.480	.215			.802	2.621		

[1]Ridge

TABLE IV.- COORDINATES FOR ARROW WING, INCHES - Concluded

Semithickness, ±t/2											
x \ y	0	±2.000	±4.333	±6.667	±10.000	±13.333	±16.667	Ridge		Trailing edge	
								±t/2	±y	±t/2	±y
37.000	0.768	0.769	0.668	0.486	0.225			0.770	3.034		
37.500	.710	.725	.668	.489	.233			.736	3.448		
38.000	.642	.674	.668	.492	.242			.703	3.862		
38.333						0.000					
38.500	.576	.620	.667	.495	.250	.004		.671	4.276		
38.569			[1].667								
39.000	.508	.565	.632	.499	.258	.017		.642	4.690		
39.500	.445	.509	.584	.499	.264	.029		.609	5.103		
40.000	.387	.458	.540	.502	.271	.040		.582	5.517	0.387	0
40.500		.397	.493	.508	.280	.052		.558	5.931	.339	.571
41.000		.338	.441	.508	.285	.062		.530	6.345	.300	1.143
41.389				[1].513							
41.532		.268	.386	.504	.295	.074		.509	6.785	.255	1.750
41.750		.251									
42.000			.350	.468	.306	.085		.494	7.172	.247	2.286
42.500			.314	.432	.318	.096		.473	7.586	.239	2.857
43.000			.277	.395	.329	.108		.462	8.000	.231	3.429
43.791			.218								
44.000				.371	.352	.131		.430	8.828	.215	4.571
45.000				.247	.375	.154		.398	9.655	.199	5.714
45.417					[1].385						
45.833				.186							
46.000					.342	.177		.367	10.483	.183	6.857
47.000					.268	.200		.335	11.310	.167	8.000
47.918							0.000				
48.000					.194	.223	.002	.303	12.138	.151	9.143
48.750					.139						
49.000						.247	.025	.271	12.966	.136	10.286
49.444						[1].257					
50.000						.216	.048	.239	13.793	.120	11.429
51.000						.143	.071	.207	14.621	.104	12.571
51.667						.093					
52.000							.094	.175	15.448	.088	13.714
53.000							.117	.143	16.276	.072	14.857
53.473							[1].128				
54.000							.090	.112	17.103	.056	16.000
54.584							.046				
55.000								.080	17.931	.040	17.143
55.500								.064	18.345	.032	17.714
56.000								.048	18.759	.024	18.286
56.500								.032	19.172	.016	18.857
57.000								.016	19.586	.008	19.429
57.500								.000	20.000	.000	20.000

[1]Ridge

TABLE V.- EFFECT OF DOUBLING THE REYNOLDS NUMBER AT M = 0.20 ON THE AERODYNAMIC CHARACTERISTICS OF THE THREE MODELS HAVING DIFFERENT PLAN FORMS (TRANSITION FREE)

(a) Diamond Model

α	C_L		C_D		C_m		L/D	
R/ftx10^{-6}	3.0	6.0	3.0	6.0	3.0	6.0	3.0	6.0
0	-0.004	0.002	0.0059	0.0064	-0.0008	0		
-4.04	-.156	-.164	.0172	.0154	-.0229	-.0242		
-2.03	-.073	-.082	.0090	.0081	-.0113	-.0120		
0	.001	.003	.0063	.0063	.0001	0	0.16	0.48
2.03	.083	.085	.0091	.0087	.0119	.0119	9.12	9.77
4.04	---	.167	---	.0155	---	.0244	---	10.77
4.06	.167	---	.0161	---	.0245	---	10.37	---
6.09	.248	.251	.0282	.0282	.0377	.0383	8.79	8.90
8.12	.330	.337	.0461	.0469	.0510	.0517	7.16	7.19
10.15	.413	.422	.0702	.0719	.0617	.0630	5.88	5.87
12.18	.496	---	.1011	---	.0703	---	4.91	---
12.19	---	.508	---	.1036	---	.0717	---	4.90
14.22	.589	.598	.1412	.1431	.0772	.0781	4.17	4.18
16.25	.686	.685	.1910	.1905	.0834	.0827	3.59	3.60
18.28	.756	.767	.2428	.2458	.0837	.0837	3.11	3.12
20.31	.831	.837	.3027	.3053	.0842	.0843	2.75	2.74
22.33	.885	.901	.3604	.3663	.0768	.0821	2.46	2.46
24.34	.926	.938	.4177	.4226	.0709	.0683	2.22	2.22
26.36	.965	.971	.4764	.4800	.0644	.0621	2.03	2.02
(b) Delta Model								
0	0.005	-0.003	0.0075	0.0065	0.0009	-0.0004		
-4.06	-.161	-.168	.0174	.0169	-.0337	-.0347		
-2.03	-.079	-.077	.0095	.0091	-.0163	-.0152		
0	.003	.007	.0073	.0069	.0007	.0012	0.41	1.01
2.03	.088	.092	.0101	---	.0178	.0185	8.71	---
4.07	.176	.177	.0179	.0170	.0367	.0373	9.83	10.41
6.10	.272	.278	.0327	.0325	.0581	.0587	8.32	8.55
8.14	.366	.376	.0539	.0546	.0799	.0811	6.79	6.89
10.17	.460	.467	.0818	.0825	.1041	.1043	5.62	5.66
12.21	.565	.566	.1194	.1191	.1278	.1273	4.73	4.75
14.25	.662	.673	.1627	.1652	.1505	.1515	4.07	4.07
15.26	---	.712	---	.1869	---	.1606	---	3.81
16.28	.761		.2145		.1731		3.55	
18.31	.849		.2708		.1947		3.14	
20.35	.949		.3389		.2183		2.80	
22.39	1.058		.4203		.2442		2.52	
24.41	1.128		.4934		.2621		2.29	
26.44	1.199		.5740		.2794		2.09	
(c) Arrow Model								
0	0.007	-0.003	0.0085	0.0081	0.0001	-0.0002		
-4.05	-.139	-.144	.0192	.0176	-.0198	-.0200		
-2.02	-.067	-.065	.0111	.0101	-.0085	-.0074		
0	.006	.005	.0085	.0084	0	.0004	0.71	0.60
2.02	.076	.076	.0111	.0105	.0086	.0088	6.85	7.24
4.06	.156	.155	.0190	.0178	.0219	.0218	8.21	8.71
6.09	.240	.239	.0326	.0318	.0370	.0372	7.36	7.52
8.12	.331	.326	.0536	.0517	.0567	.0554	6.18	6.31
10.15	.417	.411	.0819	.0774	.0784	.0760	5.09	5.31
12.19	.507	.505	.1130	.1119	.1026	.1011	4.49	4.51
14.22	---	.605	---	.1546	---	.1288	---	3.91
16.26	.708	.706	.2077	.2062	.1600	.1595	3.41	3.42
18.30	.806		.2666		.1919		3.02	
20.34	.914		.3378		.2282		2.71	
22.37	1.019		.4166		.2637		2.45	
24.41	1.114		.5007		.2976		2.22	
26.44	1.206		.5914		.3311		2.04	

TABLE VI.- THEORETICAL ZERO-LIFT WAVE-DRAG COEFFICIENTS FROM THE PRELIMINARY ANALYSIS USED TO SELECT THE DESIGN AREA DISTRIBUTION

Plan form	Area distribution (see fig. 20)				Drag coefficient, ΔC_{D_o} (N = 25)		
	A_2	A_3	A_4	$A_{n>4}$	$\beta \cos \theta = 0$	$\beta \cos \theta = 0.6633$	$\beta \cos \theta = 3.3541$
Diamond	A_N	A_N	A_N	$N \to \infty$	0.0034	0.0023	0.0040
Diamond	1.696[1]	0	0	0	.0025	.0059	
Diamond	1.405	0	-.727	0	.0026	.0053	
Diamond	1.551	0	-.360	0	.0023	.0053	
Delta	A_N	A_N	A_N	$N \to \infty$	.0034	.0110	.0062
Delta	1.696[1]	0	0	0	.0025	.0190	
Delta	1.551	-.836	0	0	.0030	.0129	
Arrow	A_N	A_N	A_N	$N \to \infty$	.0034	.0079	.0025
Arrow	1.696[1]	0	0	0	.0025	.0105	
Arrow	1.405	0	-.727	0	.0026	.0095	
Arrow	1.551	-.836	0	0	.0030	.0074	

[1]Sears-Haack body, minimum wave drag for given volume and length from linearized theory. See reference 8.

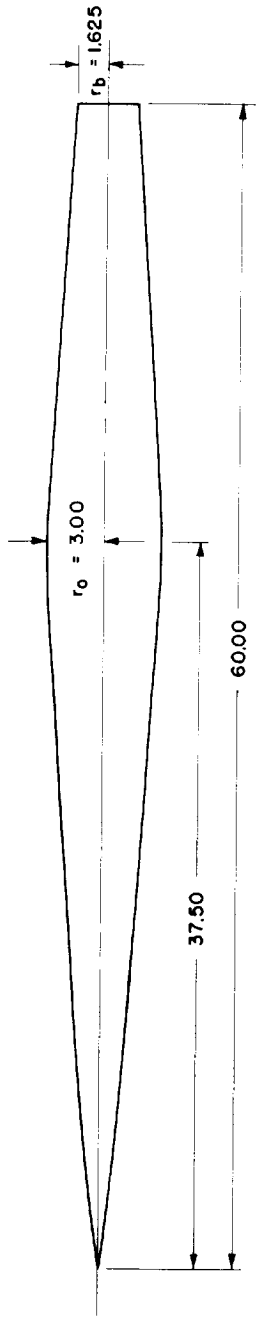

(See table I for ordinates)

(a) M = 1.00 equivalent body.

Figure 1.- Sketches of the models.

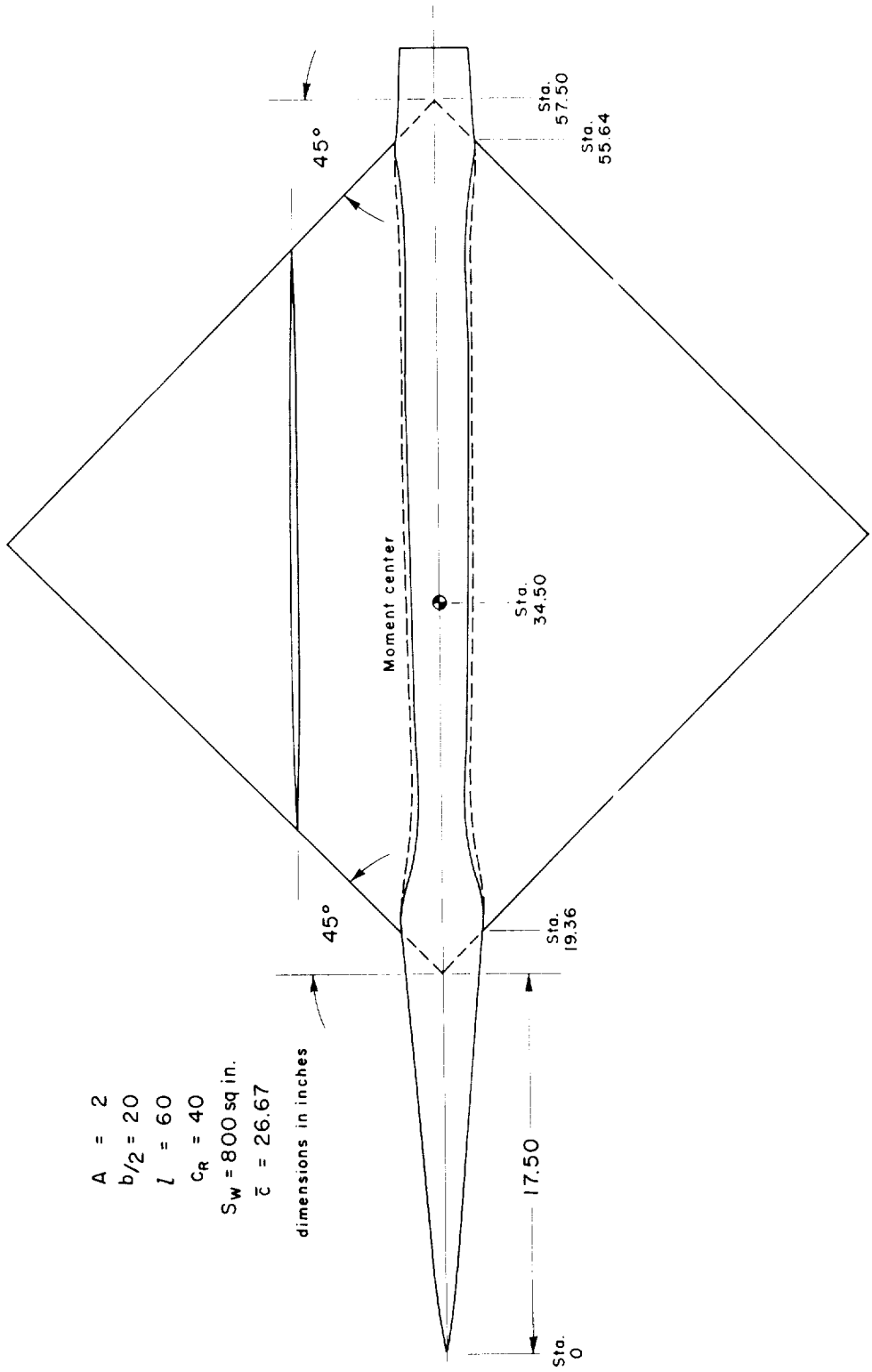

(b) Diamond model.

Figure 1.- Continued.

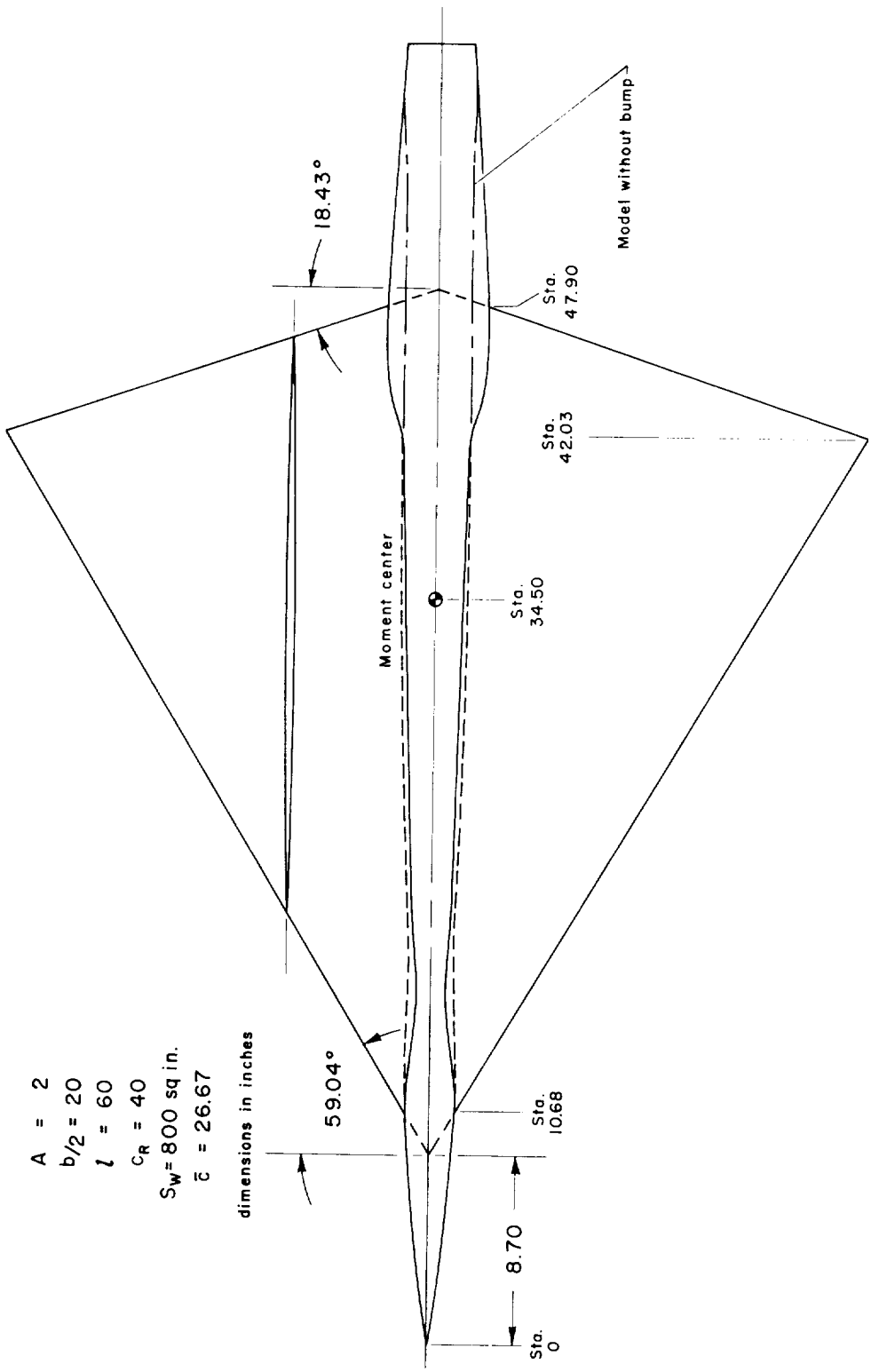

(c) Delta model.

Figure 1.- Continued.

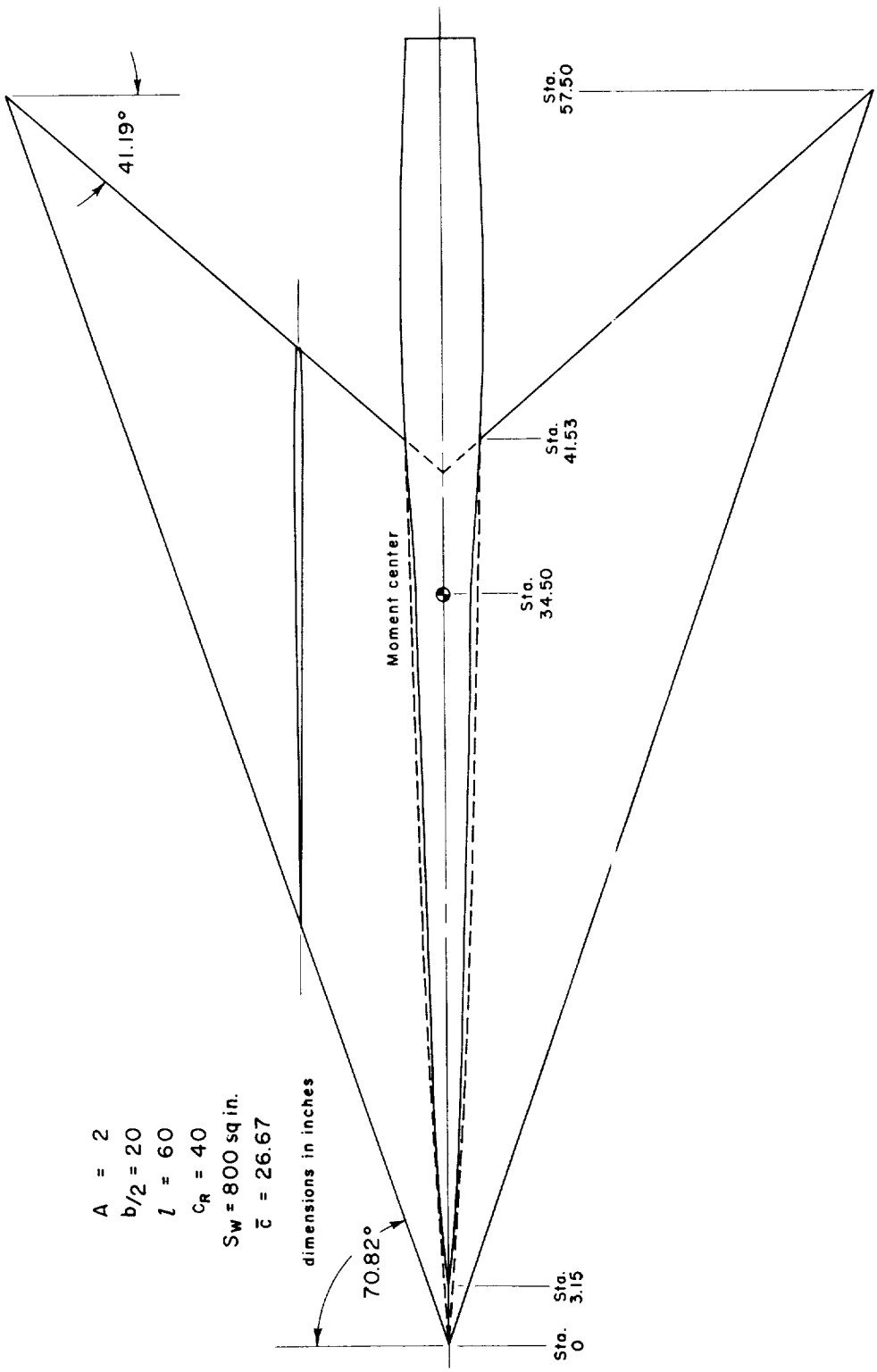

(d) Arrow model.

Figure 1.- Concluded.

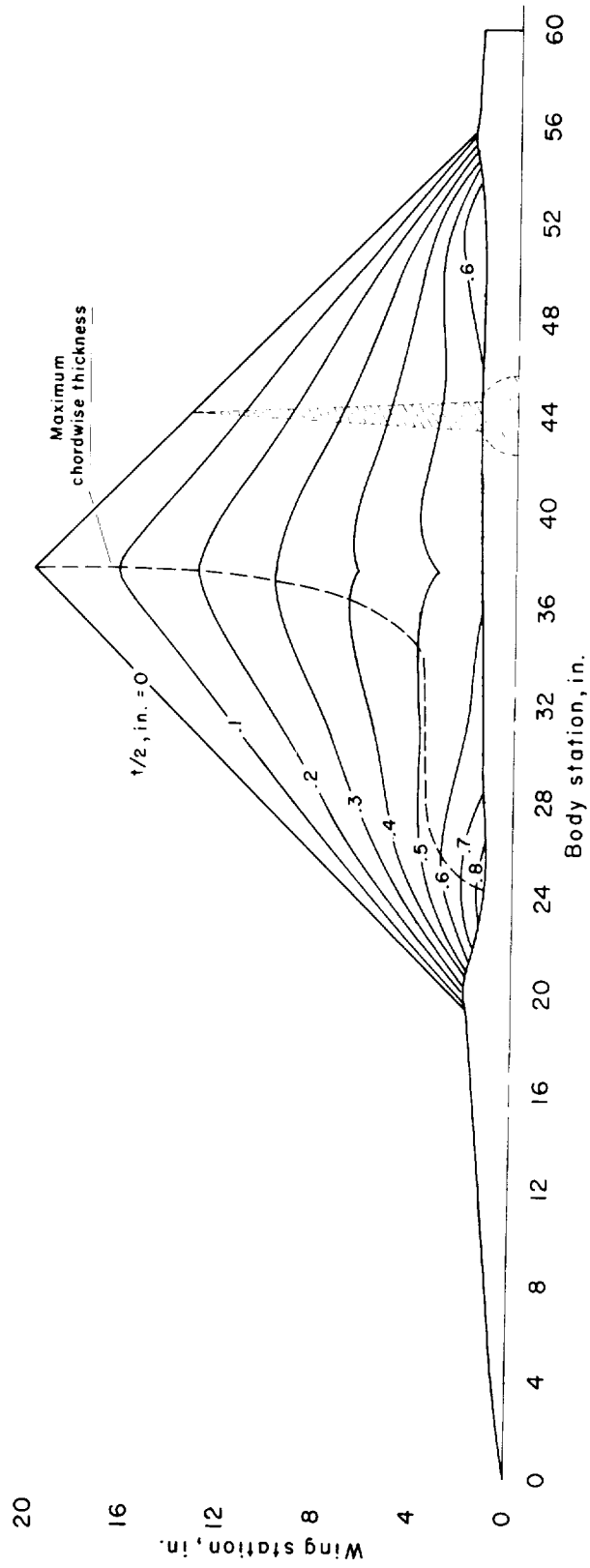

(a) Diamond model.

Figure 2.- Semi-plan view of the models with wing thickness contours.

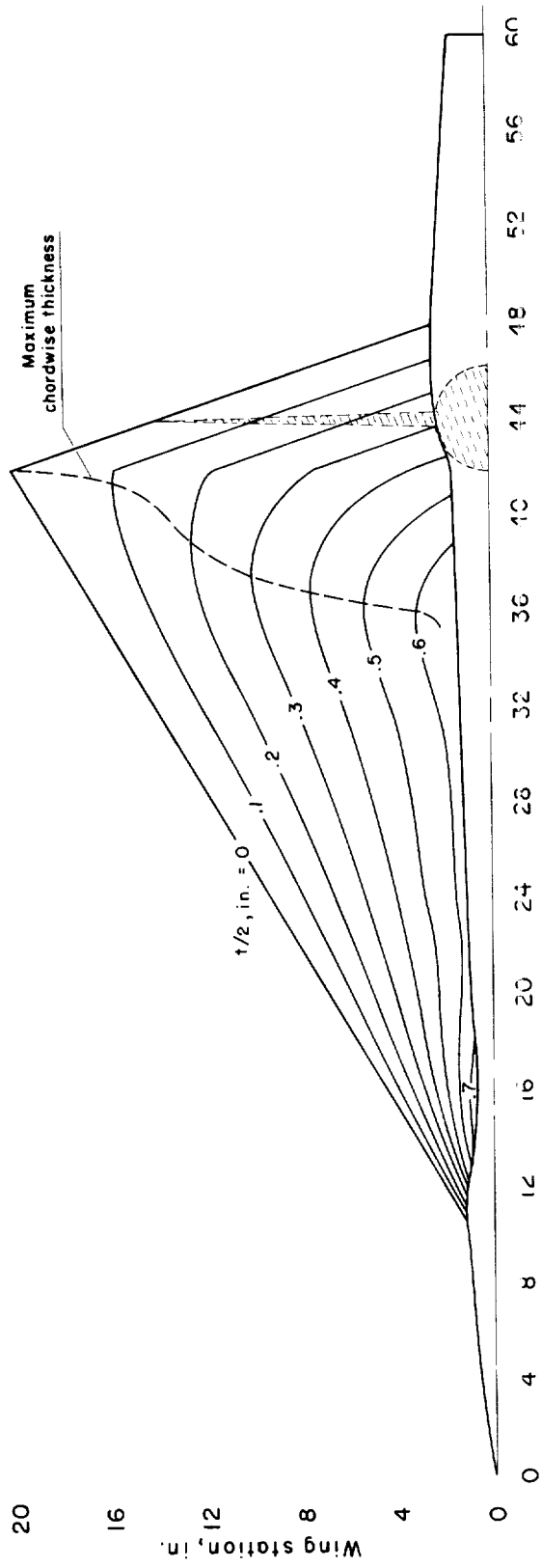

(b) Delta model.

Figure 2.- Continued.

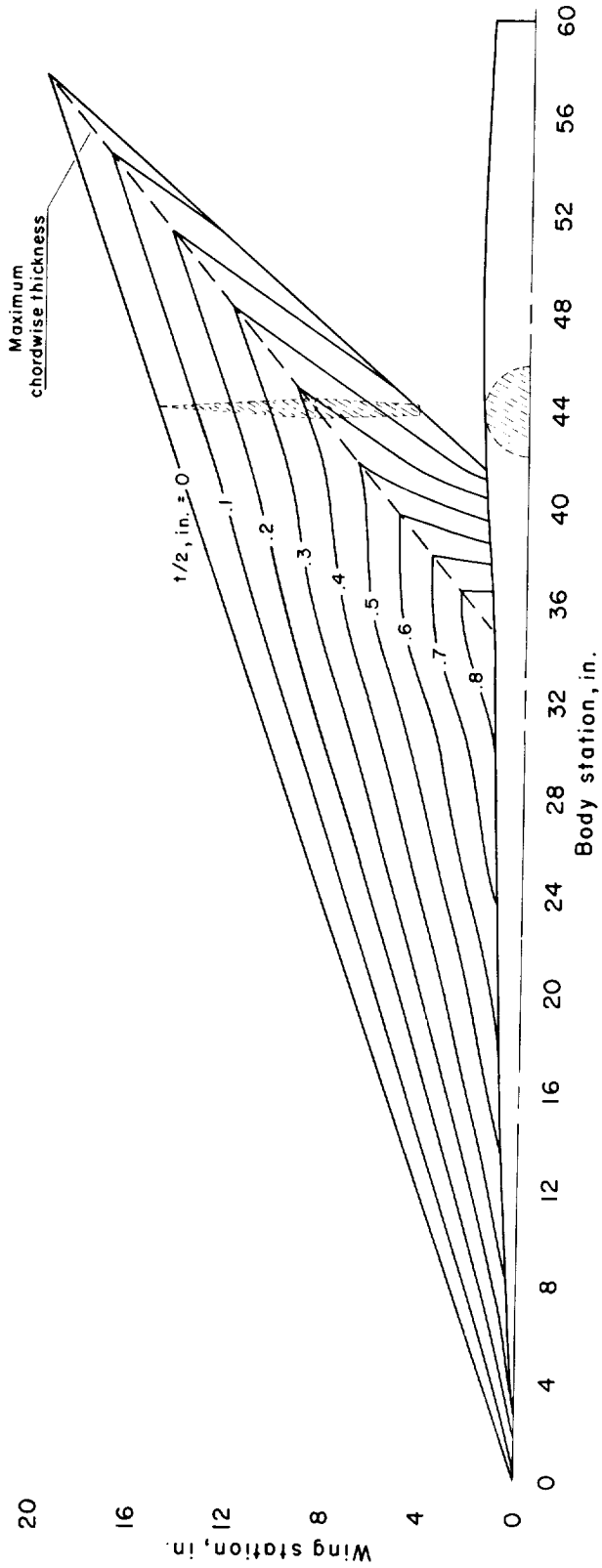

(c) Arrow model.

Figure 2.- Concluded.

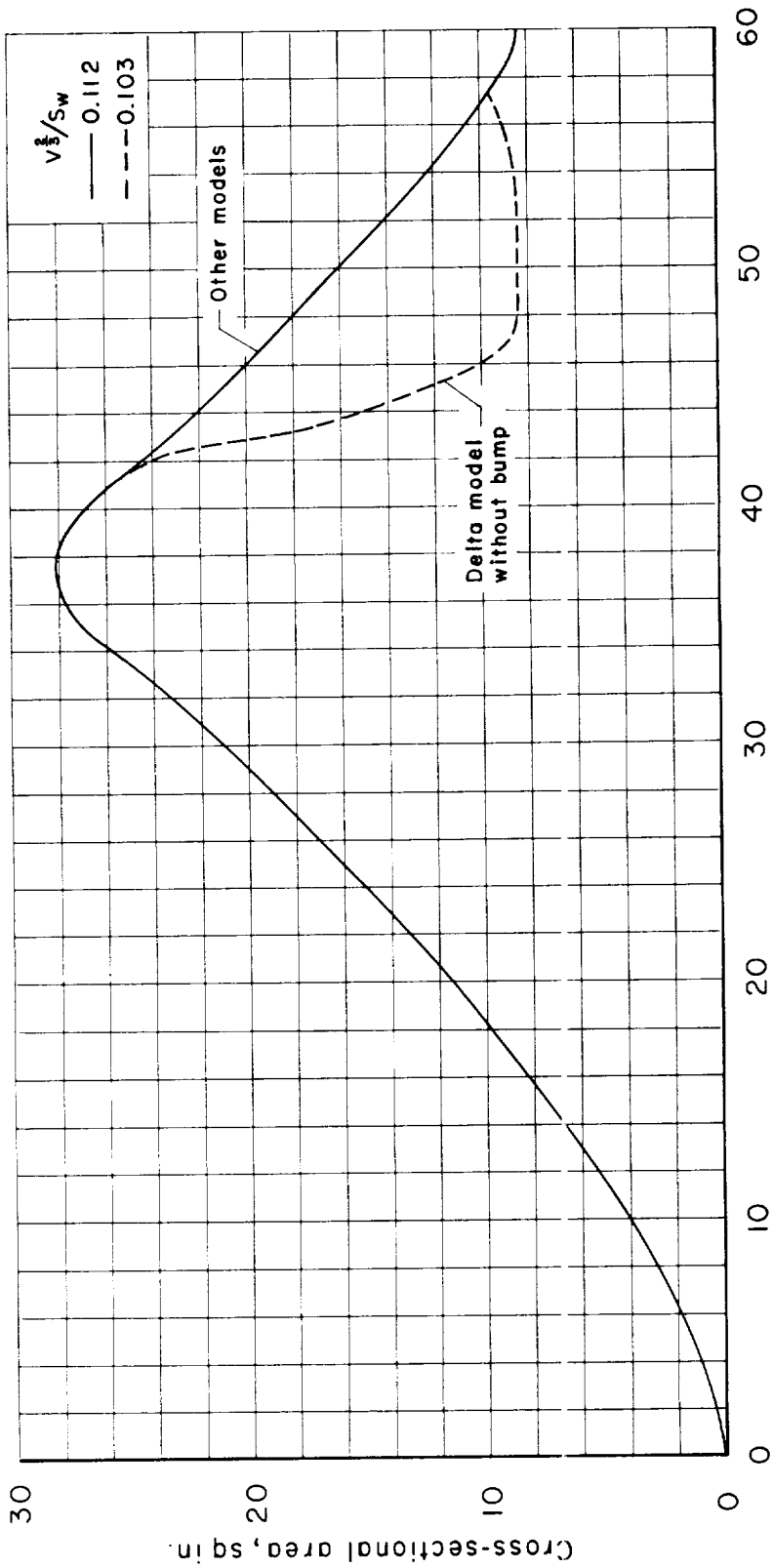

Figure 3.- The design area distribution as derived in reference 1 and modified for the delta model without the body bump.

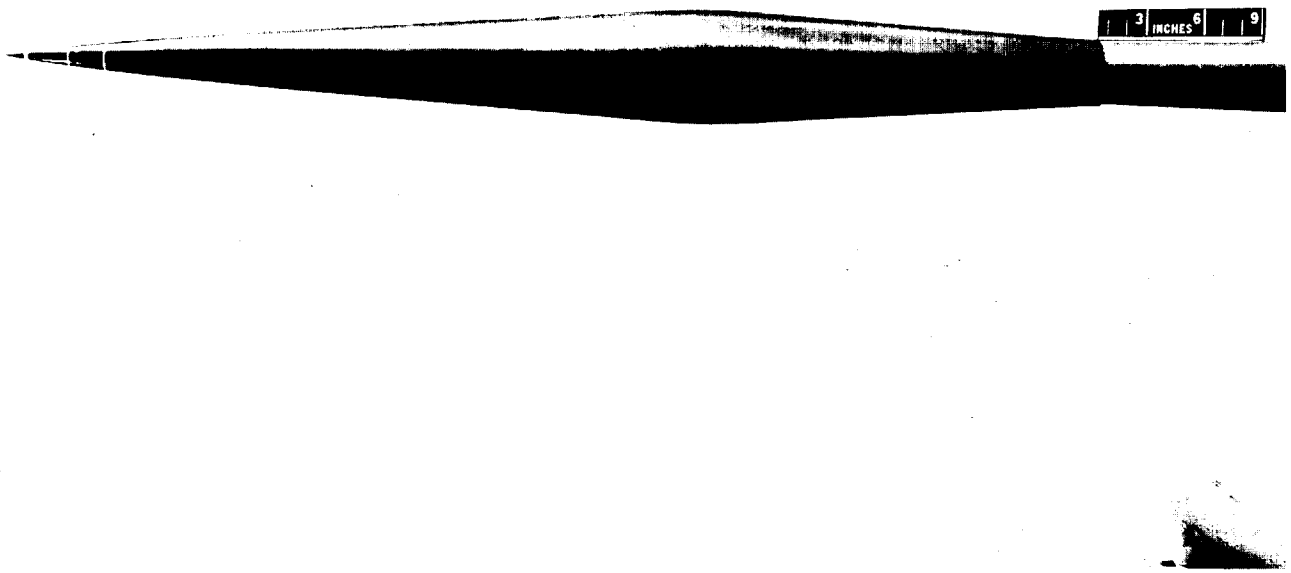

(a) M = 1.00 equivalent body.

Figure 4.- Photographs of the test models.

A-23674

(b) Diamond model in the 8- by 7-foot test section.

Figure 4.- Continued.

A-23953

(c) Delta model without body bump in the 14-foot transonic test section.

Figure 4.- Continued.

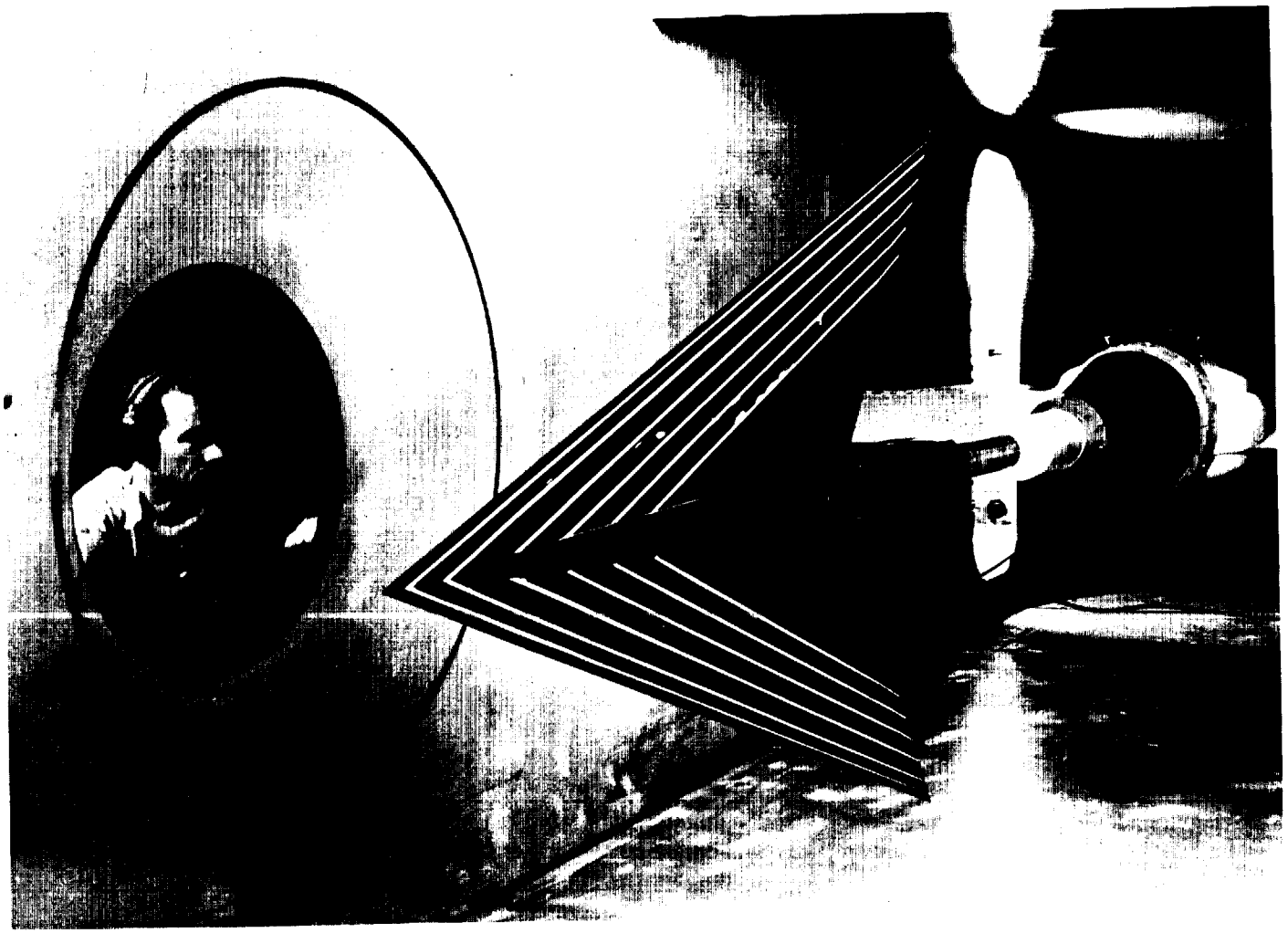

A-25866

(d) Arrow model in the 9- by 7-foot test section.

Figure 4.- Concluded.

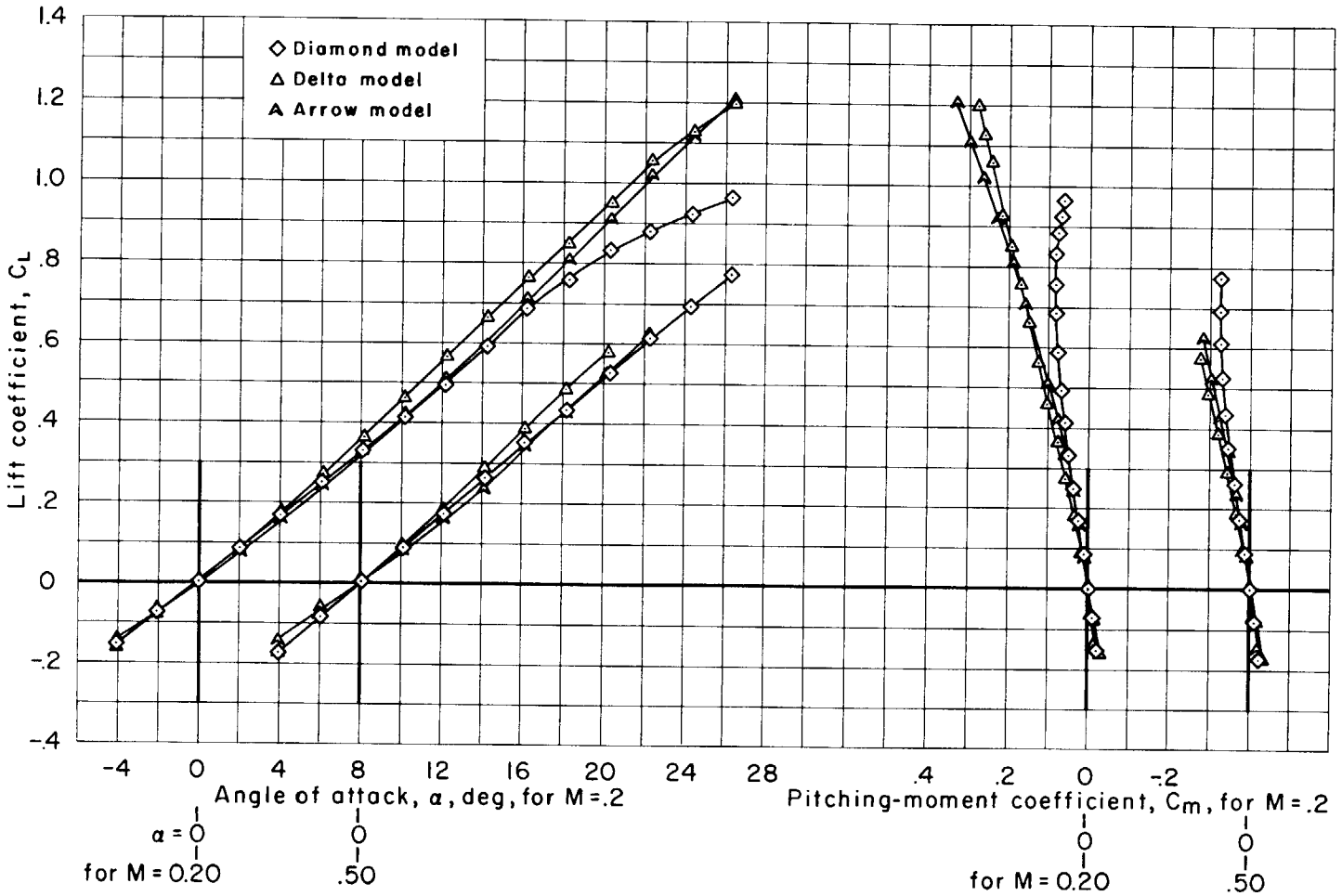

(a) C_L vs. α and C_m

Figure 5.- Subsonic aerodynamic characteristics with transition free as determined from tests in the Ames 12-Foot Pressure Wind Tunnel (R/ft = 3,000,000).

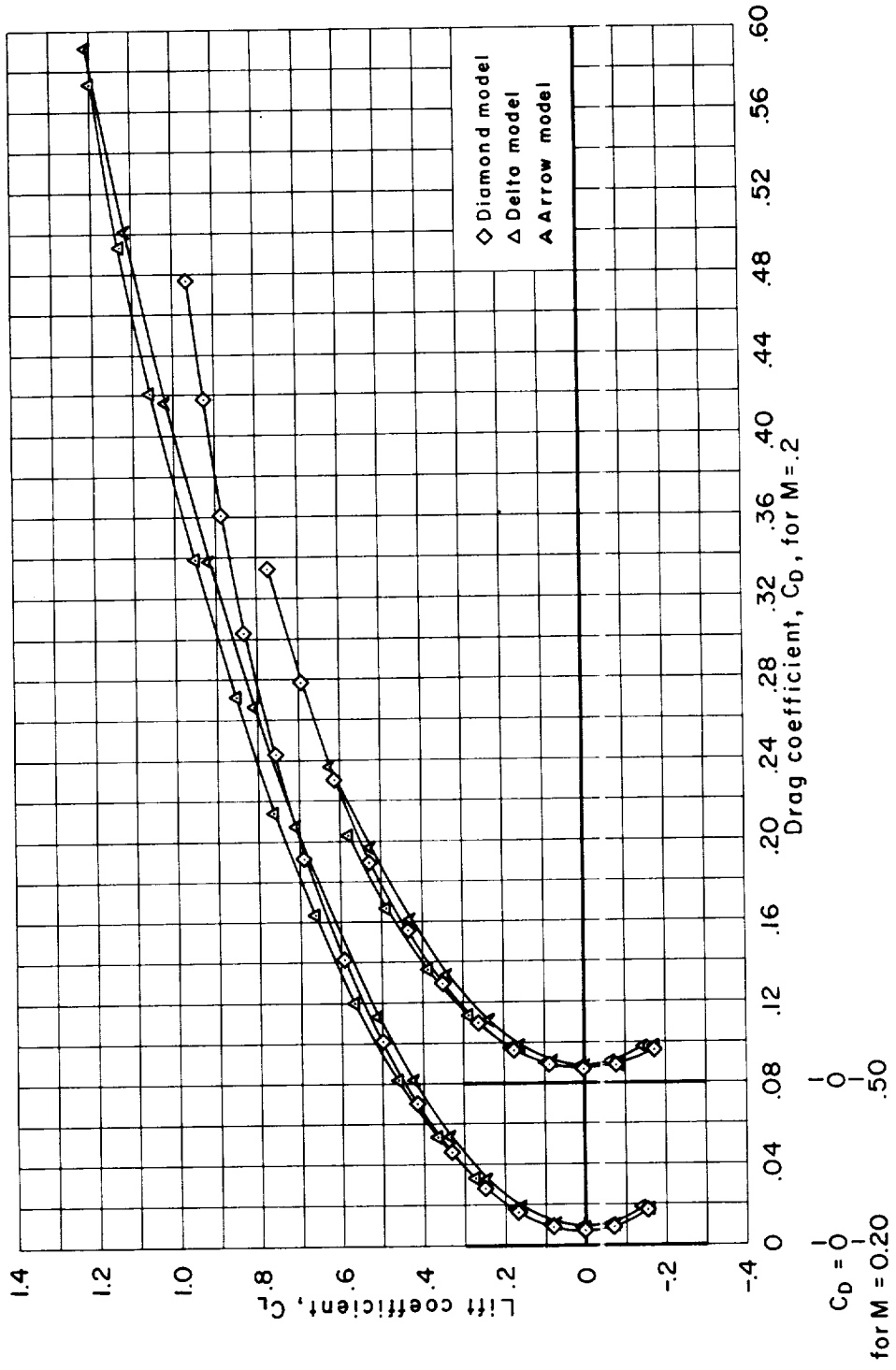

(b) C_L vs. C_D

Figure 5.- Concluded.

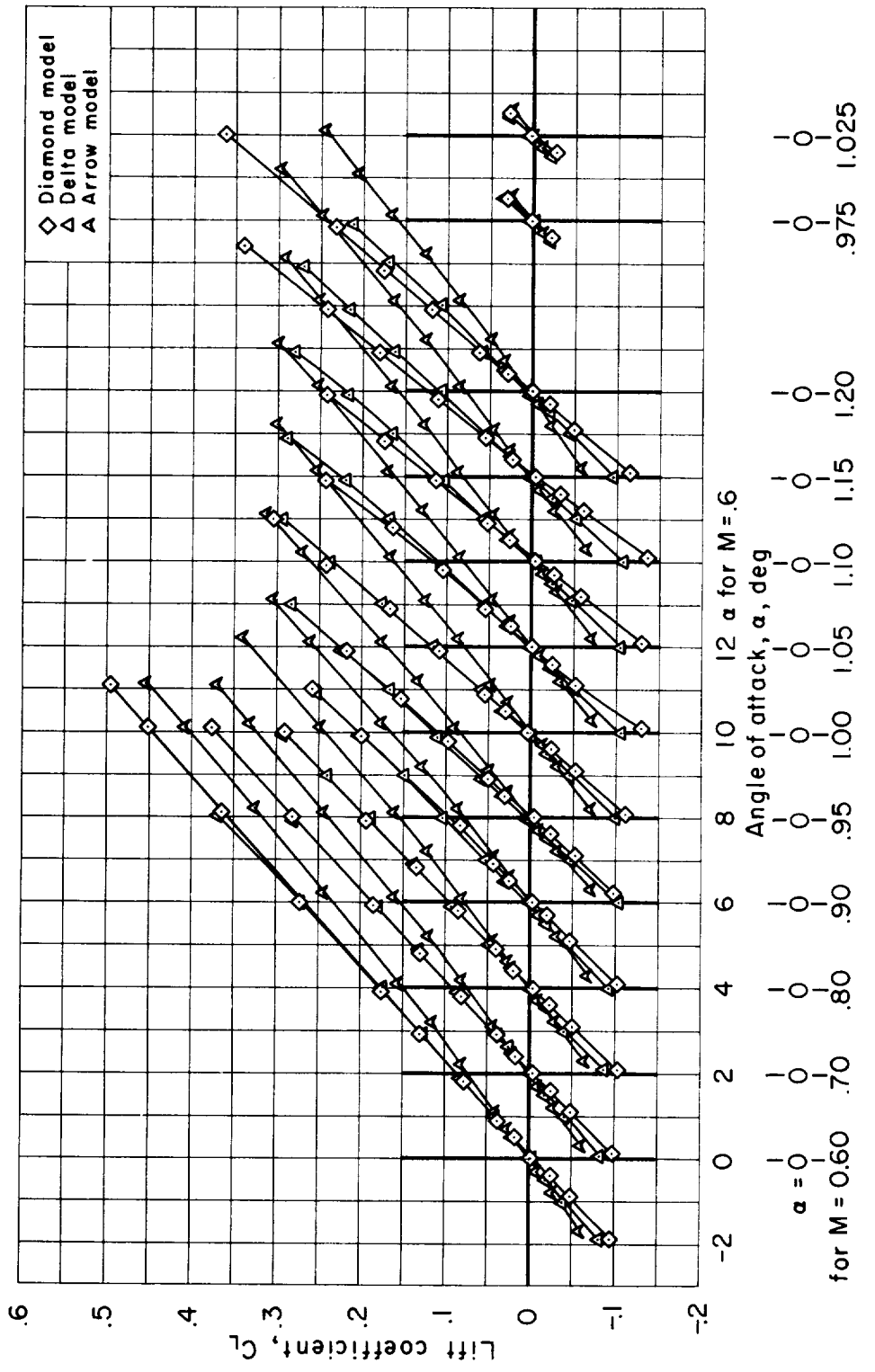

(a) C_L vs. α

Figure 6.- Transonic aerodynamic characteristics with transition fixed as determined from tests in the Ames 14-Foot Transonic Wind Tunnel (R/ft = 3,500,000 to 4,000,000).

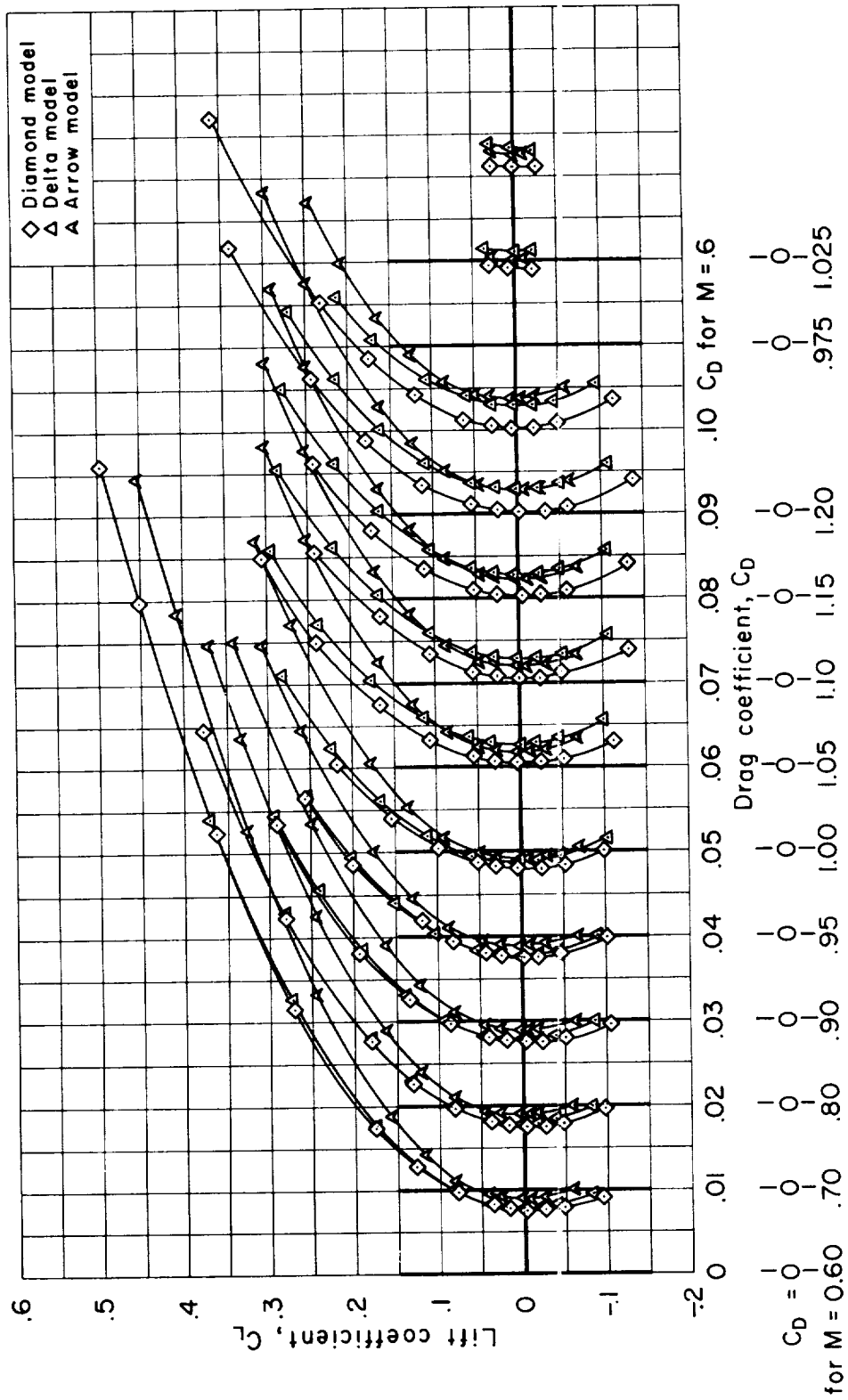

(b) C_L vs. C_D

Figure 6.- Continued.

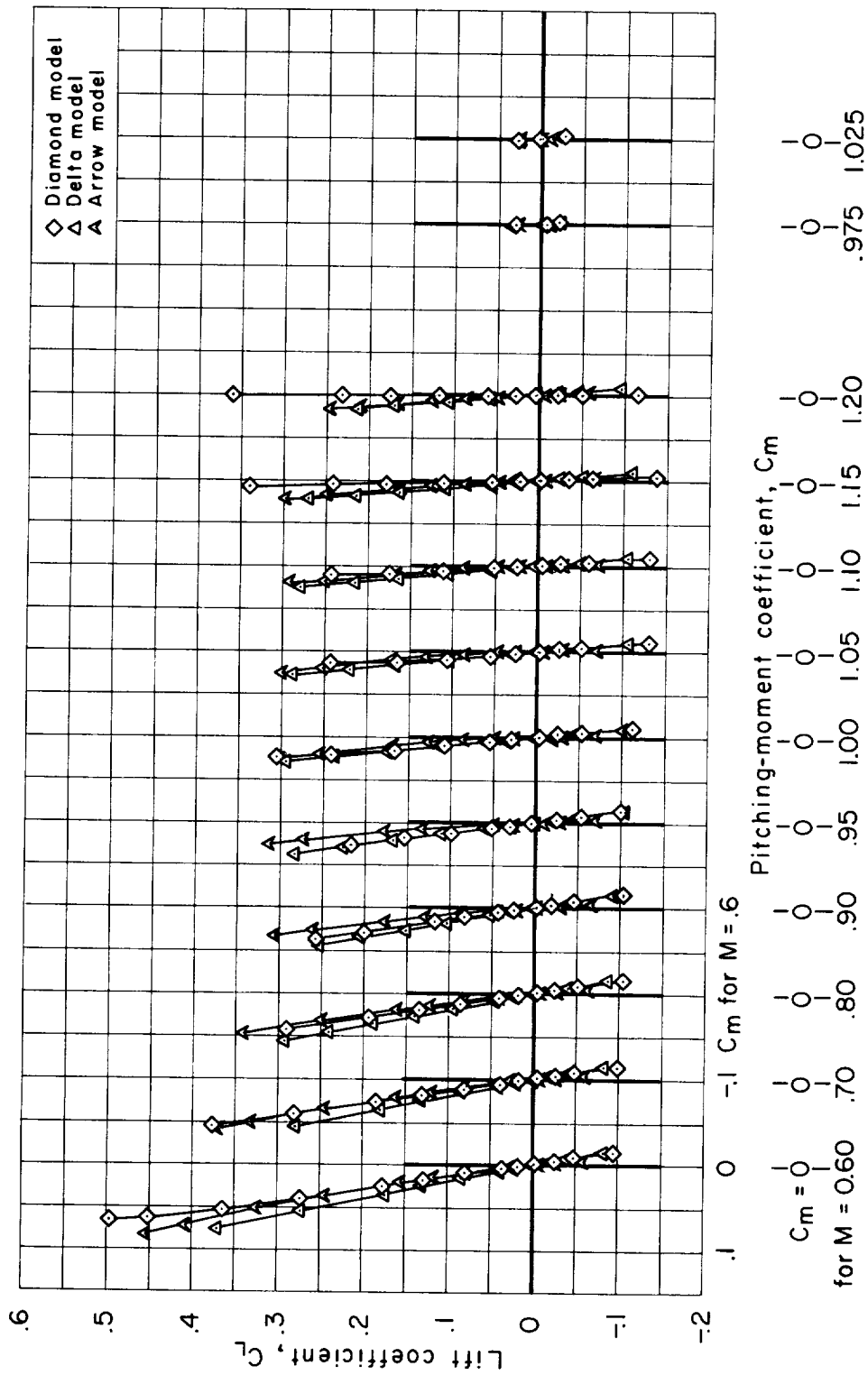

(c) C_L vs. C_m

Figure 6.- Continued.

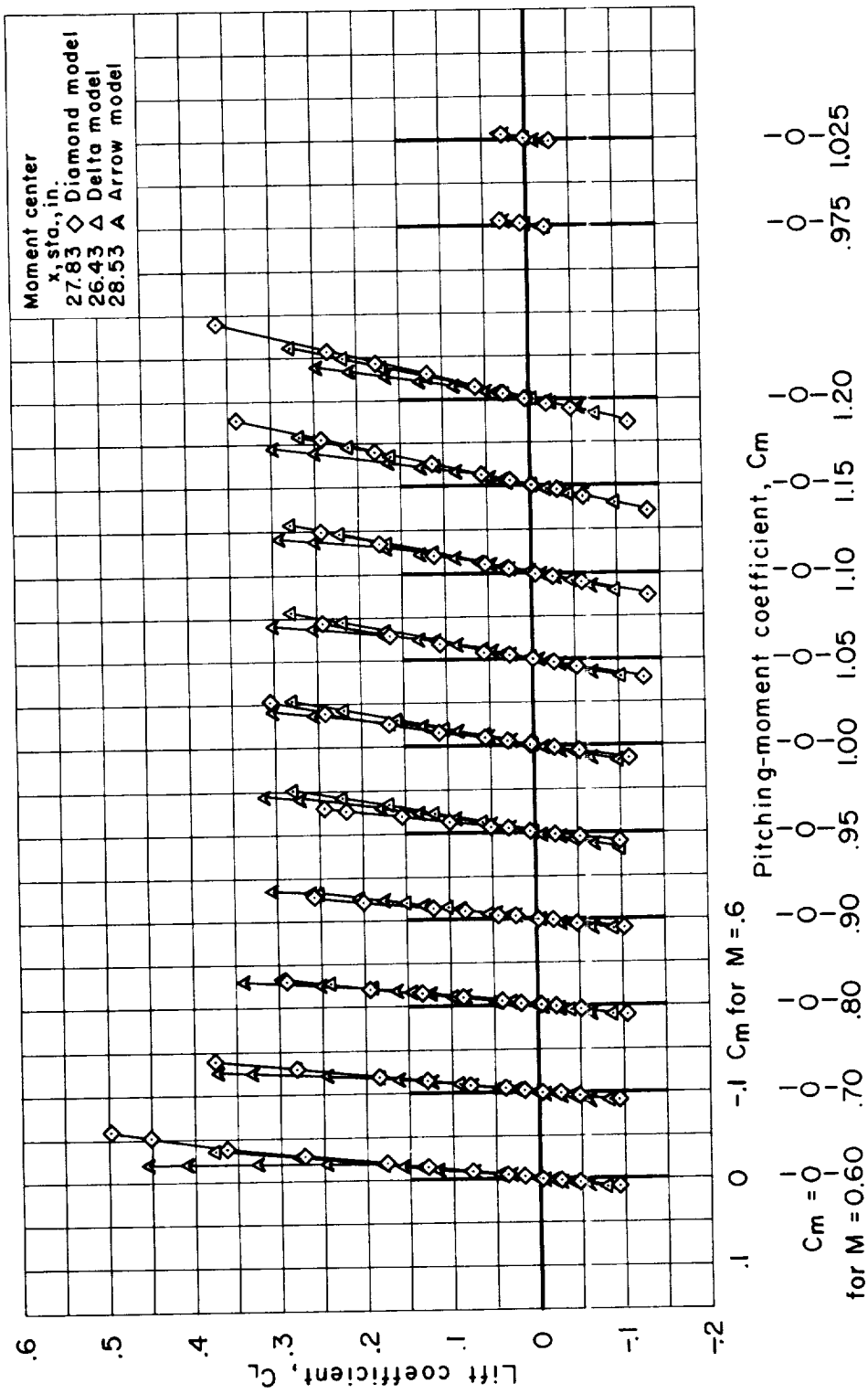

(a) C_L vs. C_m with 10-percent static margin at M = 0.60.

Figure 6.- Concluded.

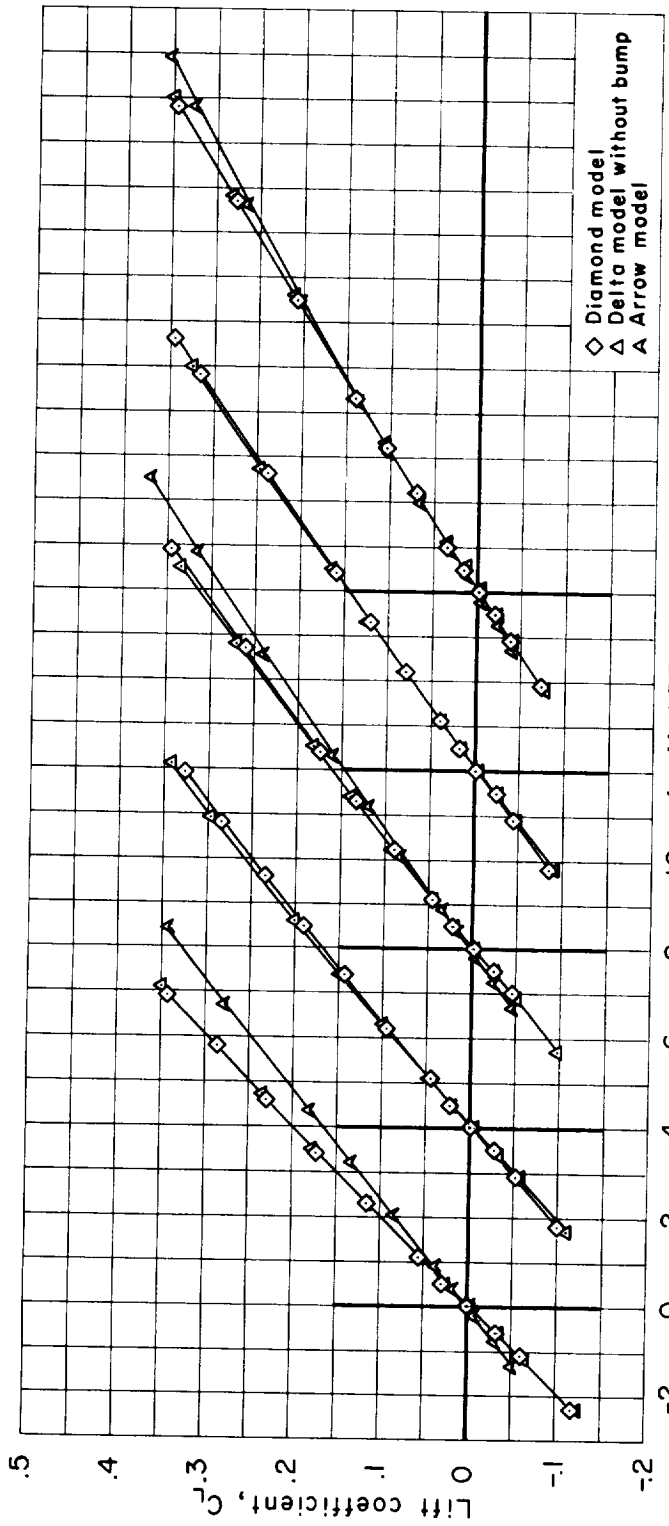

(a) C_L vs. α

Figure 7.- Supersonic aerodynamic characteristics with transition fixed as determined from tests in the 9- by 7-foot supersonic test section (R/ft = 3,000,000).

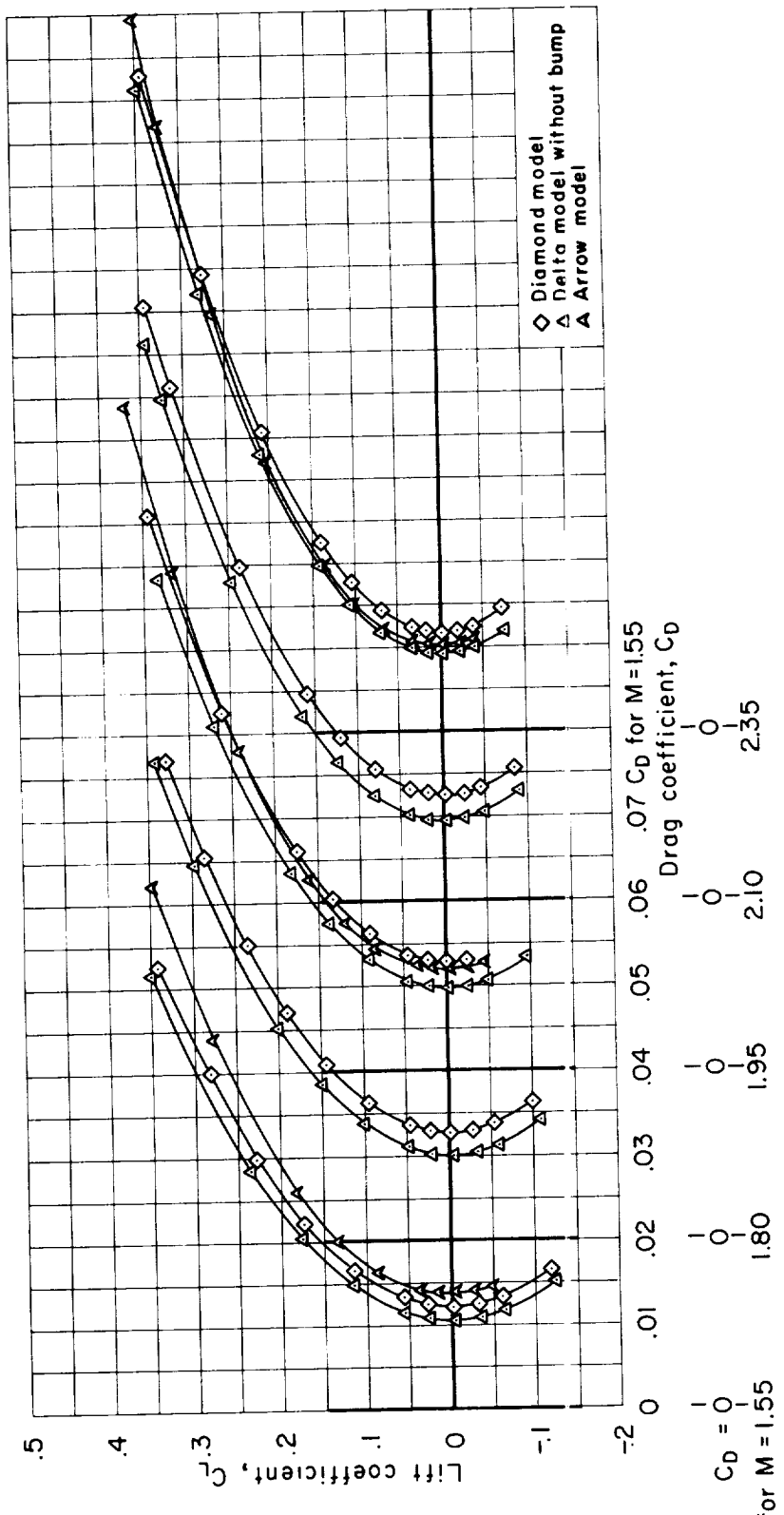

(b) C_L vs. C_D

Figure 7.- Continued.

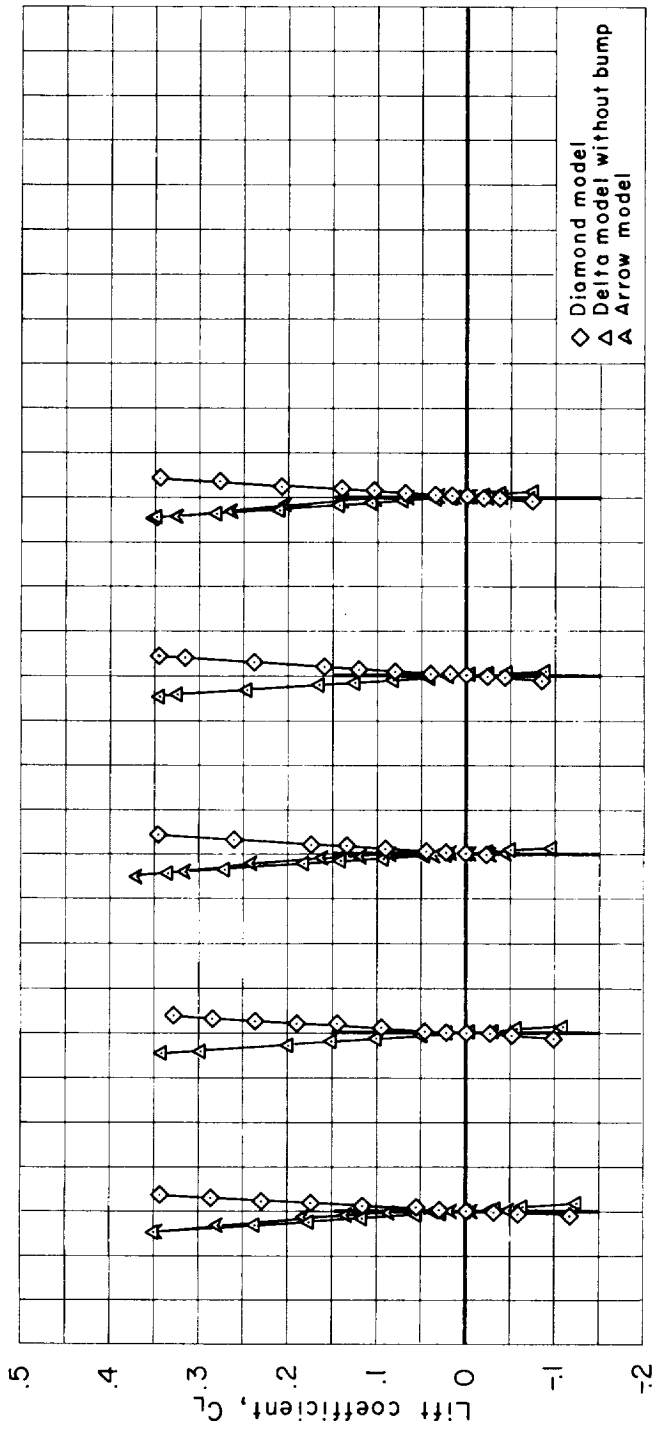

(c) C_L vs. C_m

Figure 7.- Continued.

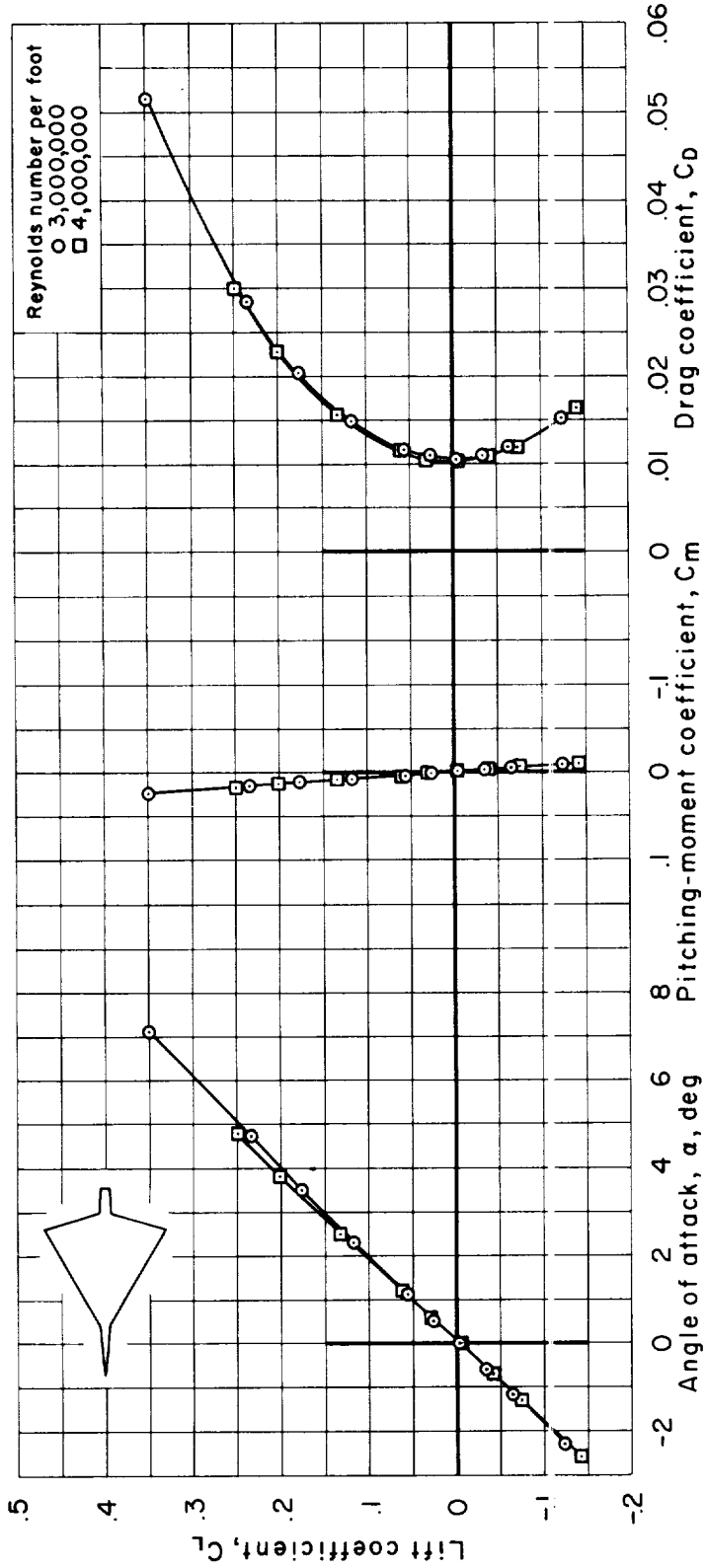

(d) Reynolds number effect at M = 1.55, delta model without bump.

Figure 7.- Continued.

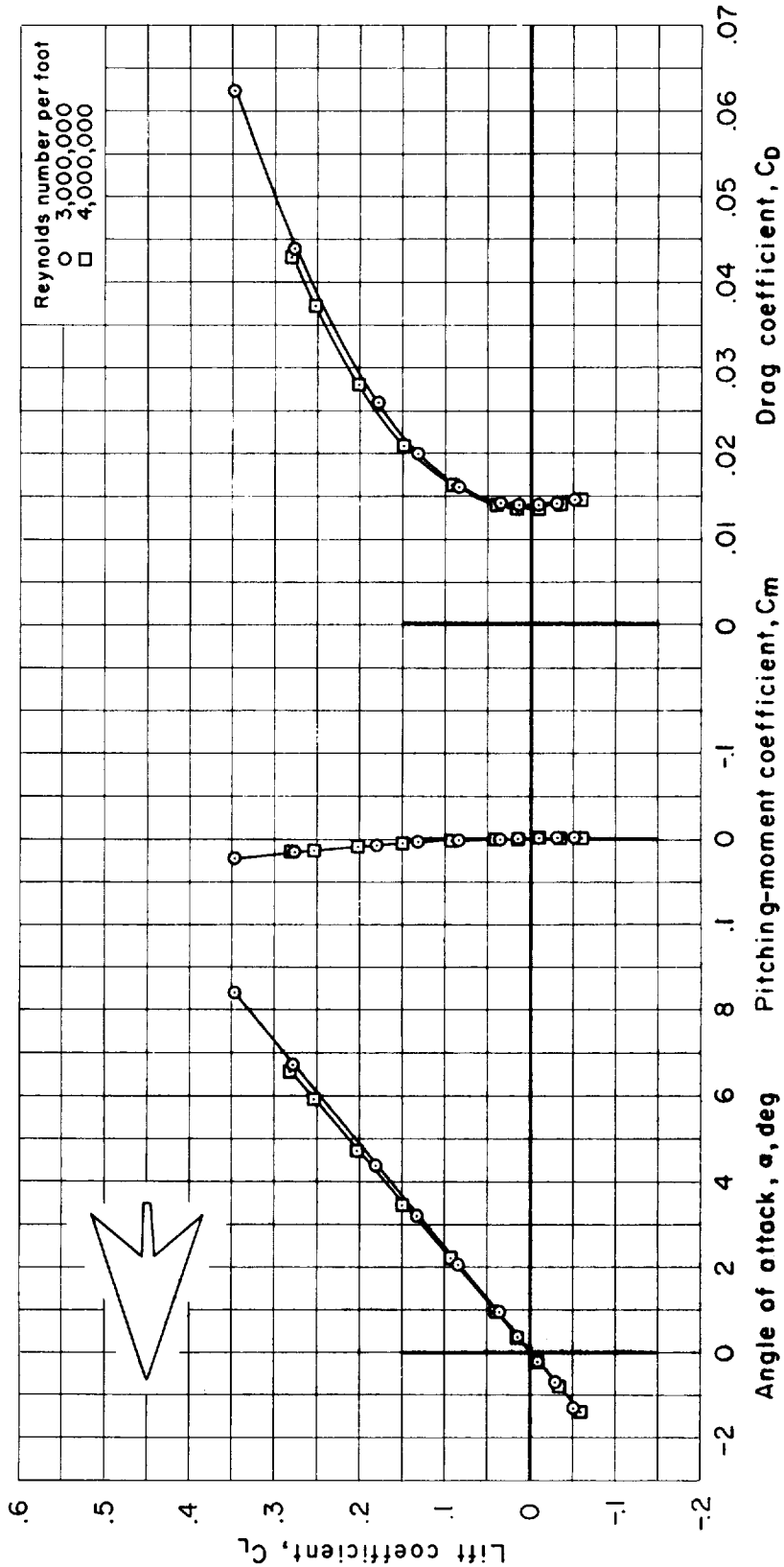

(e) Reynolds number effect at M = 1.55, arrow model.

Figure 7.- Concluded.

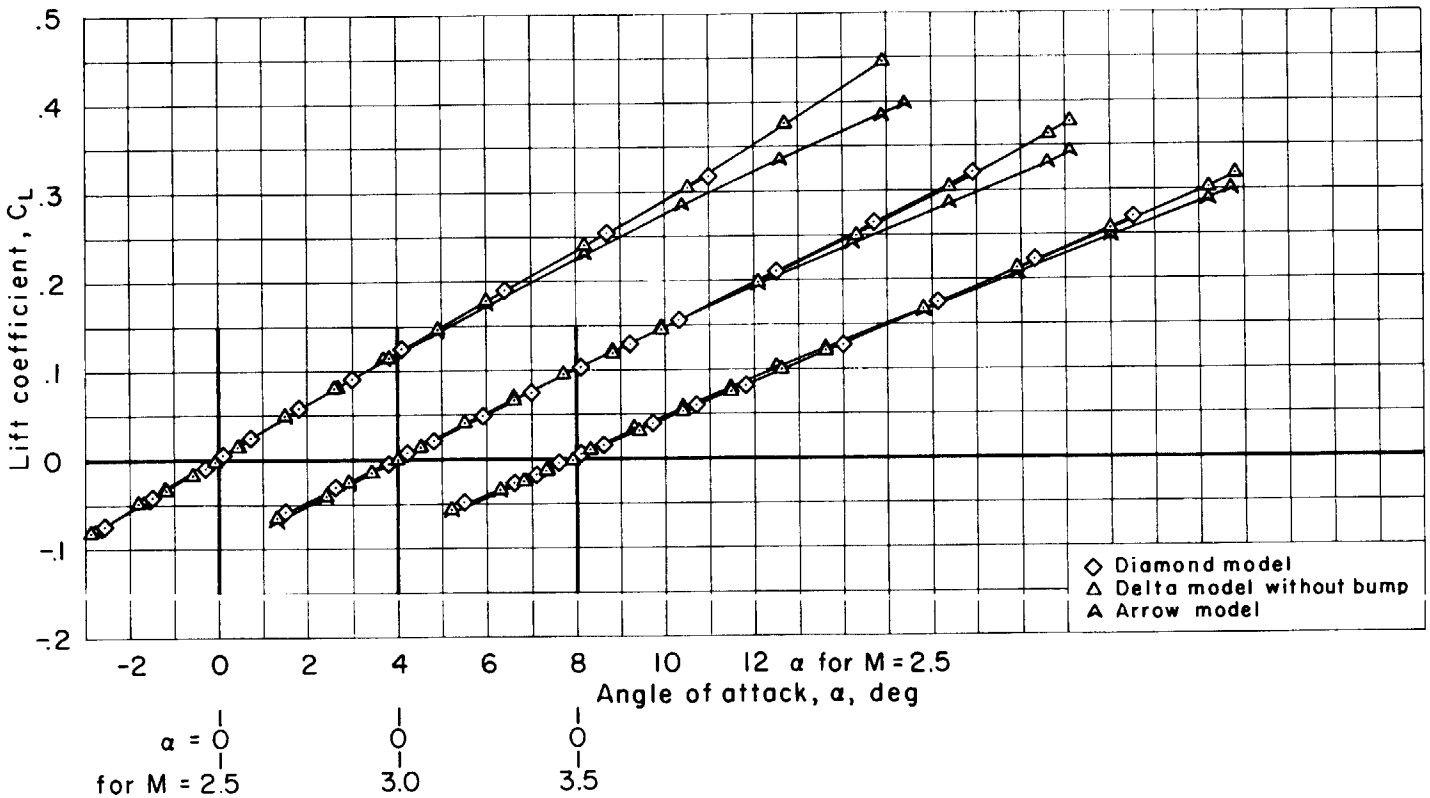

(a) C_L vs. α

Figure 8.- Supersonic aerodynamic characteristics with transition fixed as determined by tests in the 8- by 7-foot test section (R/ft = 2,000,000 for arrow and delta models and 3,000,000 for the diamond model).

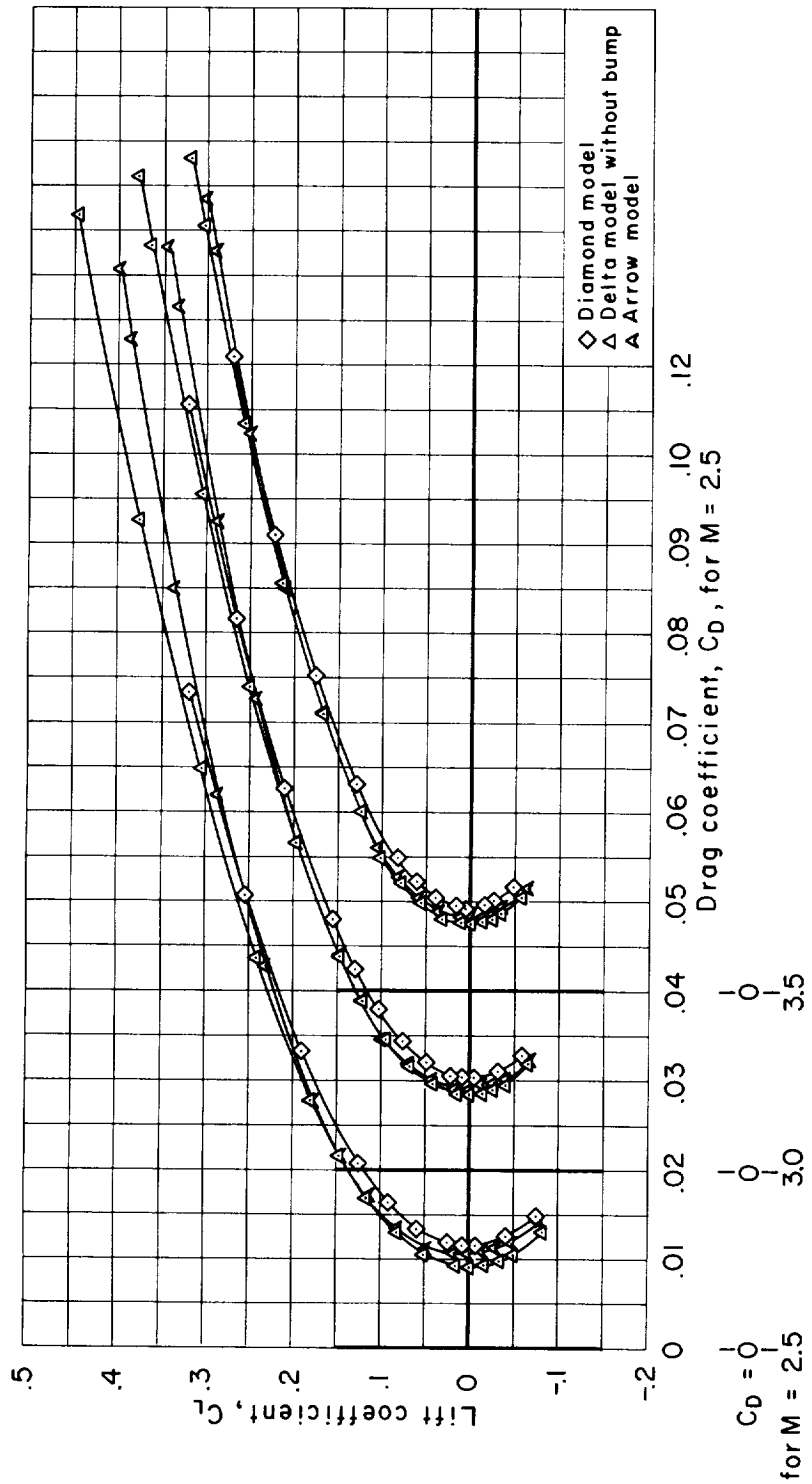

(b) C_L vs. C_D

Figure 8.- Continued.

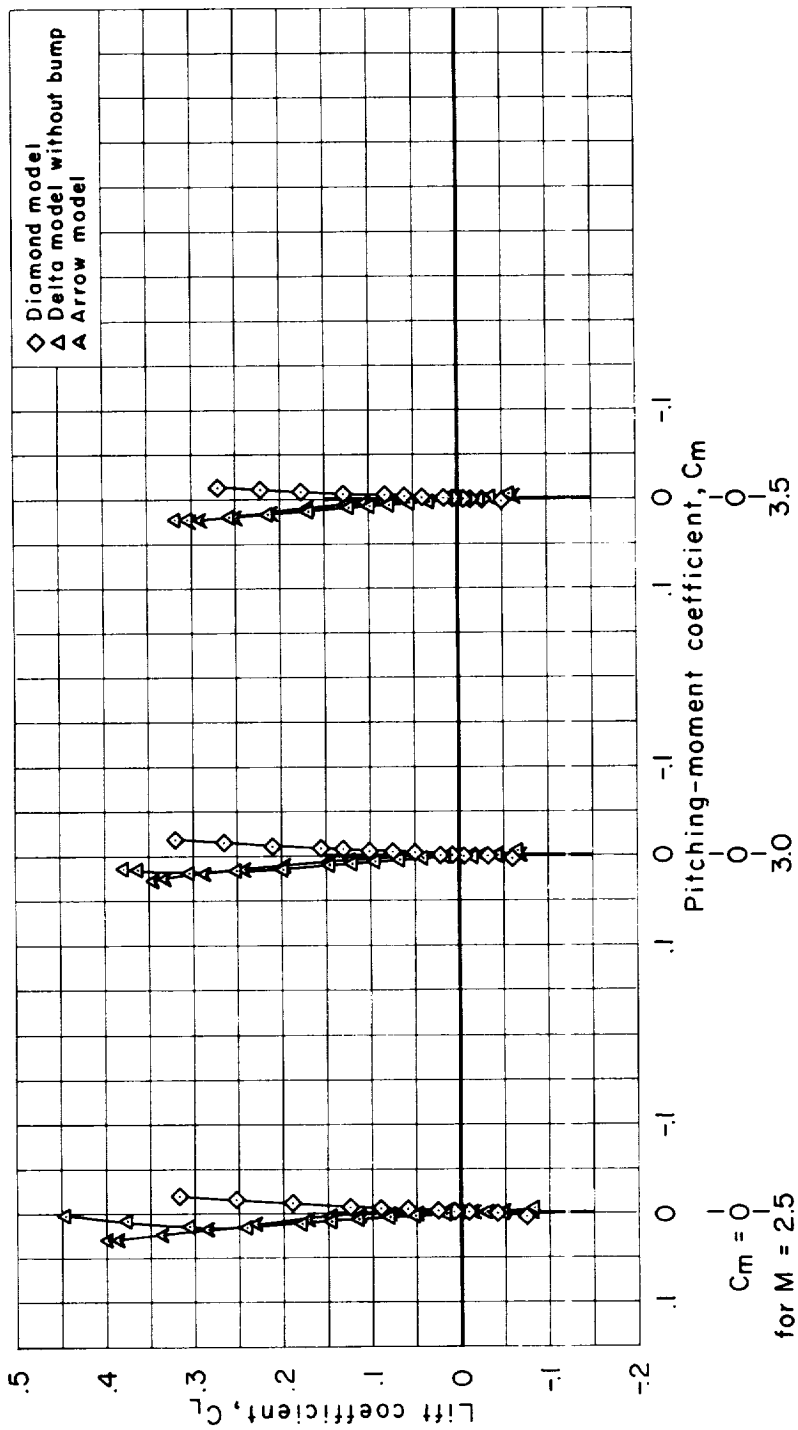

(c) C_L vs. C_m

Figure 8.- Continued.

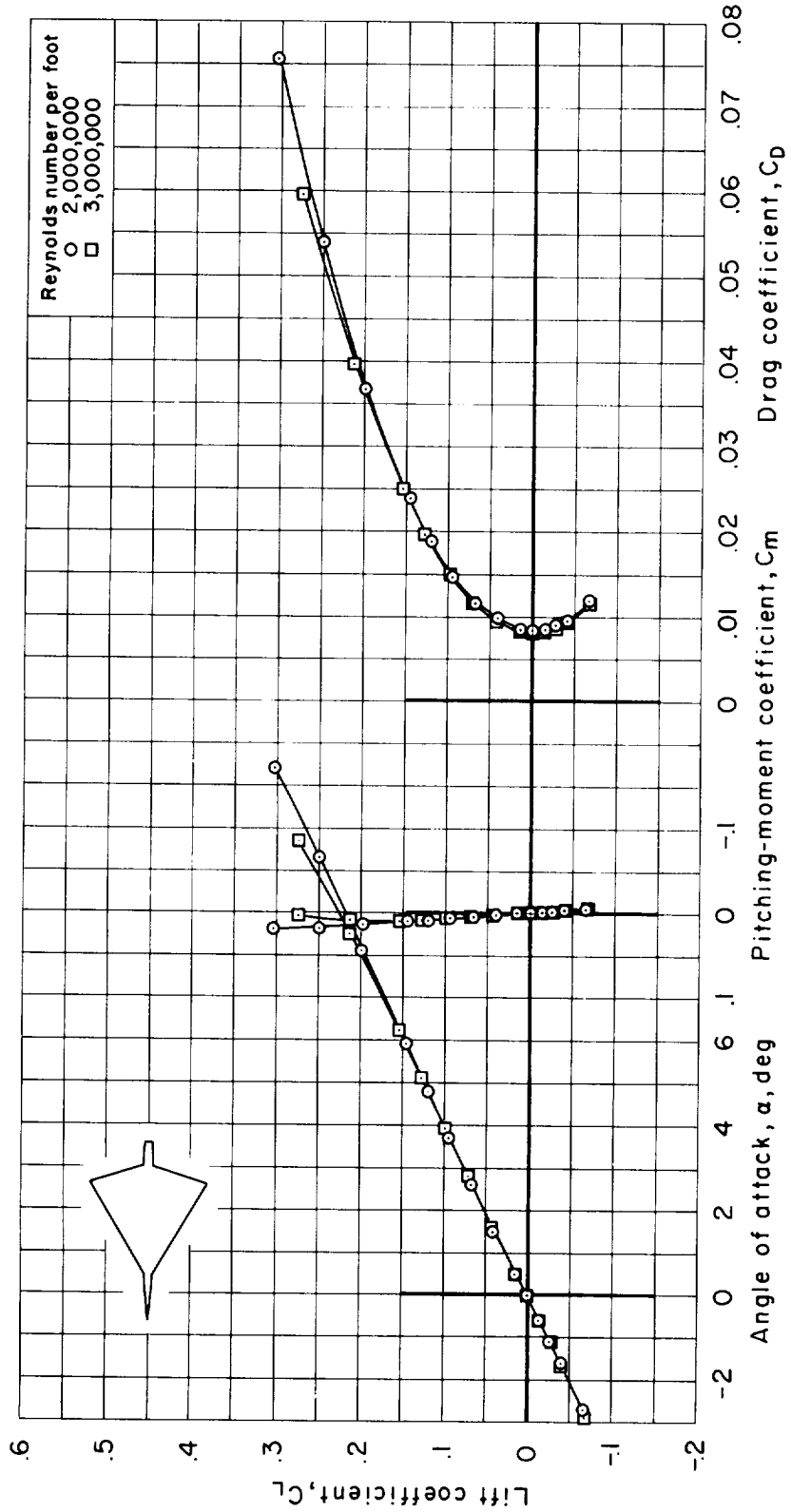

(d) Reynolds number effect at M = 3.00, delta model without bump.

Figure 8.- Continued.

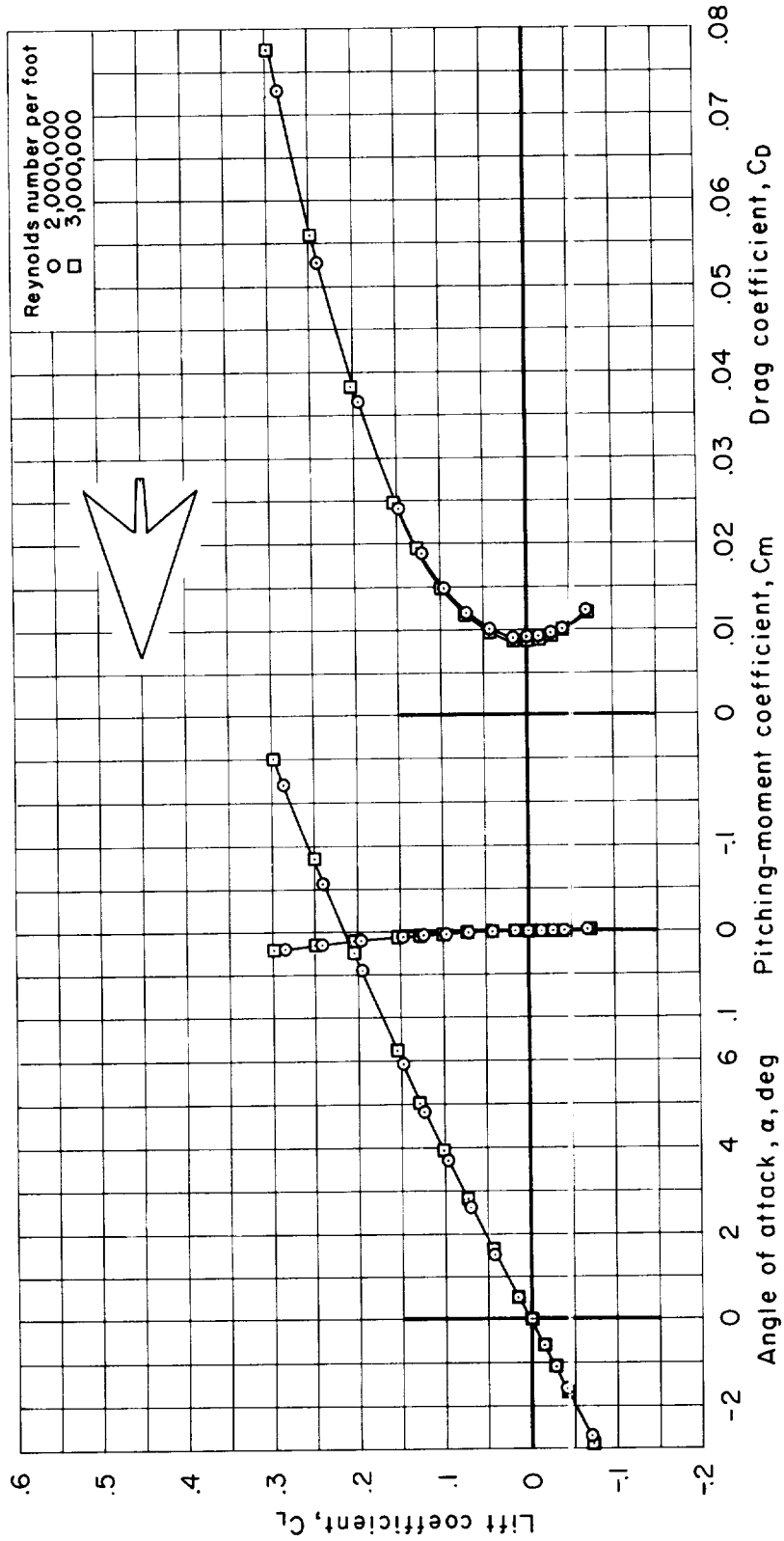

(e) Reynolds number effect at M = 3.00, arrow model.

Figure 8.- Concluded.

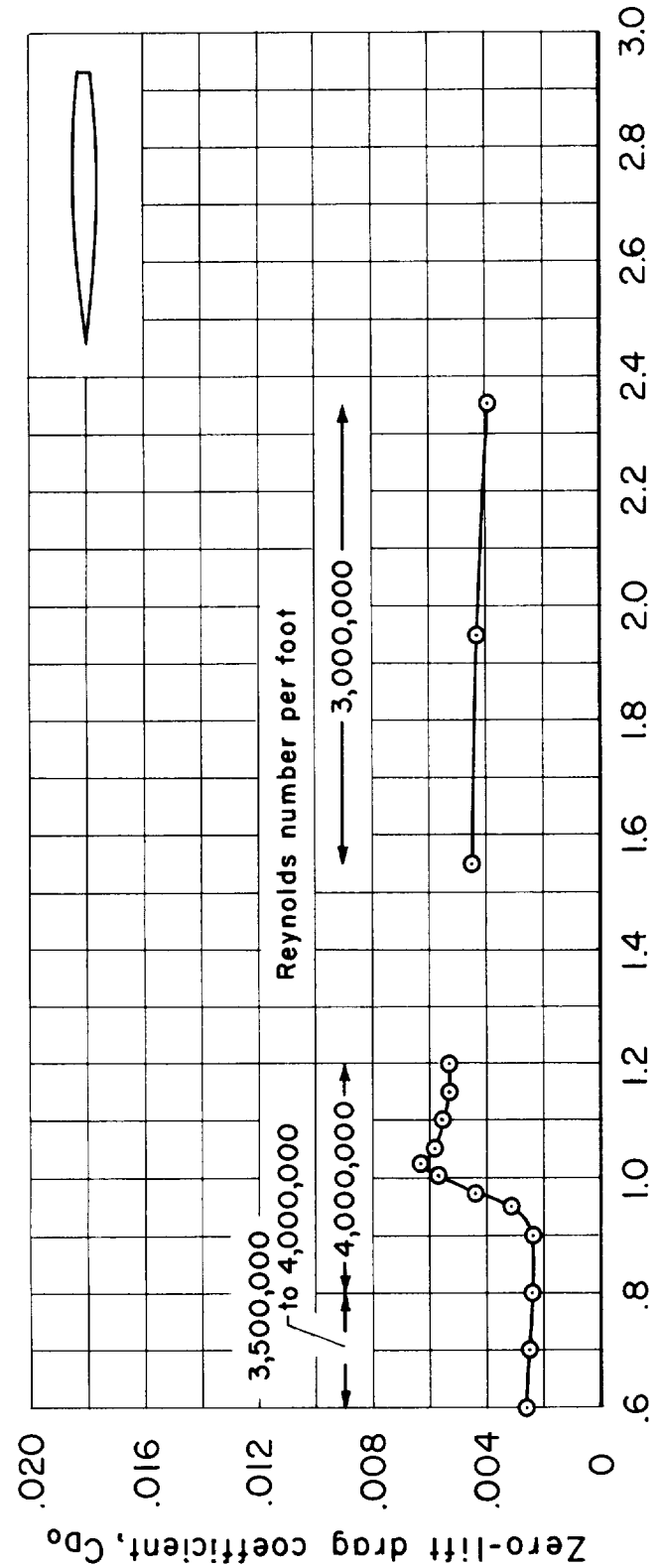

Figure 9.- Zero-lift drag coefficients for the M = 1.00 equivalent body with transition fixed as determined from tests in the 14-foot and 9- by 7-foot test sections (R/ft = 3,000,000 to 4,000,000).

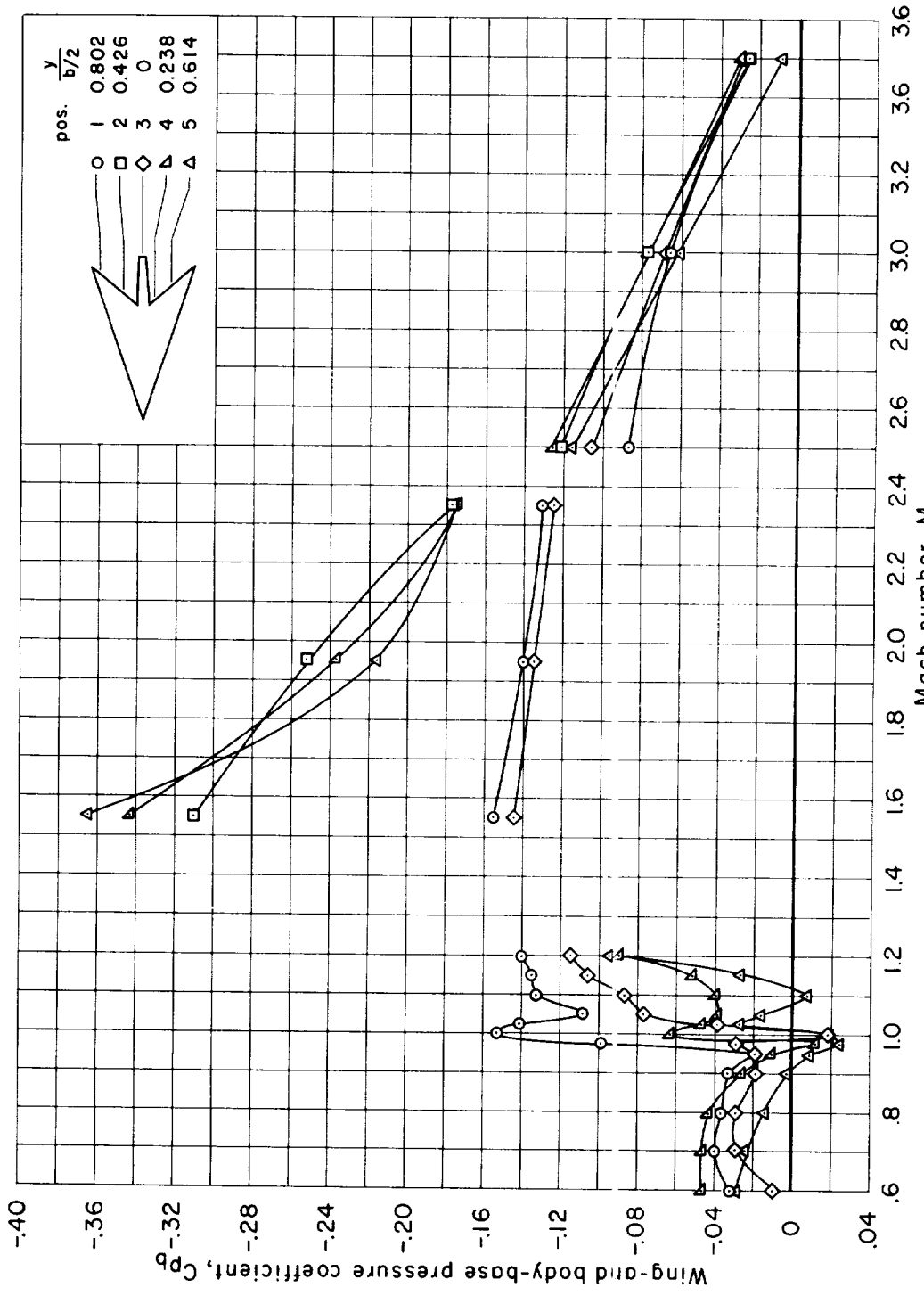

Figure 10.- Wing- and body-base pressure coefficients for the arrow model.

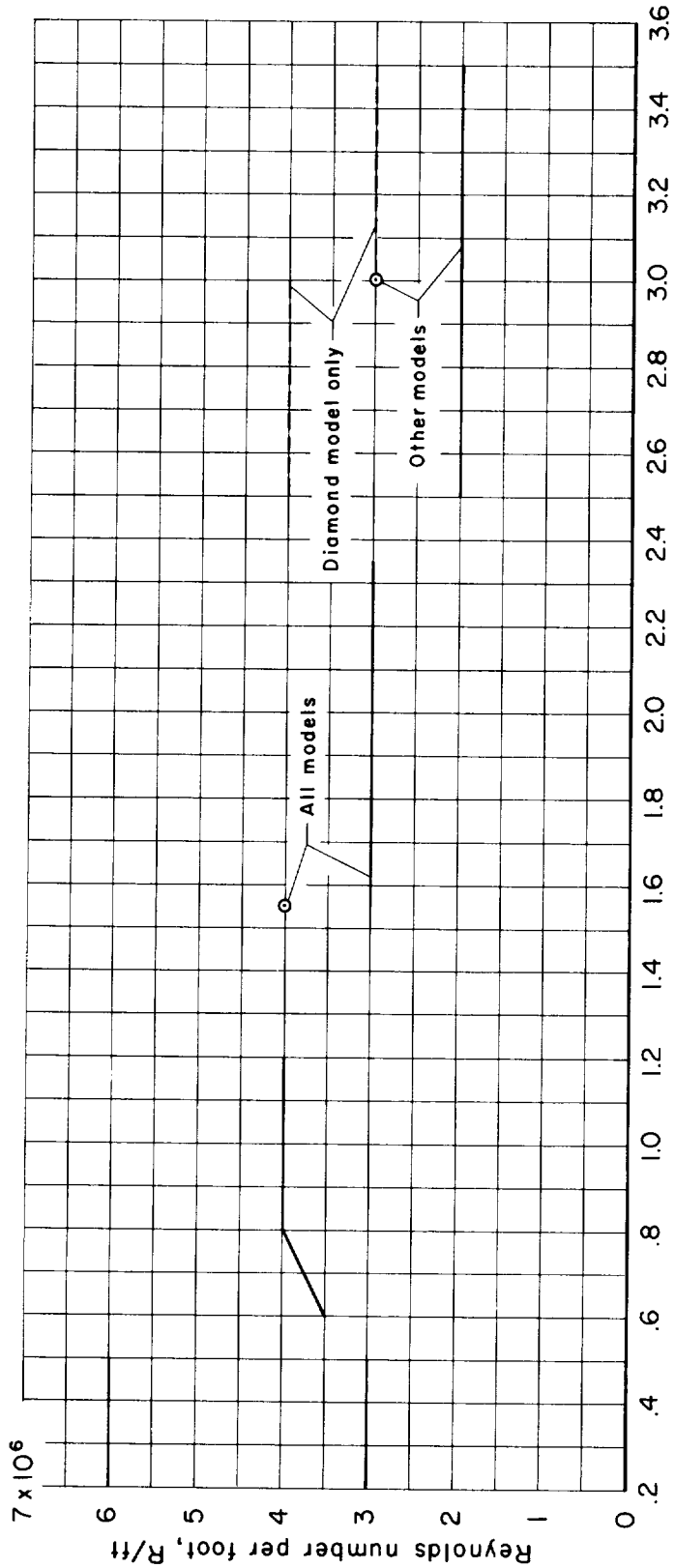

Figure 11.- Reynolds number per foot variation with Mach number for the models investigated.

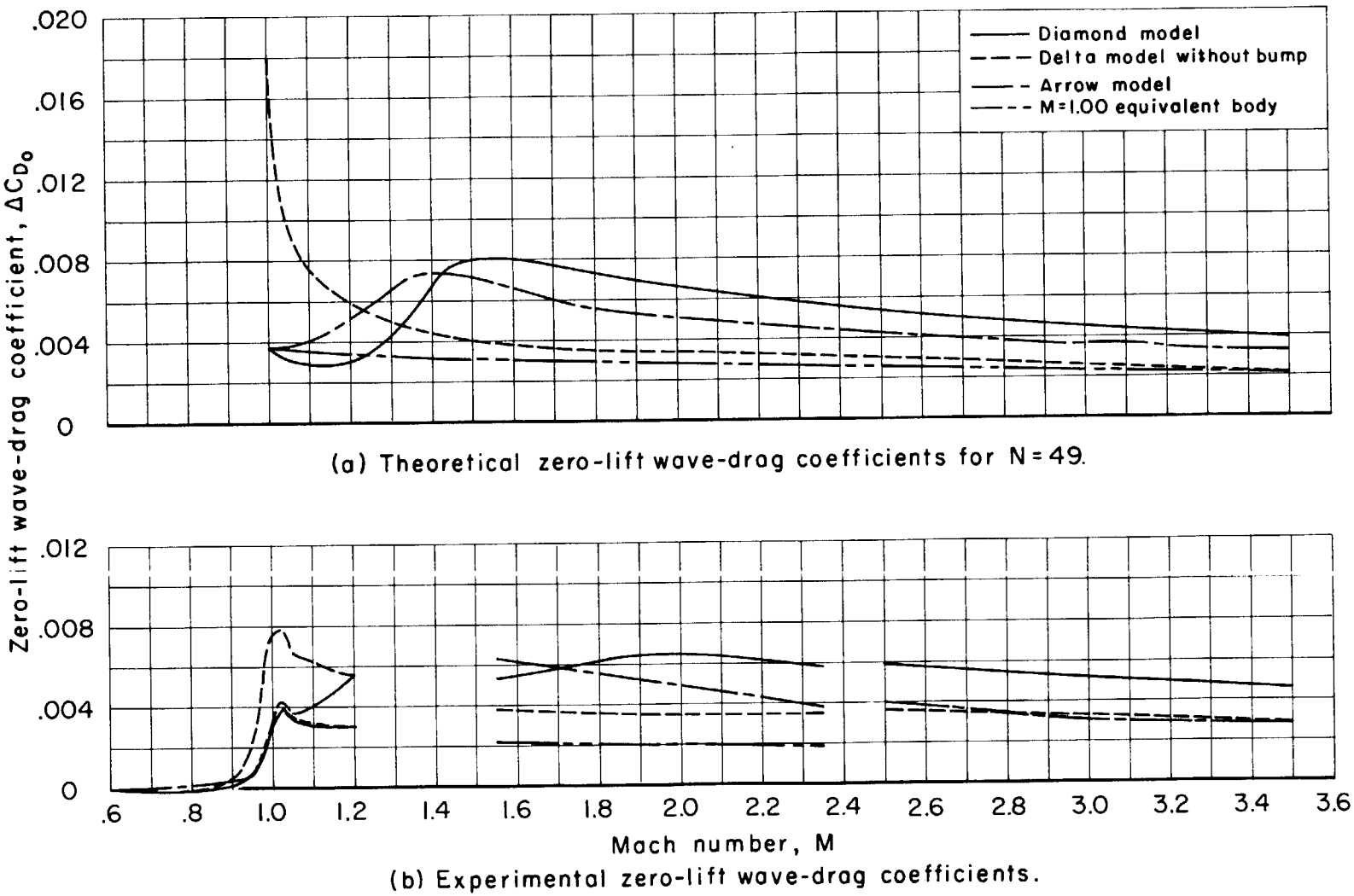

Figure 12.- Comparison of the zero-lift wave-drag coefficients for the three wing plan forms and the M = 1.00 equivalent body.

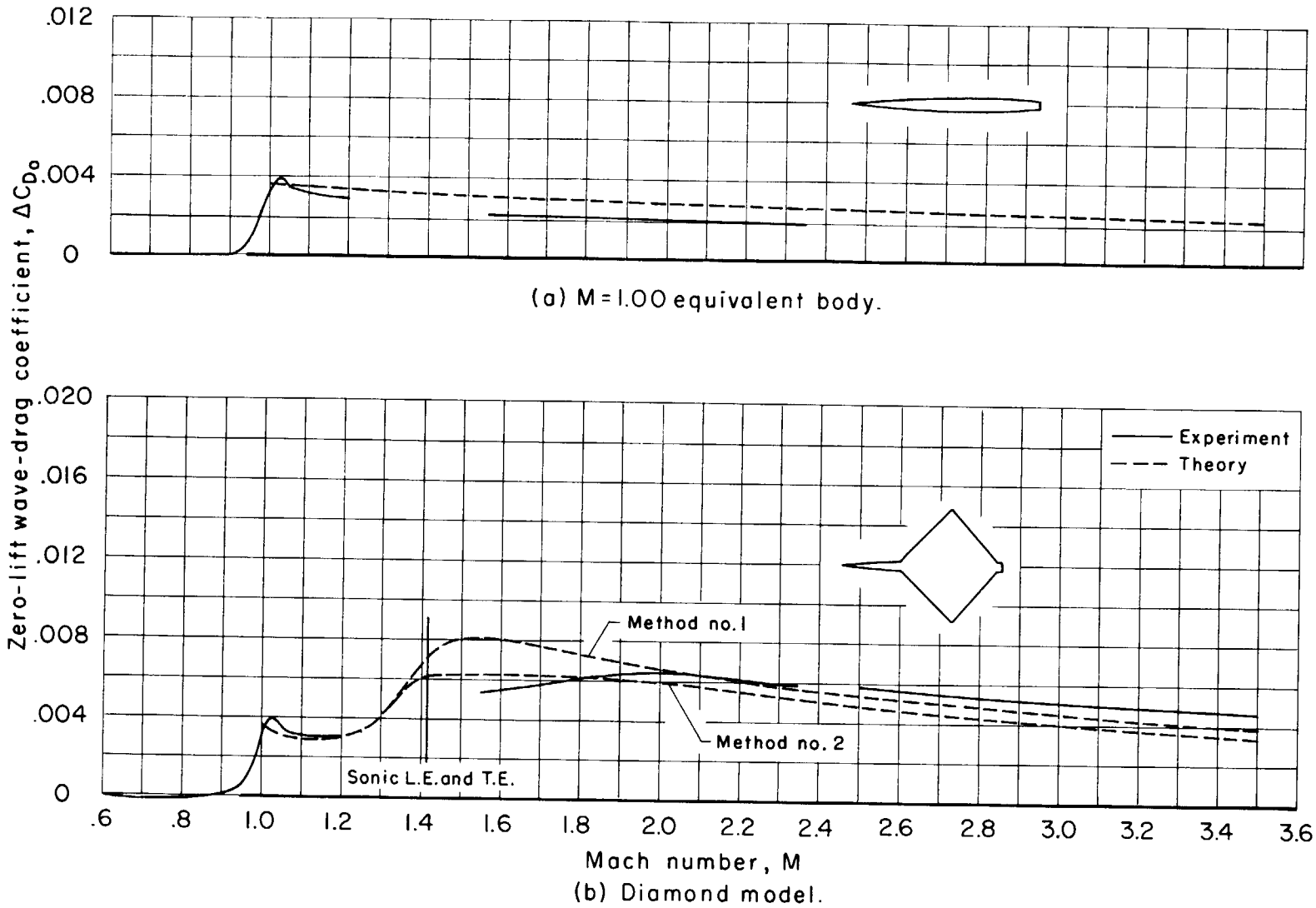

Figure 13.- Zero-lift wave-drag coefficients of the various models as determined by experiment and theory.

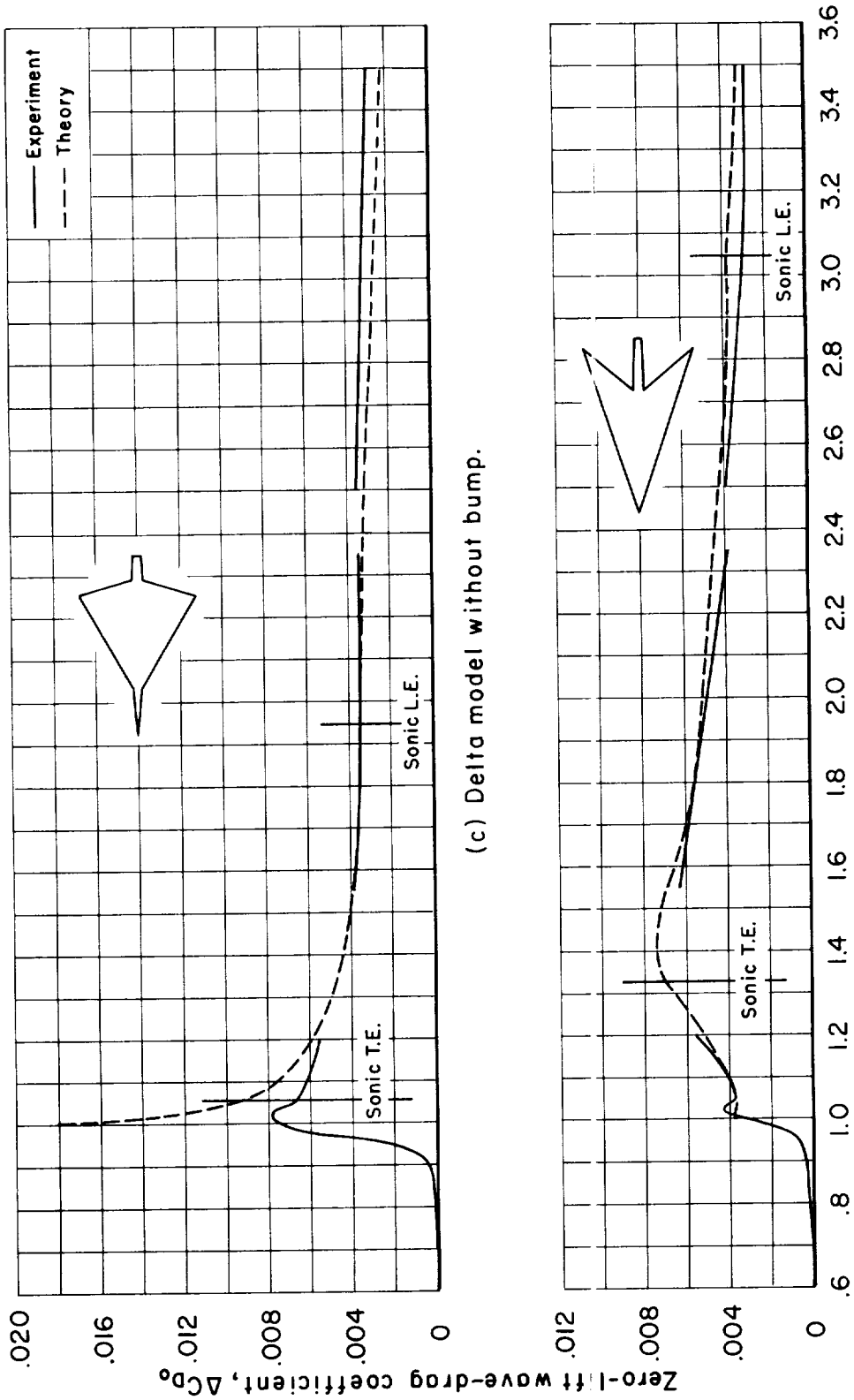

Figure 13.- Concluded.

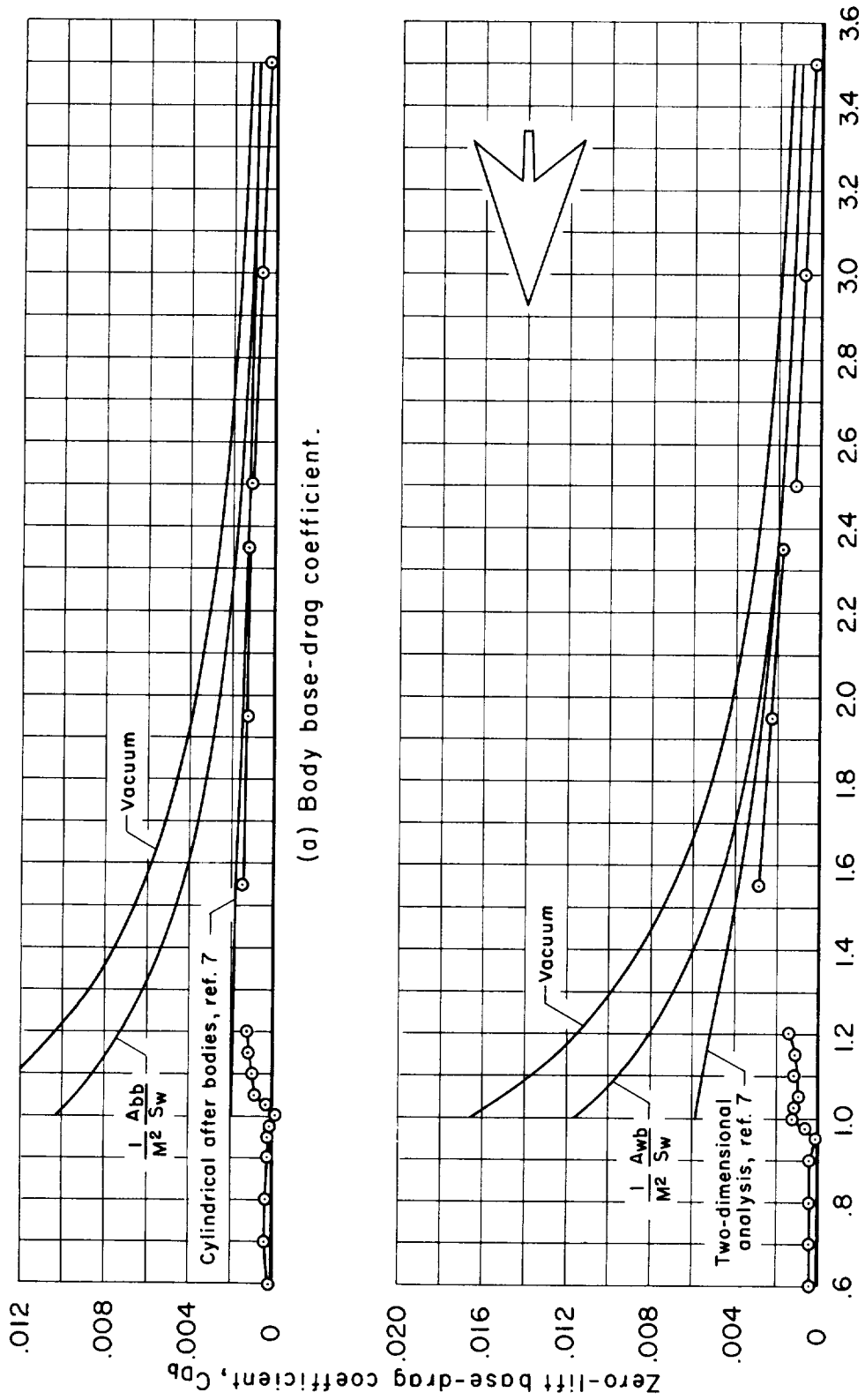

Figure 14.- Zero-lift base-drag coefficients for the wing and body bases of the arrow model as determined by experiment and empirical predictions.

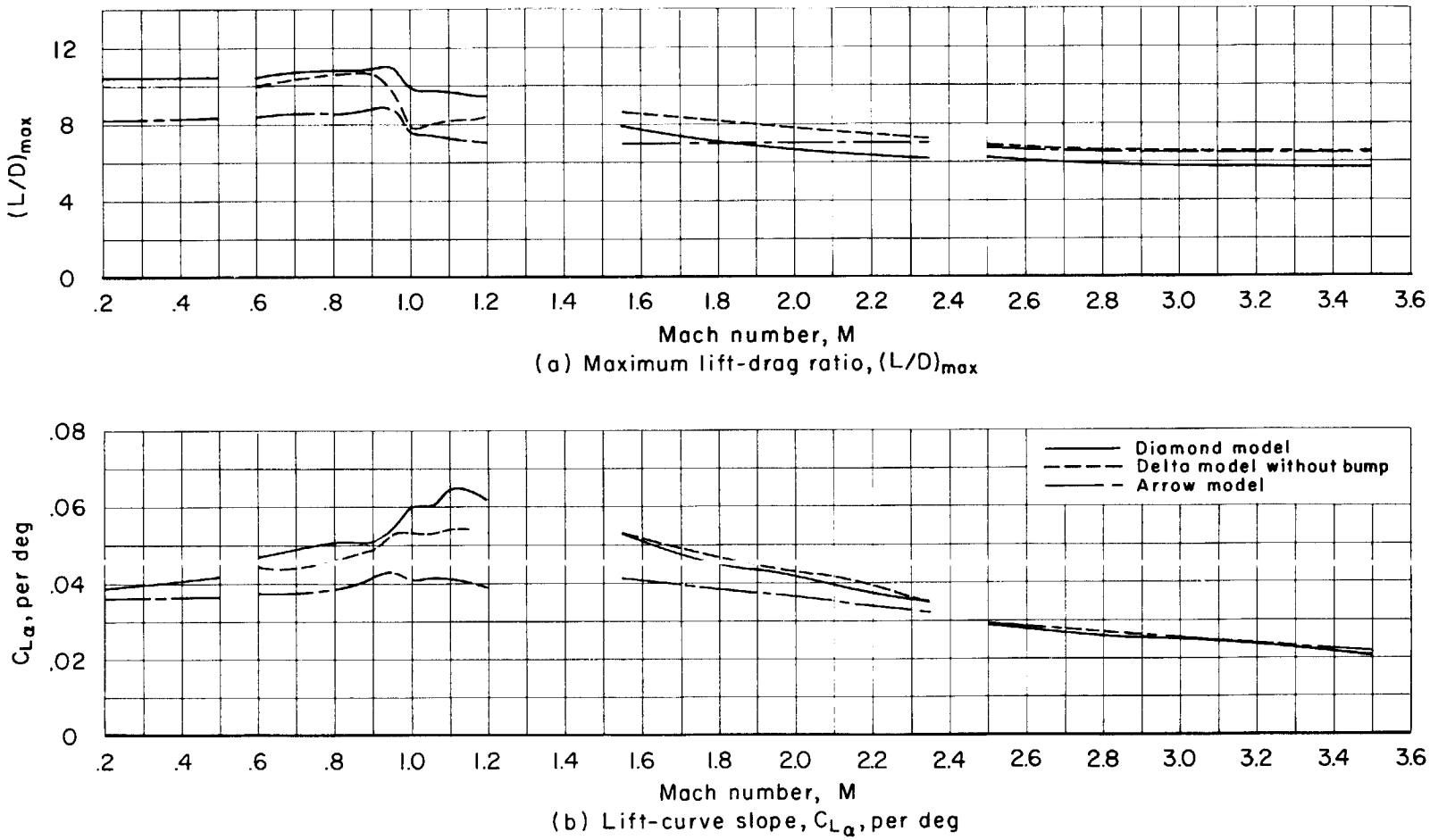

Figure 15.- Experimental aerodynamic trends with Mach number for the models of different plan form (transition fixed except at M = 0.20 to M = 0.50).

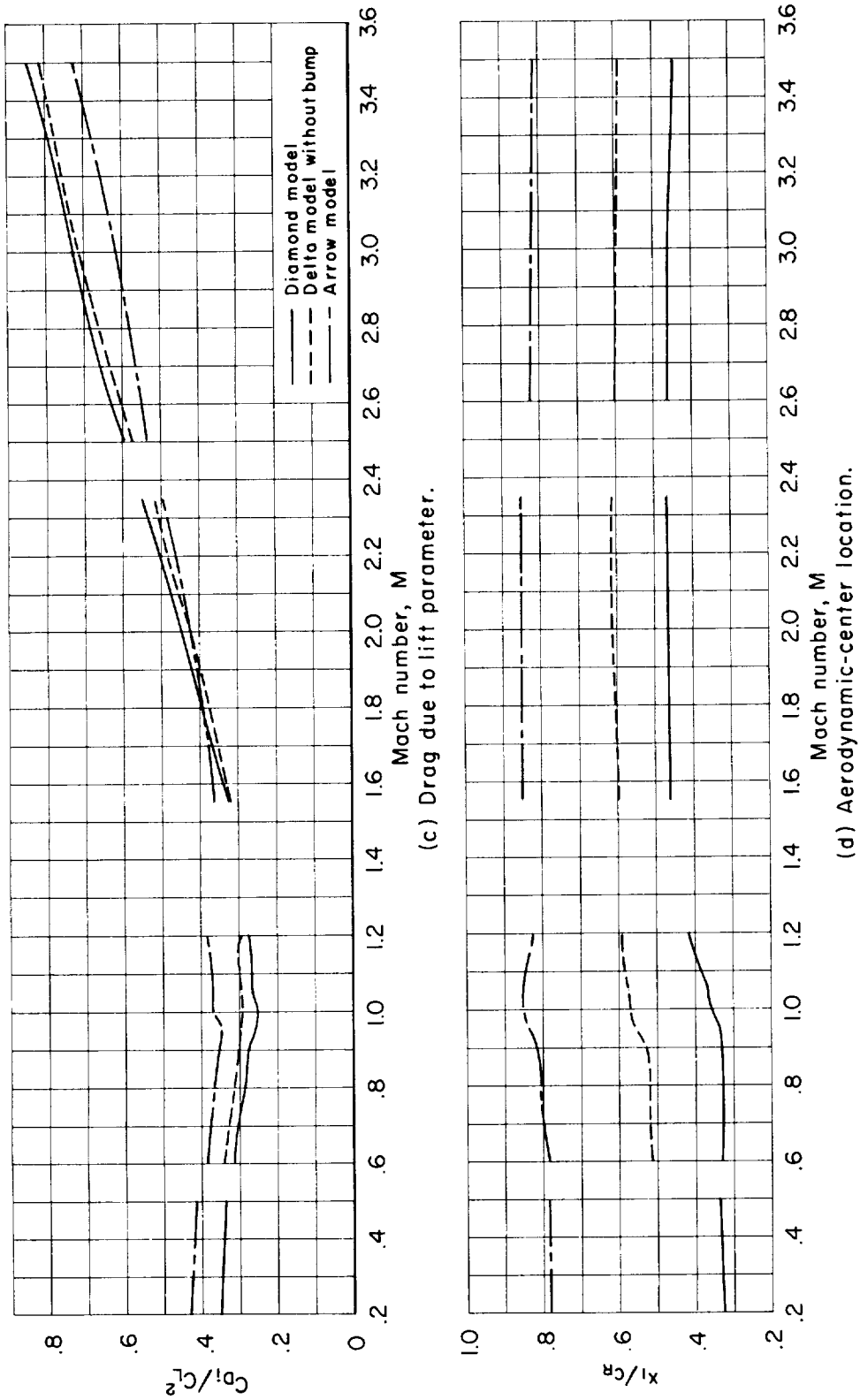

Figure 15.- Concluded.

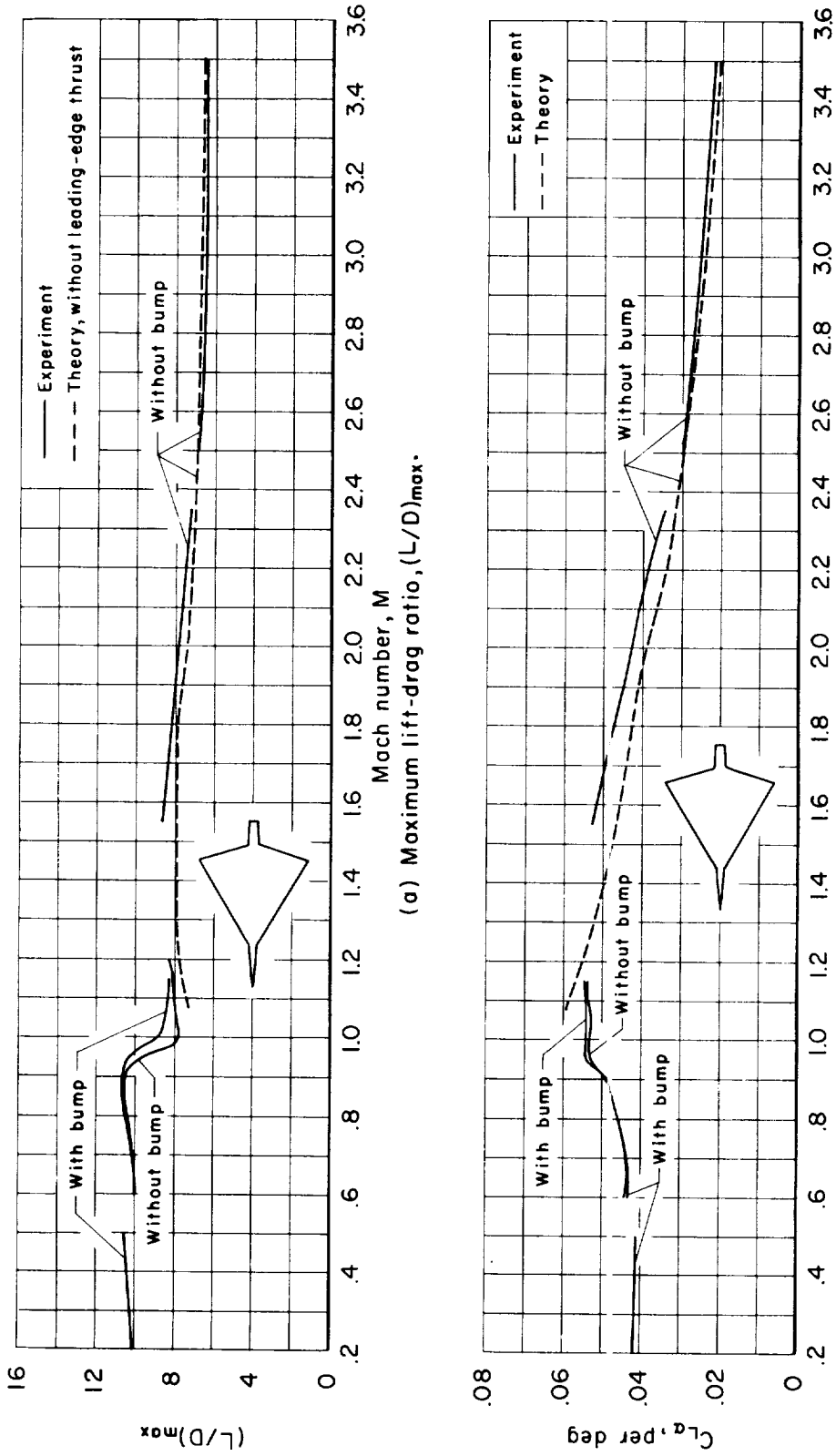

Figure 16.- Aerodynamic trends with Mach number for the delta models as indicated by experiment and theory (transition fixed except at M = 0.20 to 0.50).

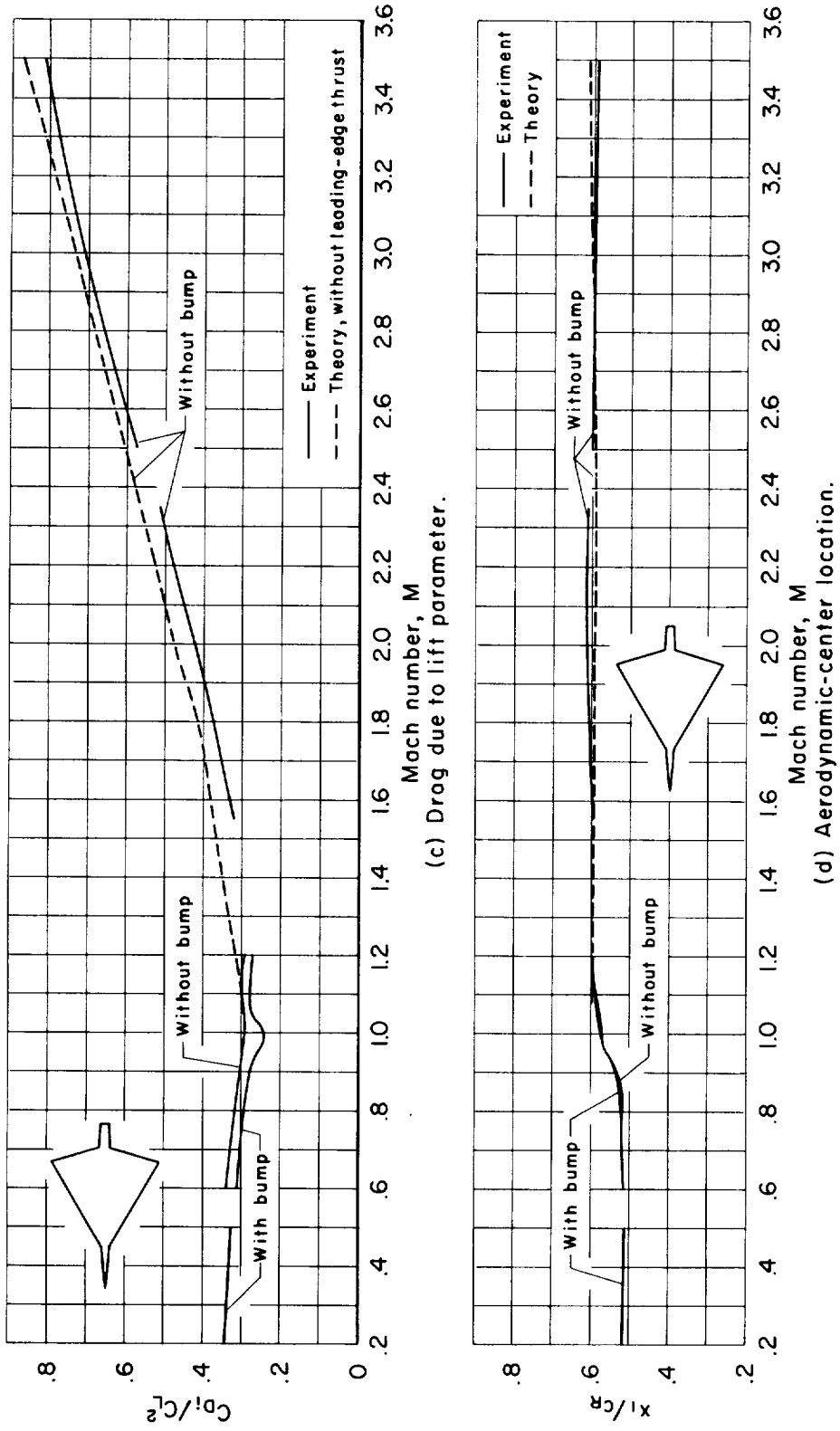

Figure 16.- Concluded.

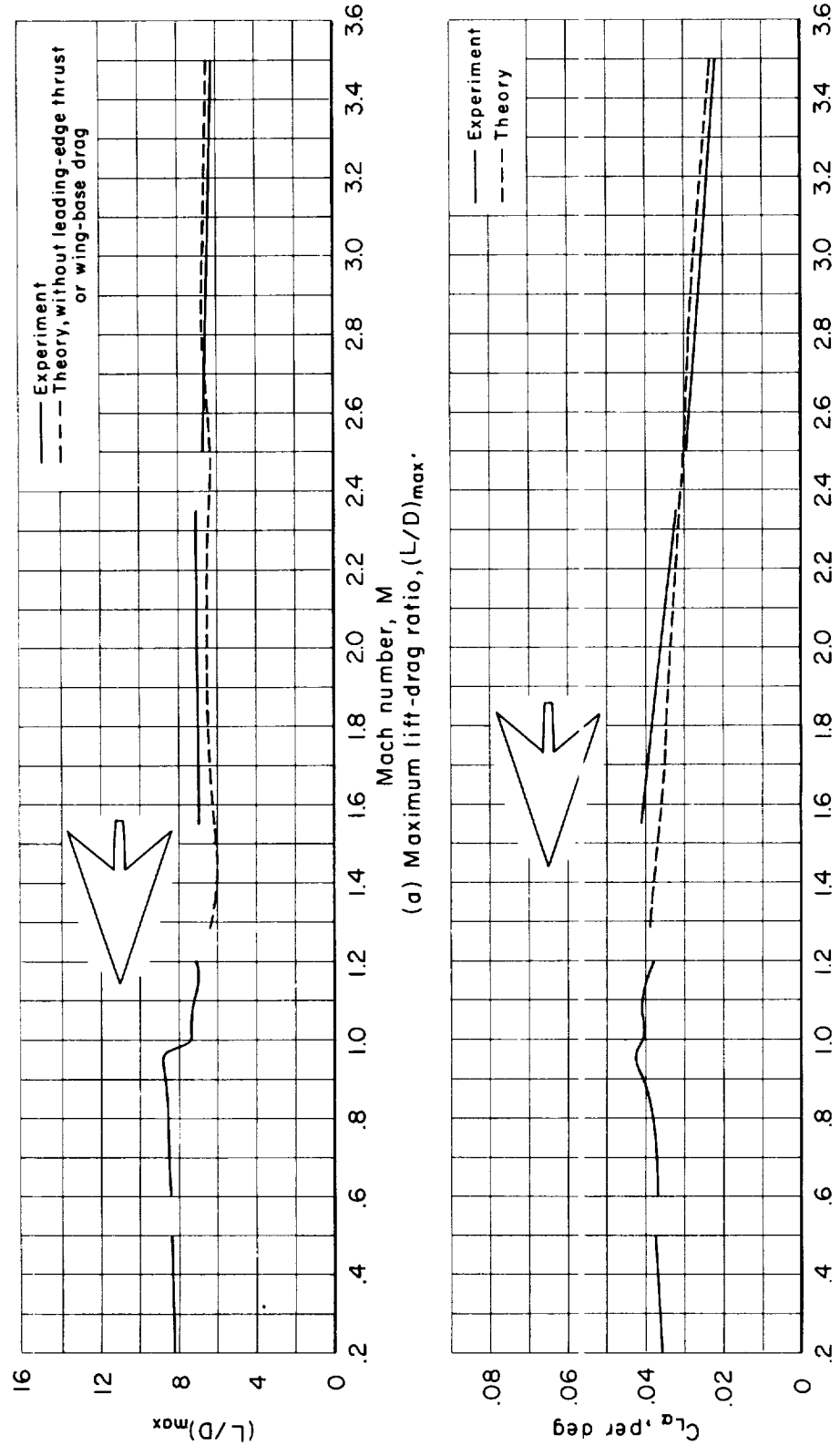

Figure 17.- Aerodynamic trends with Mach number for the arrow model as indicated by experiment and theory (transition fixed except at M = 0.20 to 0.50).

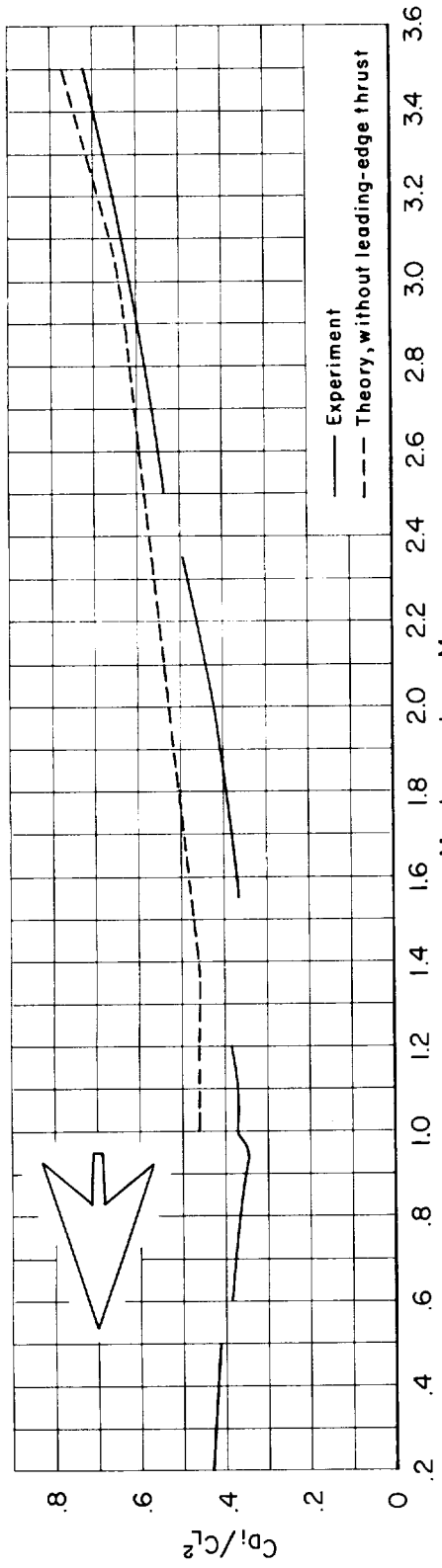

(c) Drag due to lift parameter.

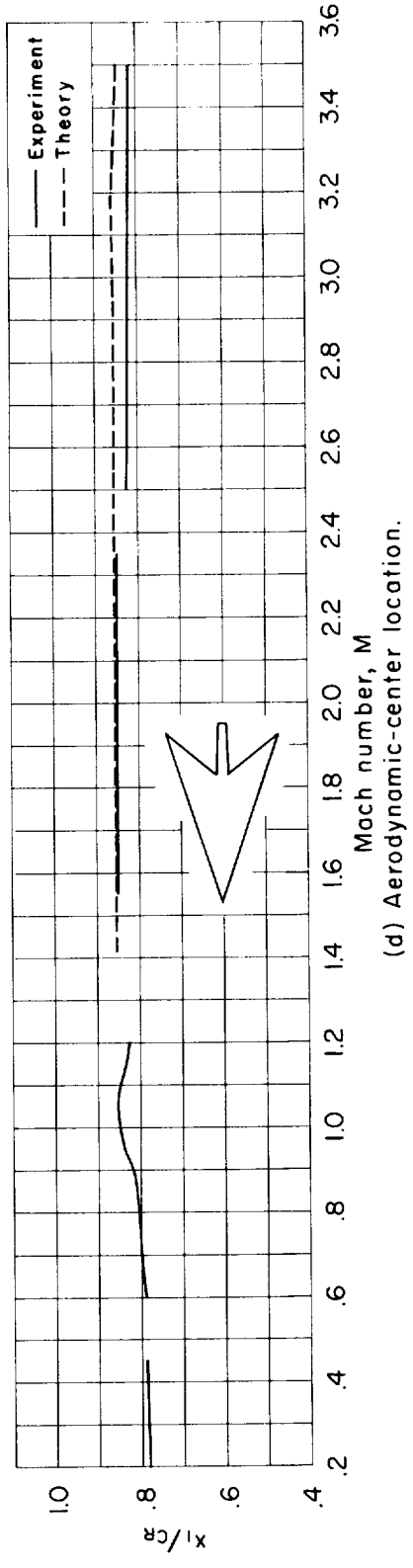

(d) Aerodynamic-center location.

Figure 17.- Concluded.

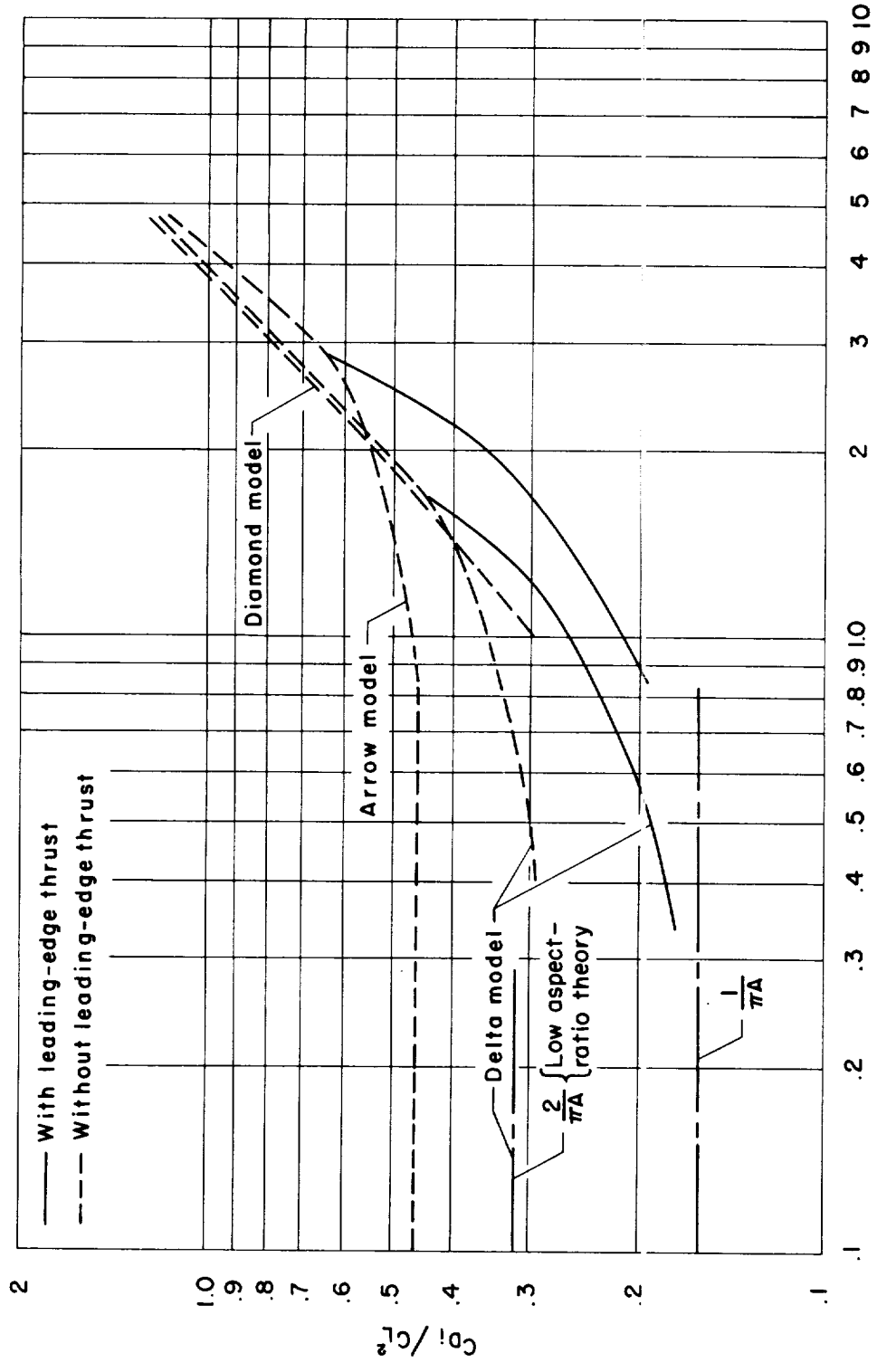

Figure 18.- Theoretical values of drag due to lift parameter for flat-plate wings of different plan form with and without leading-edge thrust.

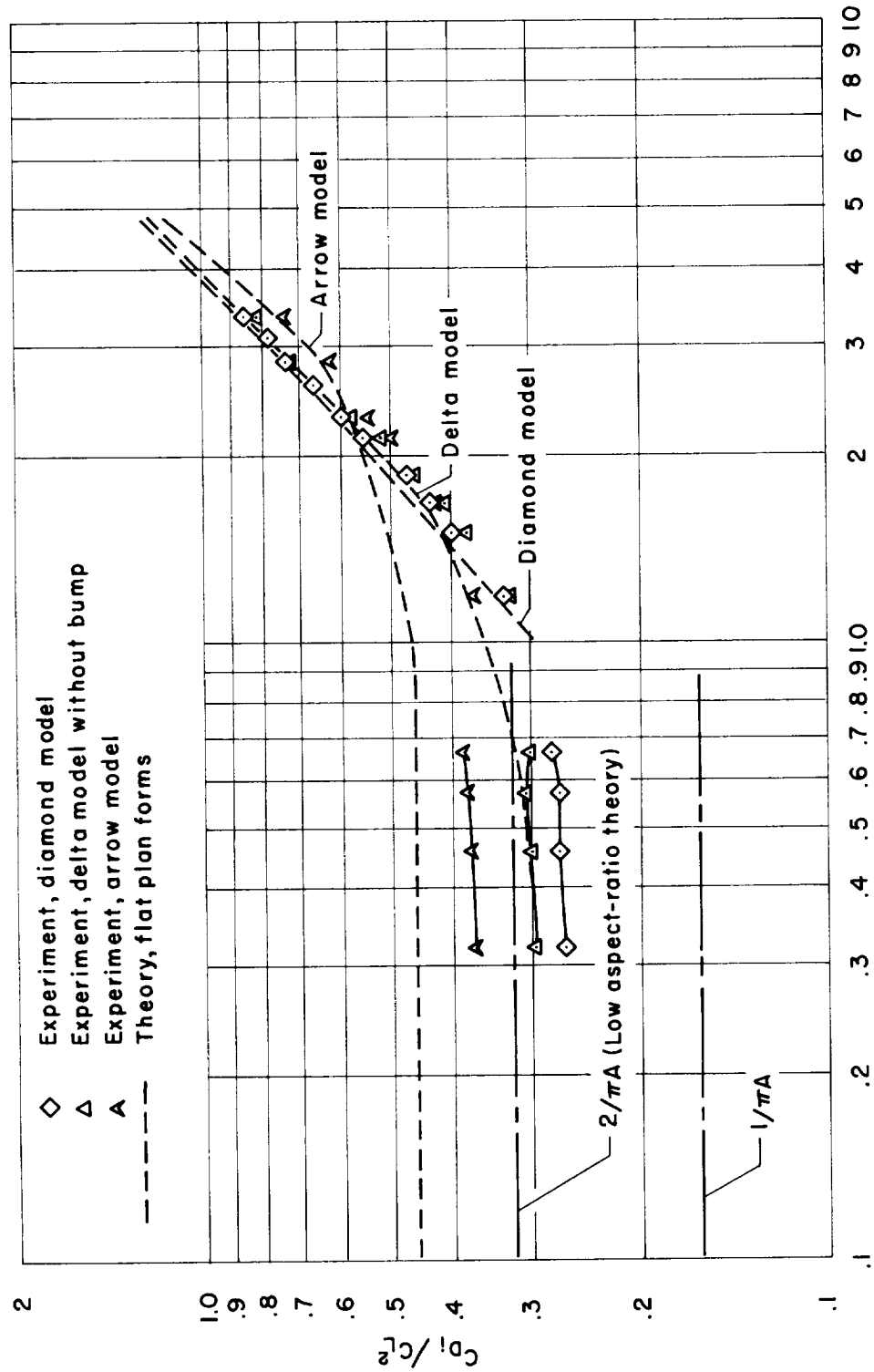

Figure 19.- Experimental values of drag due to lift parameter at supersonic speeds and theory without leading-edge thrust.

$$S = \frac{l}{4} \sum_{2}^{N} A_n \left[\frac{\sin(n-1)\phi}{n-1} - \frac{\sin(n+1)\phi}{n+1} \right] ; \cos\phi = \left(\frac{2x}{l} - 1 \right)$$

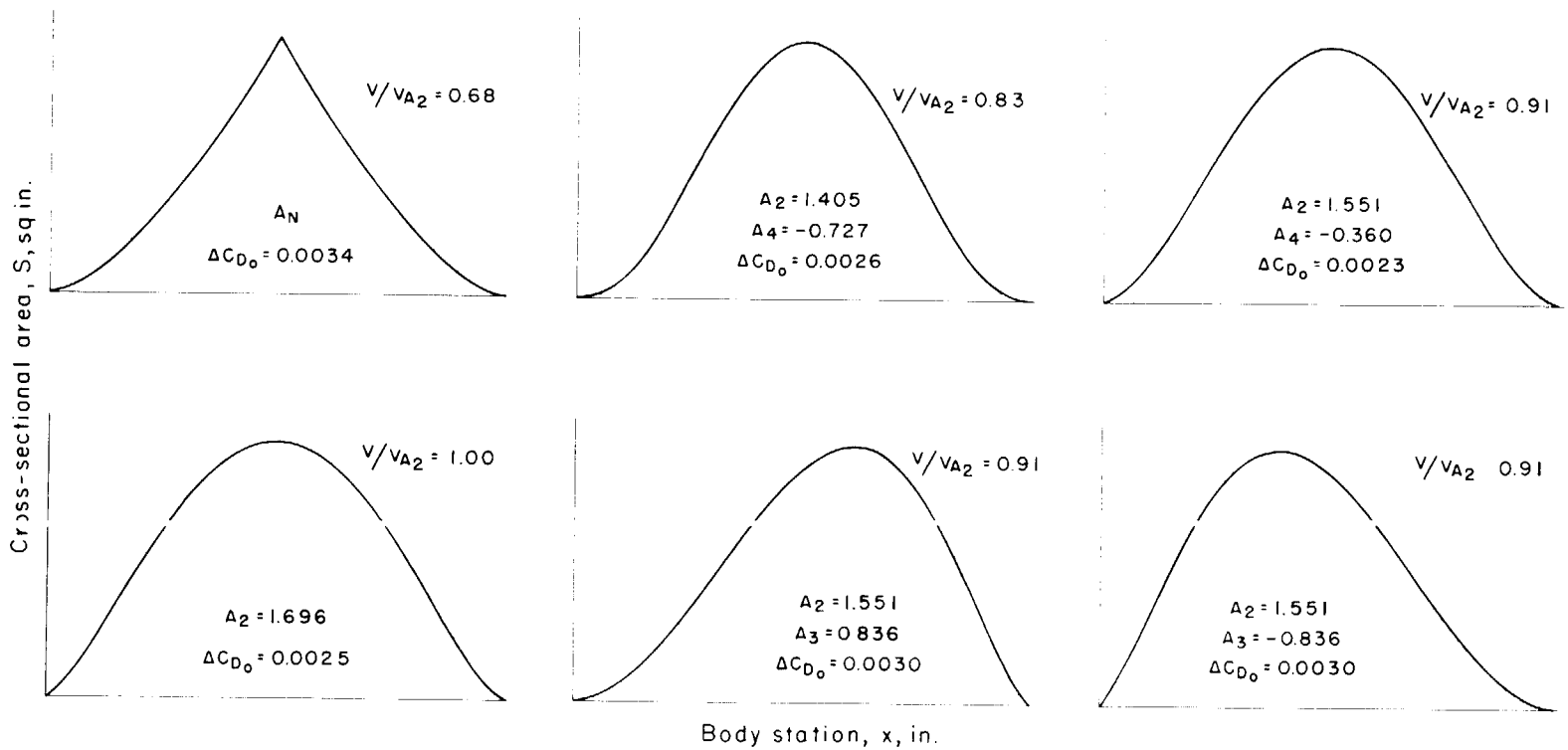

Figure 20.- Area curves considered in the selection of the design area distribution; the corresponding theoretical zero-lift wave-drag coefficients (ΔC_{D_o}) are for M = 1.00 and N = 25.

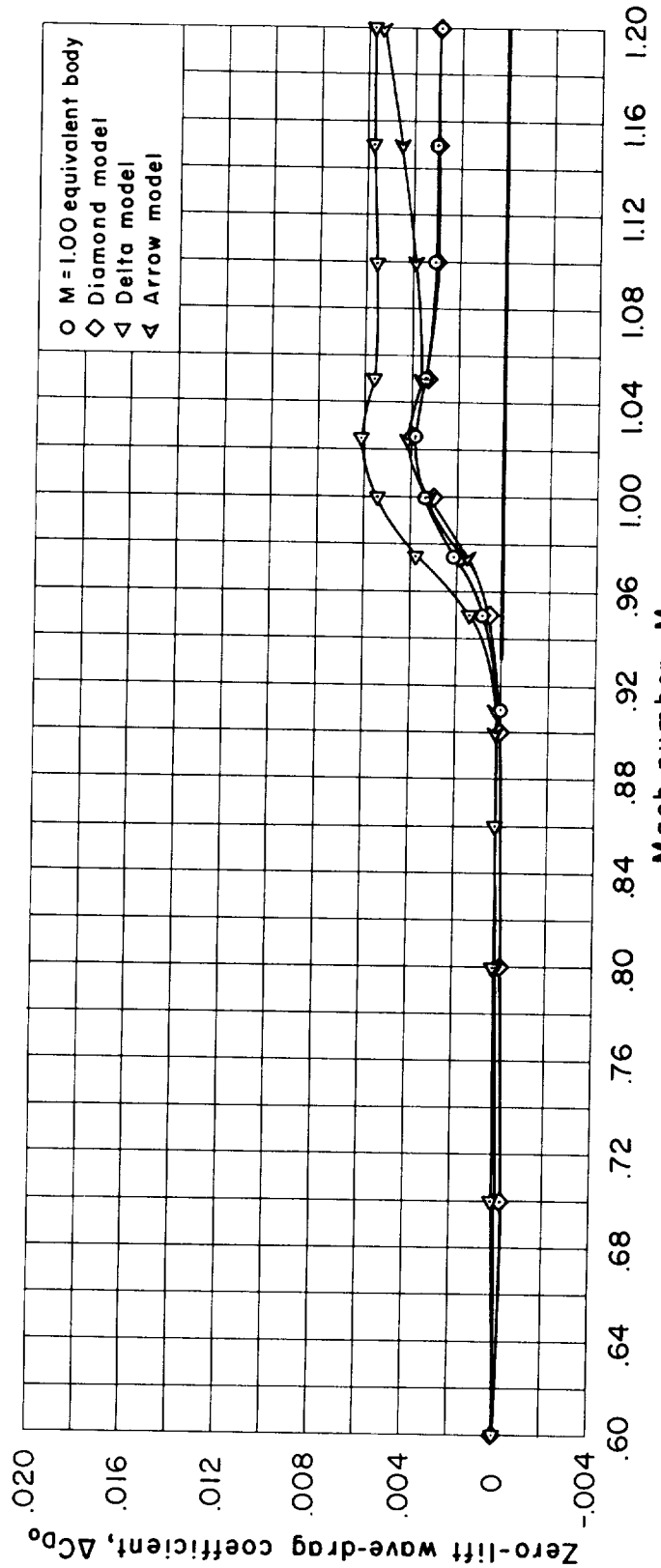

Figure 21.- Transonic zero-lift wave-drag coefficients for the three models of different plan form and for the M = 1.00 equivalent body.

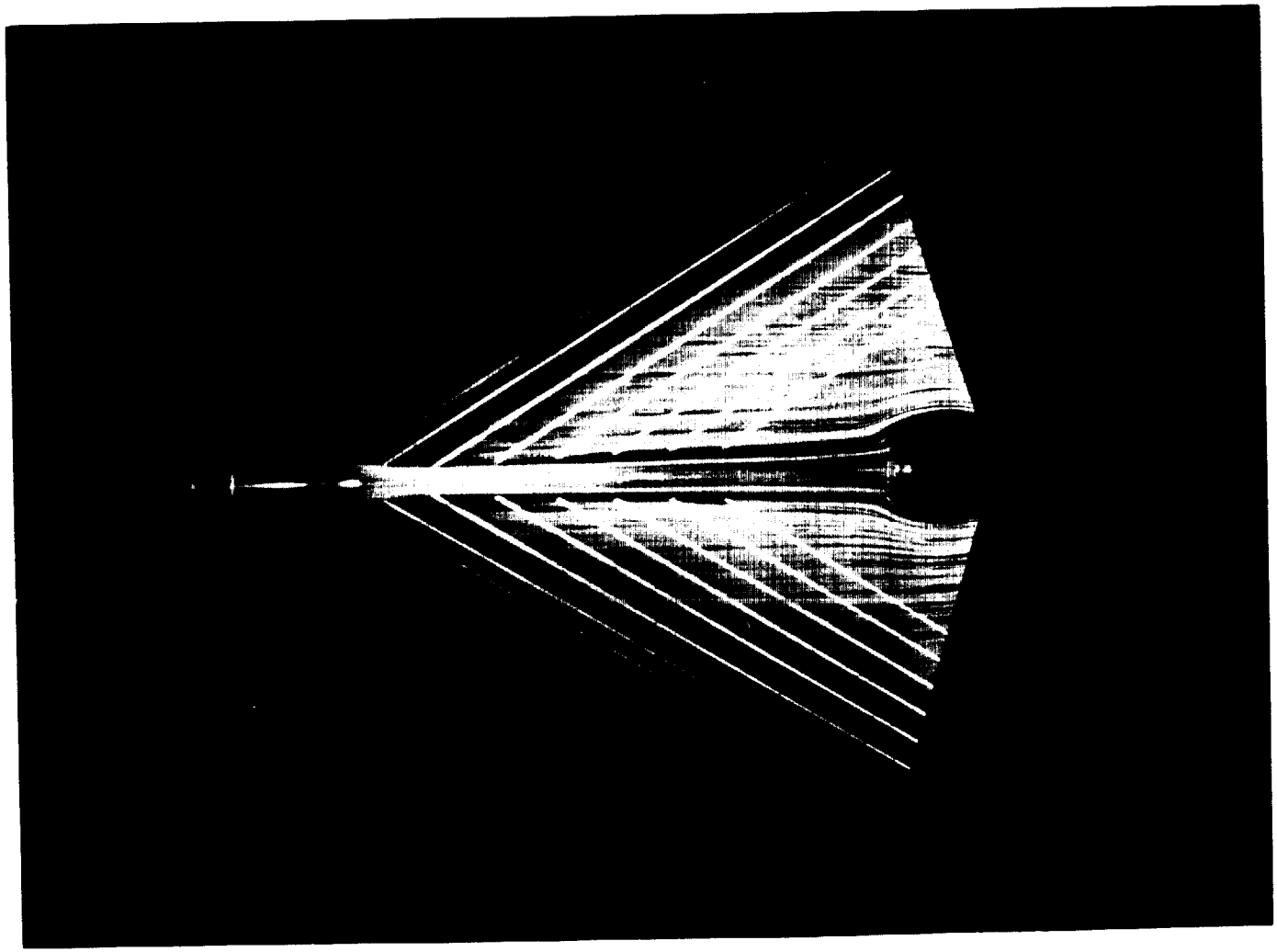

A-26528

Figure 22.- Thickened boundary layer near the rear bump of the body of the delta model as indicated by a fluorescent-oil film ($M = 0.60$, $\alpha = 0^{\circ}$).

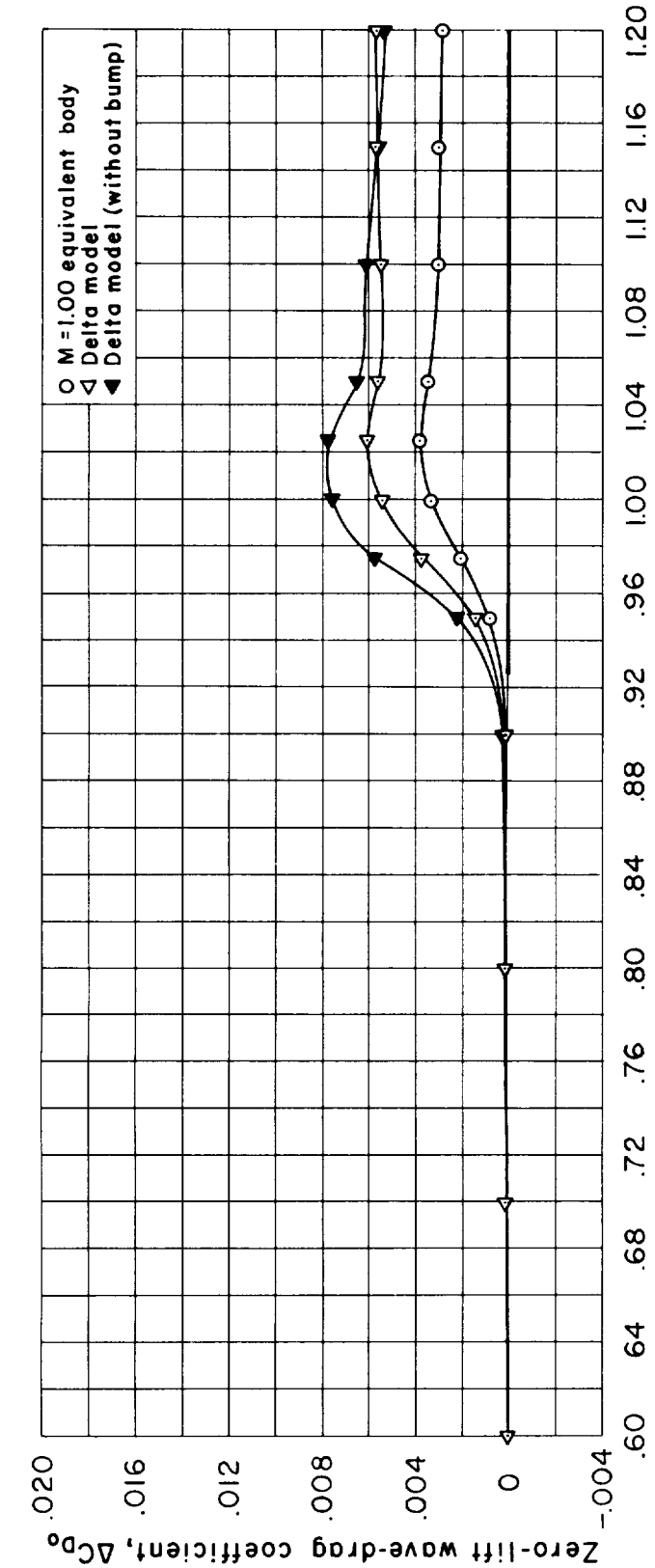

Figure 23.- Transonic zero-lift wave-drag coefficients of the delta model with and without the bump at the rear of the body.

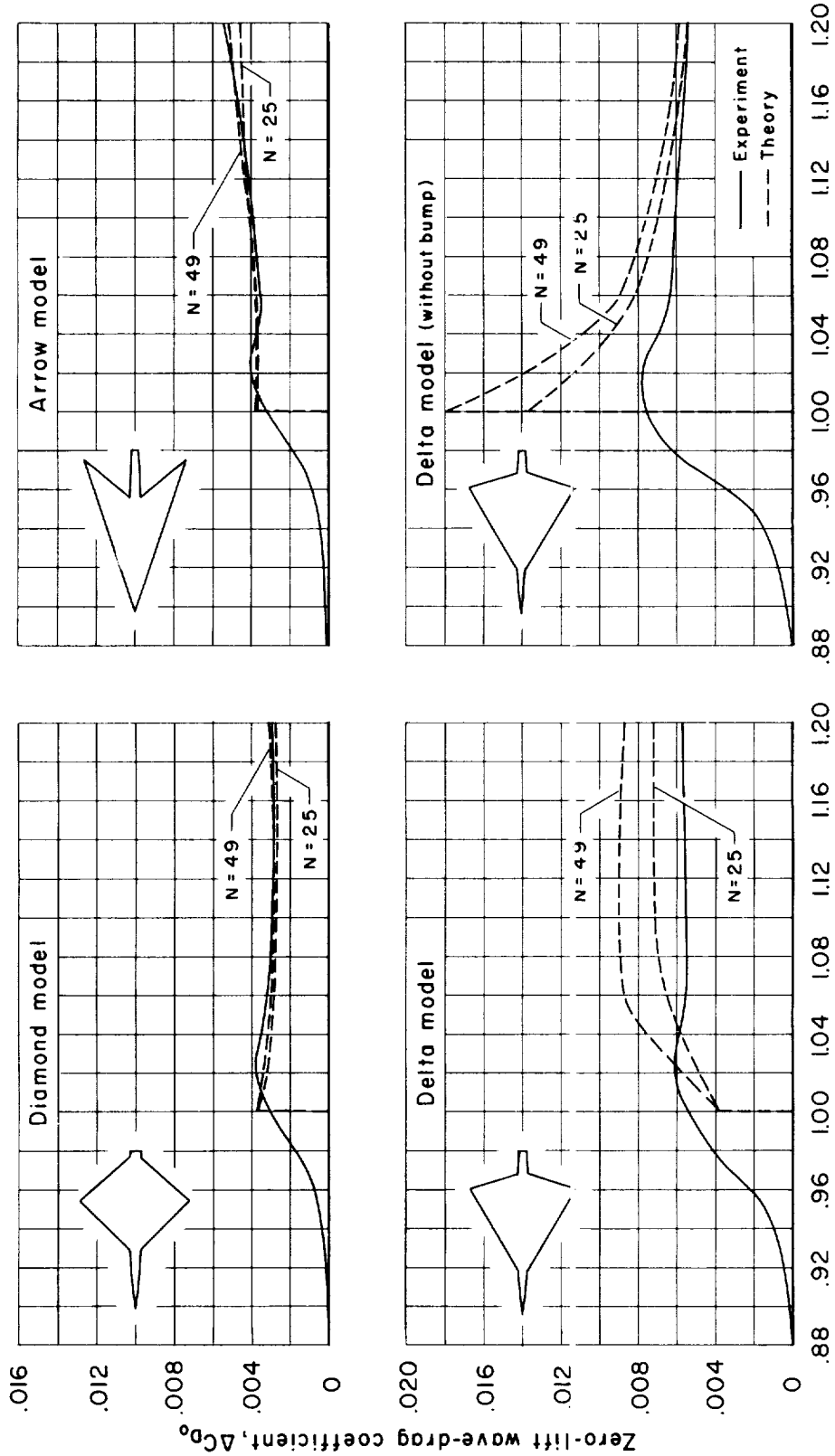

Figure 24.- Transonic zero-lift wave-drag coefficients of the various winged models as determined by experiment and theory.

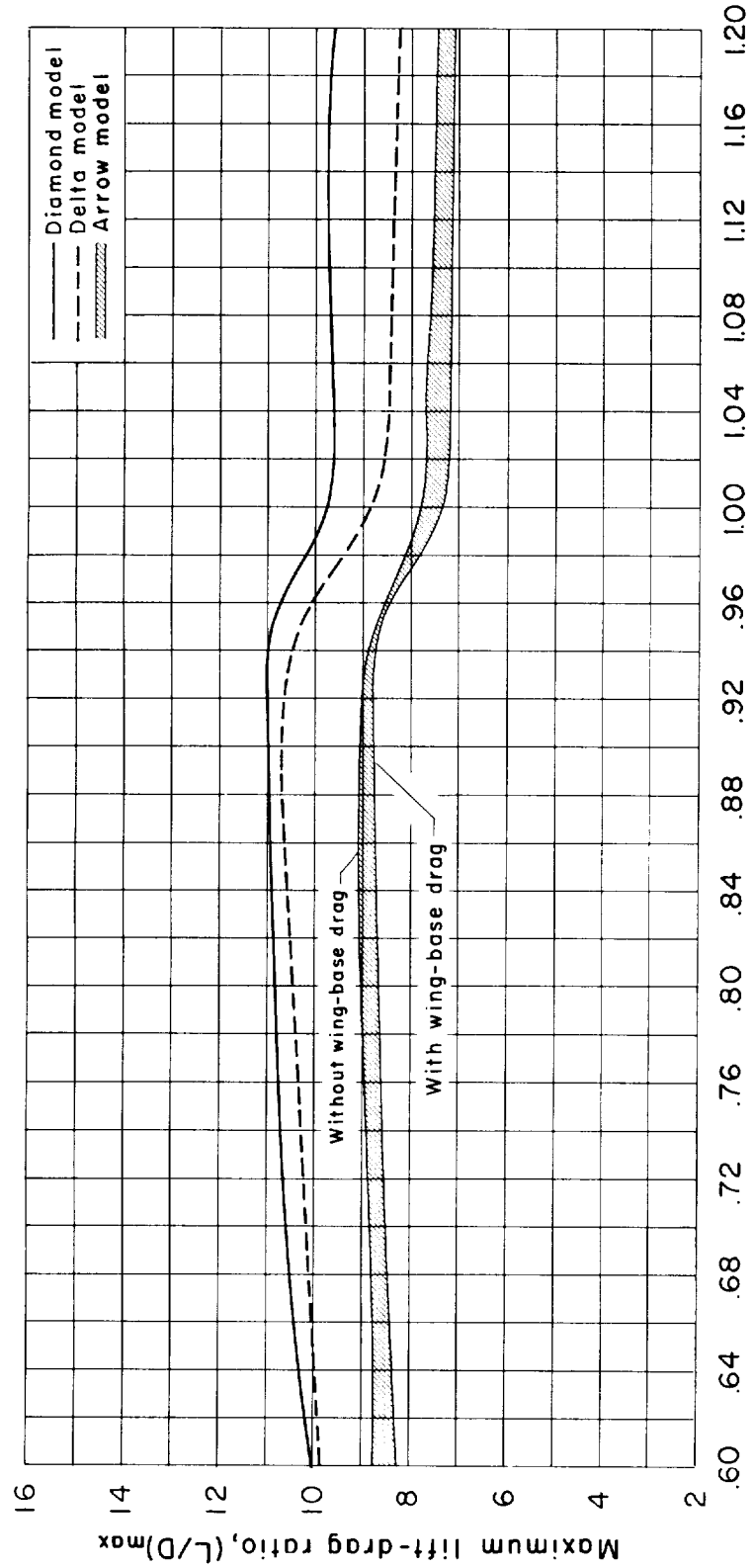

Figure 25.- Transonic maximum lift-drag ratios for the three models of different plan form.

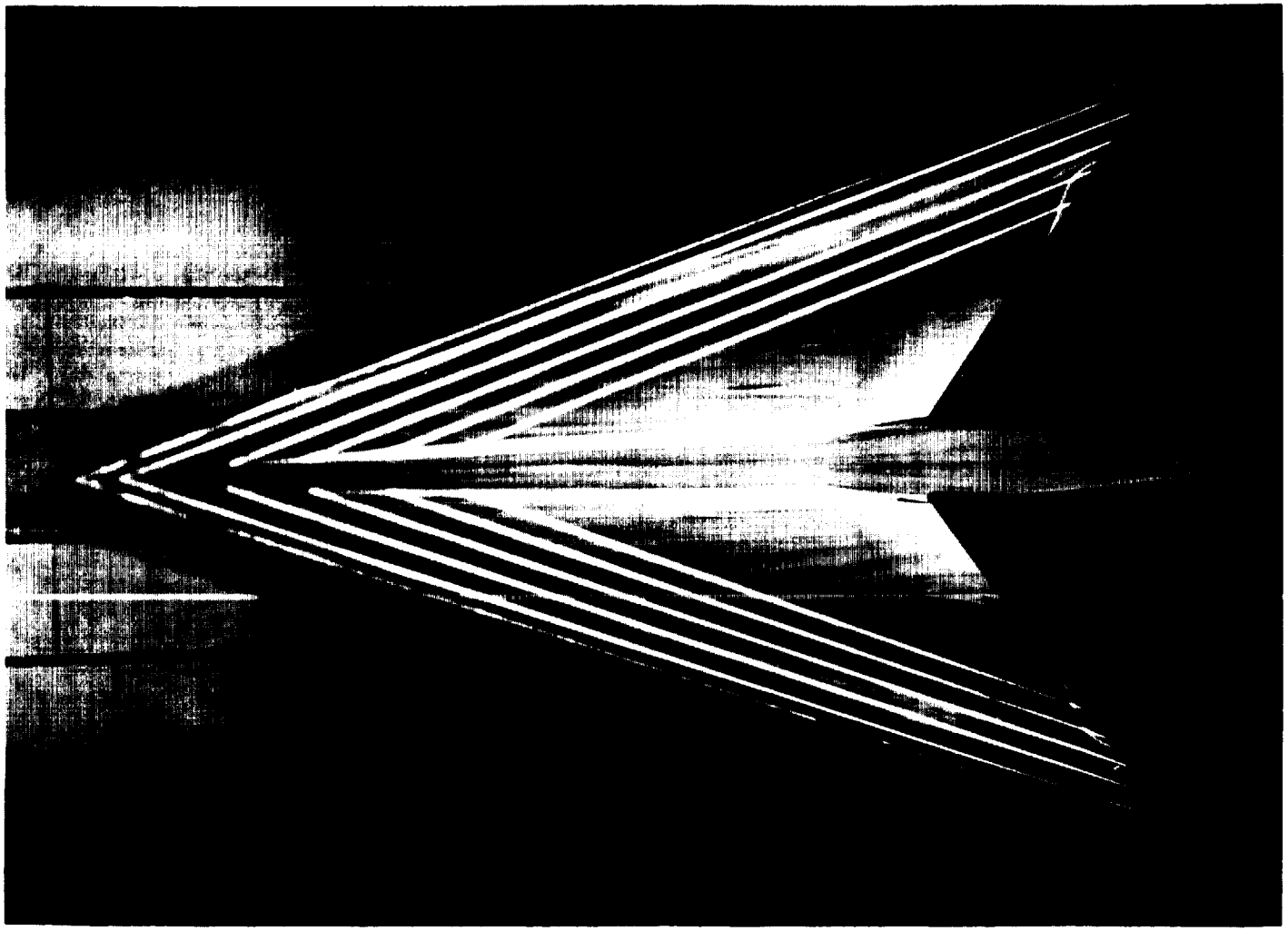

A-26529

Figure 26.- Separated-flow region near the trailing edge of the arrow wing as indicated by a fluorescent-oil film (M = 0.70, $\alpha = 11^{\circ}$).

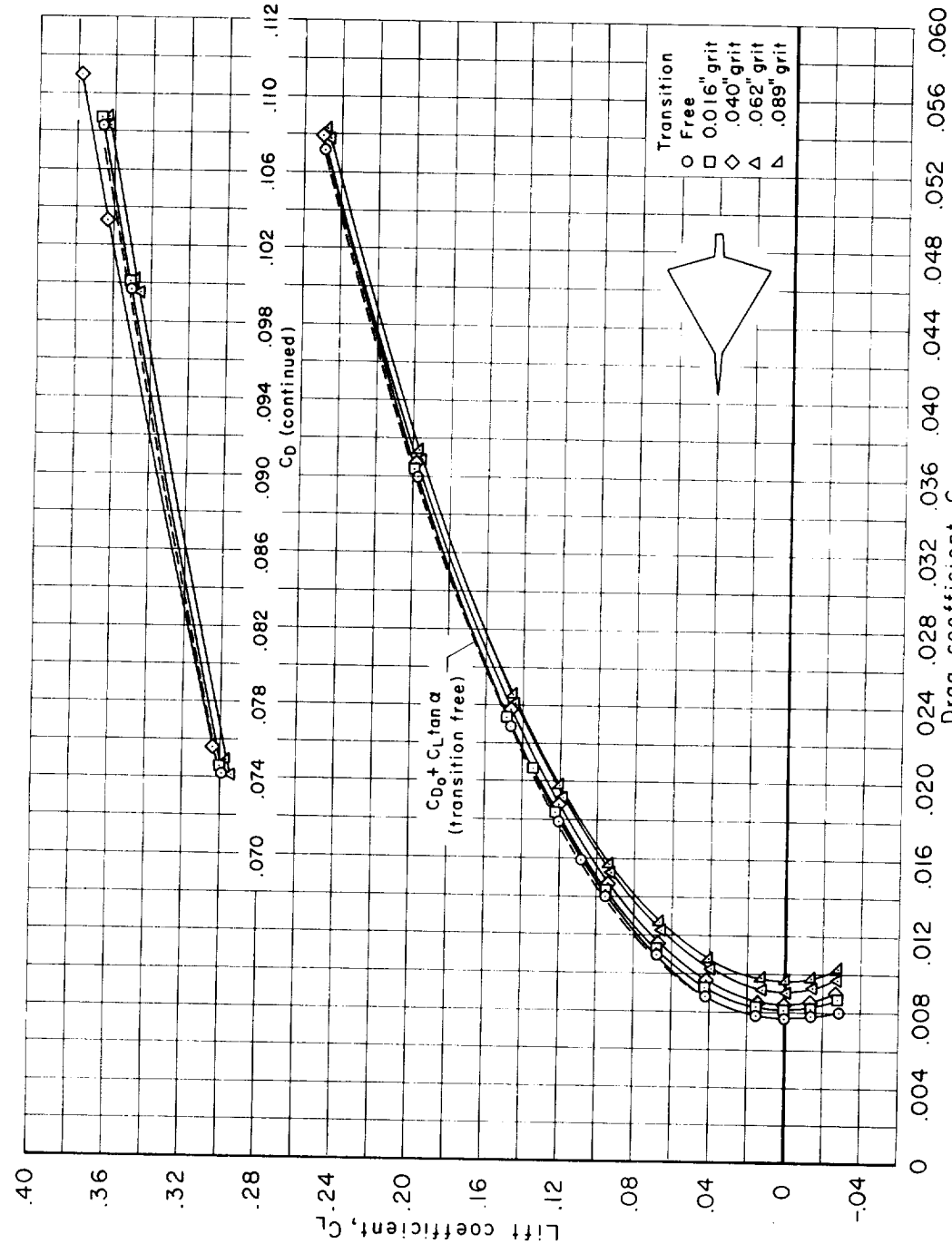

Figure 27.- Lift and drag coefficients for the delta model without bump with transition fixed with four average-sizes of grit and with transition free ($M = 3.00$, R/ft = 2,000,000).

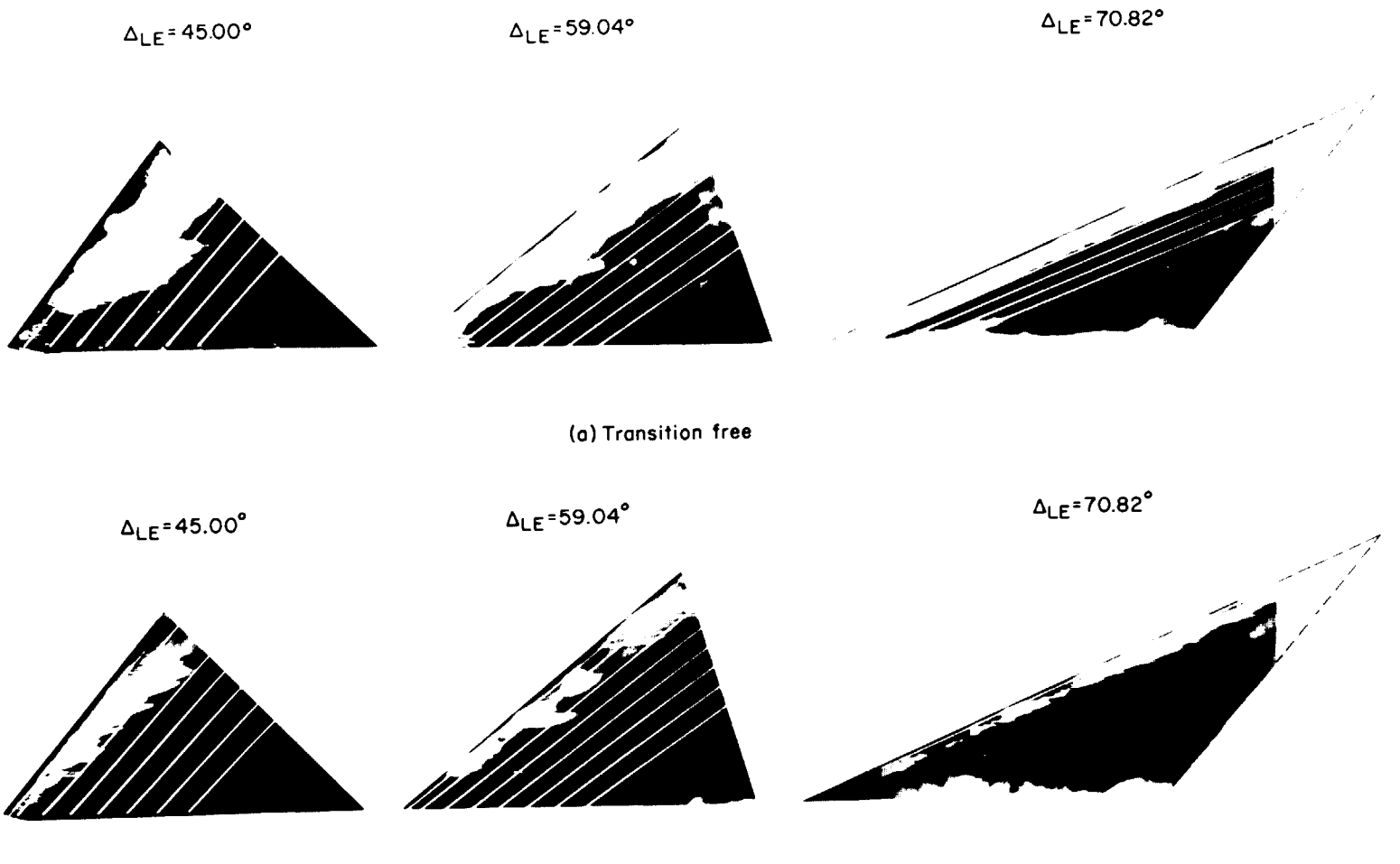

Figure 28.- White regions of laminar boundary layer flow as indicated by fluorene sublimation crystals (M = 3.50, α = 0°, R/ft = 2,000,000).

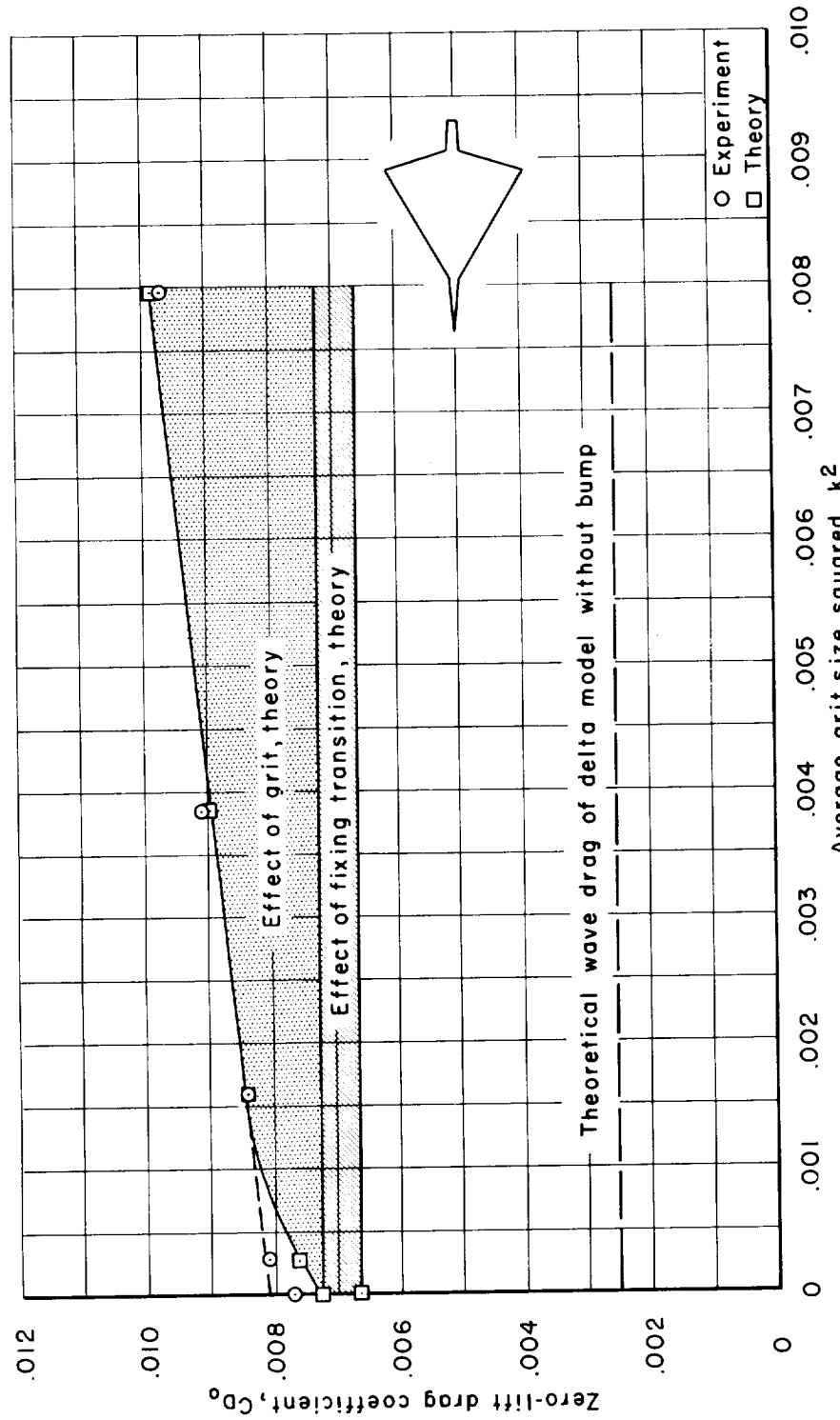

Figure 29.- Effect of average grit size on the zero-lift drag coefficients of the delta model without bump as determined by experiment and theory ($M = 3.00$, R/ft = 2,000,000).

NASA - Langley Field, Va. A-376